Ghent University
Faculty of Sciences
Department of Physics and Astronomy

Constructing Tales of Future Belgian Heatwaves using Ensemble-Mining Strategies

Niels Carlier

GHENT
UNIVERSITY

June 2025

Promotor: Prof. Dr. Ir. Steven Caluwaerts

Copromotor: Kobe Vandelanotte

A dissertation submitted to Ghent University in partial fulfillment of the requirements for the degree of Master of Science in Physics and Astronomy.

Preface

It would have been unwise to attempt writing a thesis without anyone to rely on, so I did not. As such, I have several people to thank sincerely. I would first like to thank professor Steven Caluwaerts for taking me in as a thesis student, for planning out a project with me and for always being so positive and enthusiastic about new results or ideas. I would like to thank my copromotor Kobe Vandelanotte for all the discussions and brainstorm sessions. I am grateful to dr. Bert Van Schaeybroeck, who had to endure an unfathomable amount of data requests, but did not falter in his speedy replies, and to dr. Hans Van De Vyver, for being a valuable source of knowledge and inspiration regarding extreme value statistics and more. I am glad to have shared this year with my fellow thesis students, who have all done amazing work.

It would have been even less wise to attempt studying physics for five years without anyone to rely on, so I did not. I want to thank my parents and my sister for always creating a warm place to come home to. Thank you to my friends for all the support and the great times, to Kurt Vonnegut for writing Slaughterhouse Five, and to my dear roommates for putting up with me. Thank you to Laura, for everything.

Five years came and went. They say it is unwise to look back too often, and yet I did, and yet I will. Vonnegut wrote:

And Lot's wife, of course, was told not to look back where all those people and their homes had been. But she did look back, and I love her for that, because it was so human. So she was turned into a pillar of salt. So it goes.

I am fond of memories, good ones especially. I am fond of the people that I share those memories with. Thank you all. I will forever be a pillar of salt.

Use of Artificial Intelligence

For this thesis, generative AI (`ChatGPT-4o`) was used for debugging the object-oriented framework I wrote for processing long series of daily temperature measurements and automatically identifying heatwaves, as well as for improving the time-shift method to also include leap years. To a lesser extent, AI was also used to interpret certain error messages when attempting to compile Cython code for WBGT calculations using Liljegren's method. No data or results were processed by AI software. No AI tools were used for writing the thesis itself.

Contents

Preface iii

Use of Artificial Intelligence v

1 Introduction 15
- 1.1 The Changing Climate and Extremes . . . 15
- 1.2 Extreme Heat . . . 15
- 1.3 The Storyline Approach . . . 17
  - 1.3.1 Realism, Relevance and Risk-Orientation . . . 18
  - 1.3.2 Constructing Storylines . . . 18
  - 1.3.3 Communicating Storylines . . . 19
  - 1.3.4 Overview of the Adressed Applications . . . 20
- 1.4 Research Objectives . . . 21
- 1.5 Thesis Outline . . . 21

2 Climate Data and Models 23
- 2.1 Observational Data . . . 23
  - 2.1.1 Hourly Local Temperature Series for Brussels . . . 23
  - 2.1.2 Annual Global Temperature Series . . . 23
  - 2.1.3 Zeeschelde Temperature Series . . . 23
  - 2.1.4 E-OBS . . . 24
  - 2.1.5 ERA5 . . . 24
- 2.2 Climate Models and Projections . . . 25
  - 2.2.1 Primitive Equations . . . 25
  - 2.2.2 Climate Modelling and Downscaling . . . 26
  - 2.2.3 EURO-CORDEX . . . 27
  - 2.2.4 Downscaled EURO-CORDEX Projections Over Brussels . . . 28

3 Methods 29
- 3.1 Mining Extremes: Basic Idea . . . 29
- 3.2 Global Warming Scaling . . . 29
  - 3.2.1 Determining GWS Thresholds for Years of Extreme Heat . . . 29
  - 3.2.2 The Local-to-Global Warming Ratio . . . 31
- 3.3 Identifying Extreme Years in Ensembles . . . 32
  - 3.3.1 Two-Sample Kolmogorov-Smirnov Tests . . . 32
  - 3.3.2 Selecting Simulations . . . 33
  - 3.3.3 Shifting Simulations . . . 35
  - 3.3.4 Identifying and Selecting Years of Extreme Heat . . . 35
- 3.4 Impact Analysis . . . 36
  - 3.4.1 Heat Stress . . . 36
  - 3.4.2 Lost Working Hours . . . 37
  - 3.4.3 Zeeschelde Water Temperatures . . . 38
  - 3.4.4 Wildfire Hazard . . . 39

3.4.5 Invasive Insect Species . . . 40
3.4.6 Air Quality . . . 41
3.4.7 Energy Consumption for Heating and Cooling . . . 42
3.5 Evaluating Global Warming Scaling via Extreme Value Theory . . . 42

4 Results **45**
4.1 Global Warming Scaling Results . . . 45
4.1.1 Local-to-Global Warming Ratios . . . 45
4.1.2 Global Warming Scaling Thresholds . . . 46
4.2 Mining Years of Extreme Heat . . . 48
4.2.1 Extreme-Heat Years for EURO-CORDEX Runs . . . 48
4.2.2 Extreme-Heat Years for Statistically-Dynamically Downscaled Runs . . . 50
4.2.3 Summary and Worst-Case Year Selection . . . 51

5 Analysis of the Worst-Case Year **53**
5.1 Heat Warning Systems . . . 54
5.1.1 Federal Heat and Ozone Plan . . . 54
5.1.2 Royal Meteorological Institute Warnings . . . 56
5.2 Heat Stress and Productivity Losses . . . 58
5.3 Zeeschelde Water Temperatures . . . 60
5.4 Wildfire Hazard . . . 61
5.5 Invasive Insect Species . . . 64
5.6 Air Quality . . . 66
5.7 Energy Consumption for Heating and Cooling . . . 66
5.8 Circulation Patterns . . . 67

6 Statistical Evaluation of the Results **69**

7 Discussion **73**
7.1 Performance, Open Challenges and Future Research . . . 73
7.2 Summary . . . 74

A Nederlandstalige Samenvatting **77**

B Extreme Value Theory **79**
B.1 Generalised Extreme Value Distribution . . . 79
B.2 Generalised Pareto Distribution . . . 80

C Liljegren's Method **83**
C.1 Natural Wet Bulb Temperature Model . . . 83
C.2 Globe Temperature Model . . . 84

D The Canadian Fire Weather Index **85**
D.1 Fine Fuel Moisture Code . . . 85
D.2 Duff Moisture Code . . . 86
D.3 Drought Code . . . 87
D.4 Initial Spread Index . . . 87
D.5 Buildup Index . . . 87
D.6 Fire Weather Index . . . 88

Bibliography **89**

List of Tables

3.1 Table of KS statistic thresholds for the parameters HI, TX and TN. 35
3.2 Table of `CLIMEX` growth indices for the three invasive species under study: the brown marmorated stink bug (*Halyomorpha halys*), the Japanese beetle (*Popillia japonica*) and the false codling moth (*Thaumatotibia leucotreta*). 41

4.1 Table of LGWRs for max. temperature T_{max}, min. temperature T_{min} and average temperature T. 46
4.2 Table of GWS Thresholds for HI, T_{max}, Tropical Nights and Heatwave Days. 47
4.3 Kolmogorov-Smirnov test results for EURO-CORDEX runs. D_{HI}, D_{TX}, D_{TN} denote the KS statistic for the parameters HI, TX and TN respectively. Runs that exhibit extreme years, marked by the GWL2.0 GWS tresholds for HI and T_{max}, are highlighted in bold. 48
4.4 Kolmogorov-Smirnov test results for shifted EURO-CORDEX runs. D_{HI}, D_{TX}, D_{TN} denote the KS statistic for the parameters HI, TX and TN respectively. Runs that exhibit extreme years, marked by the GWL2.0 GWS tresholds for HI and T_{max}, are highlighted in bold. 49
4.5 Overview of results for extreme year identification in projections from selected (top part) and shifted (bottom part) EURO-CORDEX runs. N is the total number of identified extreme years. 50
4.6 Kolmogorov-Smirnov test results for downscaled EURO-CORDEX runs over Brussels. D_{HI}, D_{TX}, D_{TN} denote the KS statistic for the parameters HI, TX and TN respectively. Runs that exhibit extreme years, marked by the GWL2.0 GWS tresholds for HI and T_{max}, are highlighted in bold. 51
4.7 Overview of results for extreme year identification in projections from selected downscaled EURO-CORDEX runs. N is the total number of identified extreme years. 51

5.1 Table of key parameter values for the worst-case year and difference with GWS threshold values. 53
5.2 Table of fitted parameter values (left part) and fit quality metrics (right part) for the Zeeschelde T_w model. 61
5.3 Table listing annual heating and cooling loads for the simulated medium-sized, single-story office building in Brussels during the worst-case GWL2.0 year (WCY) and the representative late 20th century year (RPY). 66

List of Figures

1.1 Evolution of the local annual temperature, as measured by the RMI. 16
1.2 Historical overview of heatwave occurrences, as measured by the RMI in Brussels. . 17
1.3 The four fictitious characters presented in the storylines constructed by the Swiss National Centre for Climate Services. Source: Fischer et al. (2022)[1]. 20

2.1 Annual (J-D) surface temperature anomalies for 2024 with respect to the 1951-1980 average. Source: GISTEMP Team (2024)[2]. 24
2.2 A schematic overview of the workflow for downscaling climate models to obtain input data for LIMs in storyline research. The listed LIMs are examples. 25
2.3 A schematic overview of the step-by-step calibration of RCM projections. Source: Duchêne et al. (2020)[3]. 27
2.4 The EURO-CORDEX domain. Source: CORDEX (2024)[4]. 28

3.1 Illustration of the delta-change method to transform the observational temperature time series from Brussels (1878-2023) into a time series at GWL2.0. 30
3.2 Illustration of the KS statistic as the maximal distance between the EDFs of two randomly drawn samples. 33
3.3 Illustrative plot of simulated temperatures compared to observed temperatures for the ten statistically-dynamically downscaled RCP8.5 runs over Brussels, averaged over ten years. 34
3.4 Illustrative plot of the procedure for shifting simulated series along the time axis. . 36
3.5 Map indicating the location of the Lillo measuring post in the vicinity of the energy plants in Doel. 38
3.6 Schematic overview of the different components that make up the FWI. Source: Lehtonen et al. (2014)[5]. 39
3.7 Illustrative photographs of the three invasive species under study: the brown marmorated stink bug (*Halyomorpha halys*) (a), the Japanese beetle (*Popillia japonica*) (b), and the false codling moth (*Thaumatotibia leucotreta*) (c). Source: USDA (2018)[6]. 40
3.8 Geometry of the simulated medium-sized, single-story office building. 42

4.1 Plot of the local (Brussels) anomalies for T_{max} and T_{min} relative to the conventional 1951-1980 average, along with the global anomaly from GISTEMP v4, all represented as a centered 10-year moving average. 45
4.2 Results of the GWS delta-change transformation for HI, T_{max}, Tropical Nights and Heatwave Days. 46
4.3 Comparison of annual average temperatures between observational series and surviving EURO-CORDEX runs, over the KS testing range. 48
4.4 Comparison of annual average temperatures between observational series and surviving statistically-dynamically downscaled EURO-CORDEX runs, over the KS testing range. 50
4.5 Overview of all the obtained years of extreme heat, marked by exceedance of GWL2.0 GWS thresholds for HI and T_{max}. 51

5.1 Plot of the local (Uccle) daily temperatures for the worst-case year 2059. The shaded yellow areas correspond to heatwaves according to the RMI definition. 53
5.2 Map of TX values for every grid point covering Belgium on the hottest days of both heatwave periods. 54
5.3 Overview of federal heat warning plan phases as they would be declared for the historically extreme years 1976 (a) and 2018 (b), and for the selected worst-case GWL2.0 year 2059 (c). 55
5.4 Overview of RMI heat warning phases as they would be declared for the historically extreme years 1976 (a) and 2018 (b), and for the selected worst-case GWL2.0 year 2059 (c). 57
5.5 Plot of daily max. WBGT values for the worst-case year 2059 and the historically extreme year 1976. Background colors indicate recommended maximal exposure levels for different metabolic rates M, according to ISO 7243. 58
5.6 Map of Max. WBGT values for every grid point covering Belgium on the hottest days of both heatwave periods. 58
5.7 Map of lost working days across the entire worst-case year for every grid point. . . 59
5.8 Plot of LWH_d in Uccle for the worst-case year 2059 and for 1976. No nonzero values occur outside of the displayed range of dates. 59
5.9 Plot of modelled and measured water temperatures for the Zeeschelde at the Lillo measuring post, along with measured local air temperatures for reference. 60
5.10 Plot of modelled water temperatures for the Zeeschelde at the Lillo measuring post during the worst-case year 2059 and comparison with historically extreme years 1976 and 2018. 61
5.11 Plot of daily precipitation values at Uccle for the worst-case year 2059. 62
5.12 Plot of daily FWI values for Kalmthoutse Heide during fire hazard monitoring for the worst-case year 2059 and the historically extreme year 1976. Background colours indicate FWI danger classes. 63
5.13 Map of wildfire danger in Belgium on the most hazardous day of the worst-case year 2059. 63
5.14 Comparative overview of the calculated voltinism of the brown marmorated stink bug (*Halyomorpha halys*), the Japanese beetle (*Popillia japonica*) and the false codling moth (*Thaumatotibia leucotreta*), evaluated at the Sint-Truiden Fruit Valley. 64
5.15 Comparative maps showing the calculated voltinism for 1976 (left) and the worst-case year 2059 (right) of three invasive species under study: the brown marmorated stink bug (*Halyomorpha halys*) (a), the Japanese beetle (*Popillia japonica*) (b) and the false codling moth (*Thaumatotibia leucotreta*) (c). 65
5.16 Plot displaying daily average temperatures T as well as stagnation conditions for the worst-case year 2059, evaluated for Uccle. The shaded yellow areas correspond to heatwaves according to the RMI definition. Shaded blue areas correspond to H-ASI stagnant days that do not coincide with heatwave days, while shaded green areas mark days that are simultaneously a heatwave day and an H-ASI stagnant day. 66
5.17 Plot of the monthly heating and cooling loads for the simulated medium-sized, single-story office building in Brussels during the worst-case GWL2.0 year (left) and the representative late 20th century year (right). 67
5.18 Map of SLP (white contours) and T_{850} (shaded contours) for the hottest day of the worst-case year 2059. 67

6.1 Mean residual life plot showing mean excesses as a function of POT threshold choice for the pooled, bias-corrected GWL2.0 EURO-CORDEX runs. The shaded green area corresponds to the identified threshold range for linear behaviour. 69

6.2 Parameter stability plots displaying how the shape parameter ξ (left) and the redefined scale parameter σ^* (right) scale with changing threshold definitions for the GPD model. 70
6.3 Diagnostic plots showing the quality of the GPD fit to the GWL2.0 HI exceedances: a quantile plot (left) and a probability plot (right). 70
6.4 Plot of return values and return periods for HI as determined from the pooled, bias-corrected GWL2.0 EURO-CORDEX runs. The value associated with the worst-case year 2059 (610.85 CDD) is marked by a dashed red line. 71

1 Introduction

1.1 The Changing Climate and Extremes

In recent years, the study of climate change and its consequences has become an important field of interdisciplinary research. The impact of climate change manifests on an ecological and environmental level, while also affecting different societal and economical sectors in many ways[7]. In a context of policy-making for adaptation and mitigation, it is therefore important to investigate what the impact of the ongoing change in our climate will be, and to evaluate methods for making such plausible and reliable assessments.

A particular example of such reverberations is that of extreme weather and climate events, of which the intensity and/or frequency have, to some extent, increased as a consequence of human-induced greenhouse gas emissions and changes in land-use[8]. In their 2023 report, the Intergovernmental Panel on Climate Change (IPCC) defines two types of extreme events:

1. An extreme weather event is an event that is rare at a particular place and time of year.
2. An extreme climate event is a pattern of extreme weather that persists for some time, such as a season.

A well-known example of an extreme weather event is the Vesdre flood event of July 2021[9], while the exceptionally dry Western-European spring of 2025 can be regarded as an extreme climate event[10]. The rarity of an event is to be interpreted within the context of the application at hand. In the aftermath of such events, questions arise on how the event came to be, whether it might occur again, and in what severity. *Observed event-based science* aims to answer these questions, and as such connects climate projections to the human experience[11].

Detecting trends in extremes is inherently challenging due to their rarity. Observational time series are often limited in duration, complicating robust statistical analysis of trends in extremes. Efforts to create long, consistent historical time series have gained attention but remain difficult due to issues such as homogenisation. Caution is warranted, on the other hand, when using climate-model projections to investigate extremes. Certain extreme events (e.g. short-duration extreme precipitation) are not well resolved at the resolutions of current climate models. Recent studies have also highlighted model difficulties in reproducing observed trends in heatwaves in Western-Europe[12], potentially due to inadequate representation of changes in circulation patterns[13] or the non-linear feedback between land and atmosphere in models[14]. In summary, despite the critical societal relevance of understanding trends in extremes, distilling this information from the vast amounts of climate projection data presents significant challenges and limitations.

1.2 Extreme Heat

A key indicator of climate change is the global mean surface temperature (GMST), which has risen significantly since the end of the pre-industrial period. It has been reported that the GMST in

2011-2020 was around 1.1 °C higher than the value for 1850-1900[15]. This global temperature increase with respect to the pre-industrial world is referred to as the *Global Warming Level* (GWL). A temperature rise of 1.1 °C is denoted as GWL1.1.

With temperatures on the rise, heatwaves and heat extremes are expected to become more common and more intense in all their properties[16]. The focus of this thesis is on such future heat extremes. Applying an observed event-based approach, we study plausible heat scenarios and characterise projected extremes.

The local climate in Belgium is no exception to the global trend of rising temperatures. Figure 1.1 shows the evolution of yearly temperatures, as measured by the RMI in Brussels[1]. Note that the temperature has risen at a noticeably higher rate at this local scale than it has globally; there is a significant difference between local and global warming rates. This is a generally valid statement[17, 18].

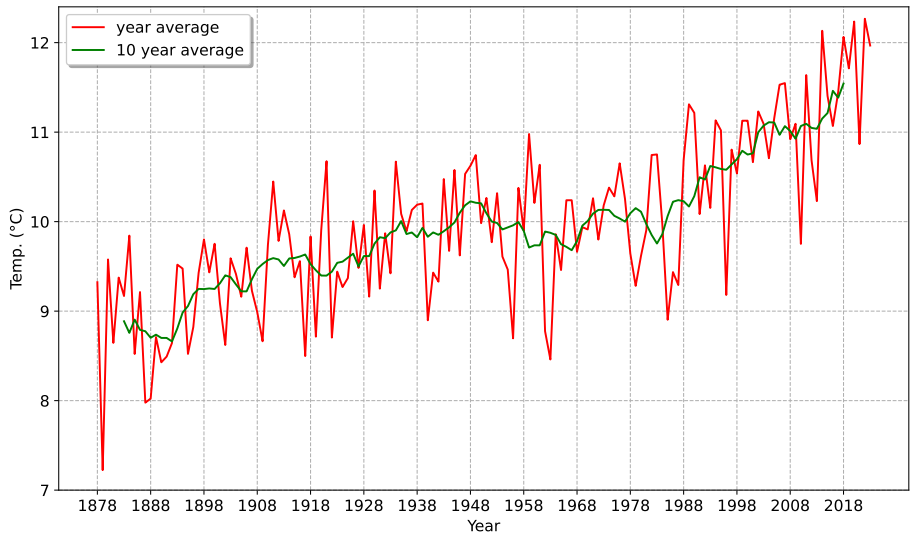

Figure 1.1: Evolution of the local annual temperature, as measured by the RMI.

The rising temperatures should be accompanied by an increase in the frequency and intensity of heatwaves, as previously stated. In Belgium, a heatwave is defined as a period of at least five consecutive days for which the two following criteria are simultaneously met[19]:

1. The maximal temperature reaches or exceeds 25 °C on every day.

2. The maximal temperature reaches or exceeds 30 °C on at least three days across the considered period.

The effect of the rising local temperatures is clearly visible in figure 1.2, which shows the historical occurrence of heatwaves as recorded by the RMI. Notably extreme years are, for example, 1947, 1976 and 2018. Such years provide good starting points for our study.

[1]Note that while we refer to Brussels, the RMI has been performing measurements in Uccle since the early 20th century.

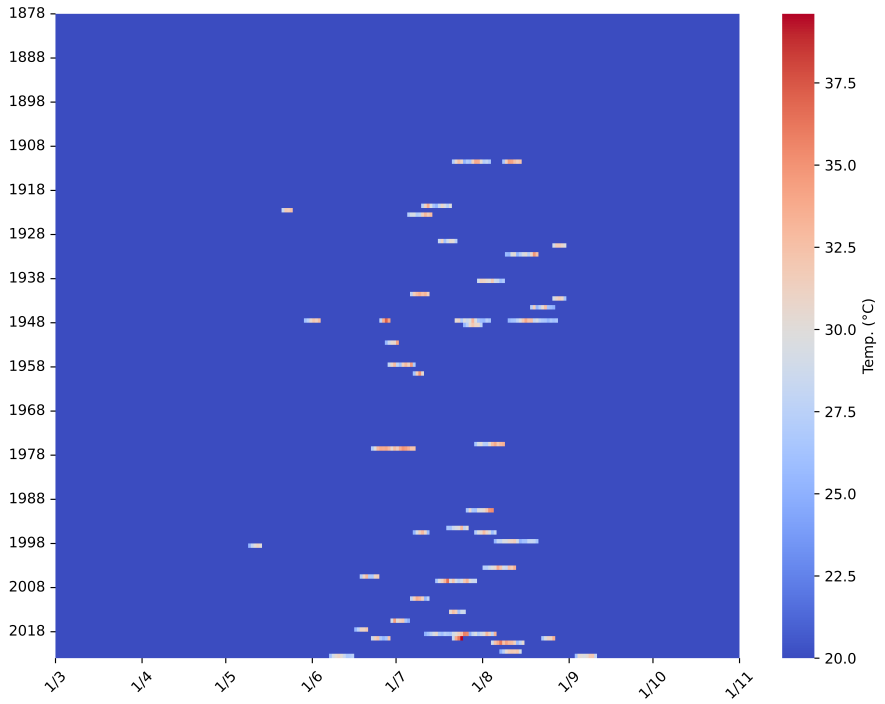

Figure 1.2: Historical overview of heatwave occurrences, as measured by the RMI in Brussels.

1.3 The Storyline Approach

It is hardly a straightforward task to probe projected extreme heat events in a way that is useful and informative for stakeholders and policy-makers. Most commonly, climate scientists present findings in a probabilistic sense. Predictions are derived from large ensembles of future climate simulations involving many models, and quantitative trends and probabilities for meteorological fields are obtained. In Hazeleger et al. (2015), this has been referred to as the *Model-Correct-Downscale-Translate* (MoCoDoT) approach[20].

However, such a probabilistic framework often has to contend with various problems, such as a lack of long-term observations, which results in a high degree of uncertainty, subjectivity in the definition of extreme events (e.g. choice of spatial or temporal scale, domain size), possible limitations of statistical models for extreme values, systematic errors in climate models, etc. MoCoDoT, by nature, tends to neglect low-likelihood but potentially high-impact events. However, these low-likelihood, uncertain events might pose the greatest threats to society. Event-based *storylines* or *tales of future weather* are an alternative to this norm, and allow us to investigate such high-impact extremes, pivoting to plausibility instead of probability as the key notion[21]. According to Shepherd (2016) and Shepherd et al. (2018), we may define a storyline as *a physically self-consistent unfolding of past events, or of plausible future events or pathways*[22, 23]. At the center of these event-specific scientific *narratives* are the driving factors and underlying processes of the events and their consequences, rather than probabilistic outcomes. Unlike MoCoDoT, the goal of the storyline approach is not to predict states of the climate system or assign probabilities to such states, but rather to gauge the effects of bringing the system under severe stress[24]. This is done by describing individual events on a localised scale.

We may identify four major strengths of the (event-based) storyline[23]:

1. The storyline triggers *episodic memory*[11], improving risk awareness by framing said risk in a way that corresponds directly to how it is perceived by individuals.

2. The storyline exposes vulnerabilities or breaking points in policies or decision-making processes related to extreme events. In this sense, storylines have clear potential to strenghten decision-making.

3. The storyline provides a physical basis for partitioning uncertainties relative to thermodynamic and dynamic aspects of studied events[25]. In MoCoDoT, on the other hand, these uncertainties are mixed.

4. By construction, the storyline explores the boundaries of plausibility, eliminating concerns of false precision and surprise.

Storylines might be perceived as anecdotal and therefore unscientific. For this reason, it is important to keep the above scientific strengths in mind when constructing such tales of future weather, and to outline criteria for assessing the scientific quality of such studies.

1.3.1 Realism, Relevance and Risk-Orientation

The event-based storylines are researched with the aim of providing stakeholders with plausible *benchmarking* projections and data. From this point-of-view, the quality of storylines can be evaluated based on three criteria: realism, relevance and risk-orientation[26].

The need for realistic storylines encourages the use of historical event chains. Observed time series may be transformed to a future climate, and the properties and impact of these *futurised* extreme events may be studied[16].

The relevance of the storyline relates to application of the approach to subjects and phenomena that are important to stakeholders and decision-making individuals. An illustrative example of this is the need for city planners to take into account future heat extremes when designing urban infrastructure, especially since cities experience more severe heat stress during such extreme events; a phenomenon known as the *Urban Heat Island* (UHI)[3].

Storylines are by nature highly risk-informative, and act as an effective *stress-test* for infrastructure, management and policy. Once we have constructed a scientifically sound, event-based storyline, in line with the aforementioned criteria, we may apply our findings on different scales and across different sectors, to describe in detail the impact of heat extremes within a selection of applications, based on stakeholder's needs and priorities.

1.3.2 Constructing Storylines

A challenging aspect of the storyline approach is obtaining the necessary data for constructing storylines that satisfy the three criteria listed in section 1.3.1. Many frameworks have been proposed. In this section, we give a brief overview of the methodologies that are most prominent in the literature.

Tales of future weather may shine light on how severe an observed extreme (e.g. a heatwave) could have plausibly been. Ciullo et al. (2021) argue that storyline research benefits from such *counterfactual thinking*, and a framework is presented for constructing storylines as so-called *downward*

counterfactuals, which describe critical events that could have occurred but did not[24]. The framework exploits ensembles of past numerical weather prediction (NWP) data to identify such counterfactuals, because these forecasts take into account the physical drivers. A similar method is that of *ensemble boosting*, as presented by Fischer et al. (2023)[27]. Starting from an ensemble of past forecasts or climate simulations, ensemble boosting generates plausible physical event trajectories by repeatedly re-initialising the NWP model using small random perturbations to the atmospheric conditions. The procedure is repeated for perturbed ensemble members that result in the most extreme circumstances, while the remaining members are discarded. This way, the most extreme yet plausible event trajectories are obtained. The application of ensemble boosting is not restricted to downward counterfactuals, but can be applied to future climate model projections as well to obtain extremes in a given future climate.

Another popular strategy is to generate synthetic time series using *Stochastic Weather Generators* (SWGs). SWGs are data-driven statistical tools to model long synthetic time series of weather variables, such as temperature, precipitation or wind with the same spatio-temporal statistical characteristics as the original observational product[28]. Yiou (2014) developed an SWG based on analogues of atmospheric circulation[29]. In Yiou and Jézéquel (2020), this SWG is complemented with an importance sampling algorithm to generate extreme temperature series[30]. This importance sampling SWG is also implemented in Pfleiderer et al. (2021) to study compound extremes affecting crop yields[31]. Brunner et al. (2021) assess compound hot-dry events using a wavelet-based SWG through the concept of phase randomisation[32, 33]. As input for any SWG we can use observational time series or reanalysis data to generate downward counterfactuals, or model projections to generate long series in a counterfactual climate.

We also address the *Pseudo-Global Warming* technique for regional modelling in a counterfactual climate - like GWL2.0 or pre-industrial - which was first described in Schär et al. (1996)[34]. PGW involves directly imposing large-scale climate system changes onto a baseline regional climate simulation of an extreme weather event by altering the initial and boundary conditions while preserving key atmospheric balances. Climate change signals are drawn from transient climate simulations and with respect to a control simulation period. Brogli et al. (2023) developed the `PGW4ERA5` software to impose PGW modifications onto ERA5 reanalysis data at the boundaries of a regional model. PGW was applied by de Vries et al. (2024) to obtain storylines for the 2019 European heatwave in a warmer climate[16].

The relatively high computational cost of the methods discussed so far renders them somewhat less attractive in an operational context. Alternatively, we may exploit climate simulation ensembles and construct tales of future weather by identifying relevant extremes in the projections. Van der Wiel et al. (2021) construct drought storylines for a future European climate by selecting analogues of observed events in unconstrained simulation runs[11]. In Yiou (2024), an ensemble-based strategy is employed to describe isolated temperature spikes in the city of Paris marked by the exceedance of a 50 °C threshold[35]. This thesis presents a new, threshold-based ensemble-mining framework called *Global Warming Scaling* to construct tales of future Belgian heatwaves in a warmer climate.

1.3.3 Communicating Storylines

Once storylines have been constructed in a scientific sense, they have to be communicated to stakeholders and the public in an adequate way. The literature contains several examples of such innovative communication strategies.

The Swiss National Centre for Climate Services introduced a concrete narrative approach with four fictitious persons to communicate key results of national storyline research[1]. The narratives describe how each of the characters are affected by adverse consequences of climate change in 2060, and are complemented with the most relevant numbers concerning mean climate change. The four characters represent several generations and different parts of Switzerland. Artistic renderings of these characters are shown in figure 1.3.

Figure 1.3: The four fictitious characters presented in the storylines constructed by the Swiss National Centre for Climate Services. Source: Fischer et al. (2022)[1].

Shepherd et al. (2018) discuss stakeholder meetings, where attendants are presented with brief textual descriptions of storyline events, and then discuss with each other the potential impact of said event on their respective sectors or groups[23]. In a 2023 report, the Royal Netherlands Meteorological Institute reports on the previously mentioned study of the 2019 heatwave in a warmer climate by giving a textual desciption of the event, detailing which phase of the Dutch national heat plan would be adopted[36]. In a June 2019 newsletter, the Belgian Royal Meteorological Institute presented storyline results in the form of fictional weather forecasts[37].

1.3.4 Overview of the Adressed Applications

Concrete narratives are constructed with the aid of local impact models. We assess the impact of prolonged extreme heat within a number of concrete applications:

- We will model productivity losses for heavy outdoor workforces due to excessive heat stress exposure.
- We will model the water temperature of the Zeeschelde near energy plants, which may influence the efficiency of energy production.
- We will assess wildfire hazard using the Canadian Fire Weather Index.
- We will model population growth of invasive insect species that pose a potential agricultural threat.
- We will assess air quality by identifying days of atmospheric stagnation.
- We will investigate how energy consumption for air conditioning changes in a warming Belgian climate.

These applications are further elaborated on in later sections.

1.4 Research Objectives

The goal of this thesis is to study the impact of future heat extremes in Belgium. This is done using an event-based storyline approach, as described in section 1.3. We take reliable data from past heatwaves and heat extremes as input for our analysis, and search for plausible high-impact heat events in a GWL2.0 climate. Once event metrics are obtained, storylines can be constructed and elaborated on in detail in the context of the applications listed in section 1.3.4.

1.5 Thesis Outline

Chapter 2 is dedicated to a description of the observational and modeled data used in this work. An overview of the methodologies is given in chapter 3, where ensemble-based strategies for characterising and identifying years of extreme heat are explained in sections 3.2 and 3.3, while some impact models and corresponding calculations are summarised in section 3.4. General results of the thesis project are reported on in chapter 4. As a proof of concept, we select a worst-case scenario year of extreme heat, and analyse said year in terms of the aforementioned applications. This discussion can be found in chapter 5. We perform a detailed statistical analysis of said year in a GWL2.0 climate; this is written out in chapter 6, with accompanying details regarding Extreme Value Theory included in appendix B. In section 7.1, we draw conclusions relating to the presented framework and formulate some remaining methodological challenges and open research questions. Conclusions of the thesis project are summarised in section 7.2.

2 Climate Data and Models

2.1 Observational Data

2.1.1 Hourly Local Temperature Series for Brussels

This thesis is a study of extreme events in Belgium and their evolution under future climate change. As such, long series of climate observations are an essential starting point of this investigation. Moreover, as stated in section 1.3.1, historical observations are evidently useful in constructing realistic storyline scenarios. We will therefore make use of observational temperature series.

Interpreting raw instrumental data in the context of climate change research is difficult. Observational time series may contain erroneous values, and changes in measurement techniques or conditions are known to cause artifacts or breaks in the data that are unrelated to real variations in the climate change signal[38]. Efforts to remove such non-climatic artifacts are collectively referred to as *homogenisation*[39]. Homogenised Belgian temperature series exist for several time scales[40, 41].

We will employ a homogenised time series of hourly temperature measurements in Brussels between 1878 and 2023, provided by the RMI.

2.1.2 Annual Global Temperature Series

Climate change is often expressed in terms of GMST anomalies. In order to study extreme heat in future climates, we therefore require global warming data over the historical range. This study makes use of GMST anomaly data made publicly available by NASA under the *Goddard Institute for Space Studies* (GISS) *Surface Temperature* (GISTEMP) product[42, 43], which combines measurements of sea surface temperature and land surface air temperature to estimate how temperature has changed on Earth since 1880. Specifically, we exploit the GISTEMP v4 dataset with annual anomaly data from 1880 to 2023. Recent results for gridded annual surface temperature anomalies for 2024 are shown in figure 2.1. We notice strong variations in regional anomalies, which will prove important in the remainder of this thesis. In this investigation, we only work with global anomalies averaged annually across the Earth's surface.

2.1.3 Zeeschelde Temperature Series

We will implement a model to estimate the temperature of the Zeeschelde near the power plants in Doel, Antwerp. This model is fitted using water temperature measurements from the Lillo measuring post, the data from which is made publicly available by the Flemish authorities through the *Waterinfo* project[44]. The dataset contains water temperatures recorded at the measuring post between 1st October 2015 and 18th September 2022[45].

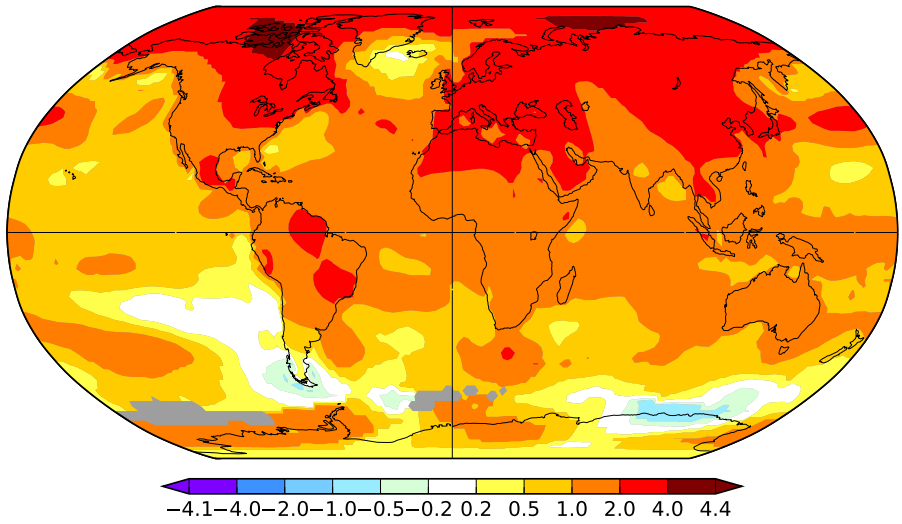

Figure 2.1: Annual (J-D) surface temperature anomalies for 2024 with respect to the 1951-1980 average. Source: GISTEMP Team (2024)[2].

2.1.4 E-OBS

The water temperature model mentioned in section 2.1.3 is calibrated using air temperature and radiation data from E-OBS for the grid point nearest the Lillo measuring post. E-OBS is a daily gridded observational dataset covering land areas across Europe[46, 47]. It is based on blended time series from the station network of the European Climate Assessment & Dataset project[48]. E-OBS meteorological datasets are available on a 0.1 and 0.25 degree regular grid and provide coverage between 1950 and 2024. All data come directly from European National Meteorological and Hydrological Services or other institutions.

2.1.5 ERA5

Some calculation results for simulated future events will be compared to past events. The meteorological data required for such calculations involving past events is provided by the *European Centre for Medium-Range Weather Forecasts* (ECMWF) *Reanalysis v5* (ERA5). ERA5 is a state-of-the-art global reanalysis dataset. It provides hourly estimates of a wide range of atmospheric, land, and oceanic climate variables from January 1940 onwards at a horizontal resolution of 31 km, and at 137 atmospheric height levels[49].

This study will use the ERA5-Land Reanalysis, which is an enhanced version of ERA5 which is produced by replaying the land component of the climate reanalysis, thereby increasing the spatial resolution to 9 km[50]. We note that only relative humidity (RH) is not a readily available field in ERA5-Land, and we compute it from air temperature T_a and dewpoint temperature T_d (in °C) using the Magnus-Tetens formula for saturation vapour pressure[51]:

$$e_{sat}(T) = 6.1078 \exp\left(\frac{17.1T}{235+T}\right) \tag{2.1}$$

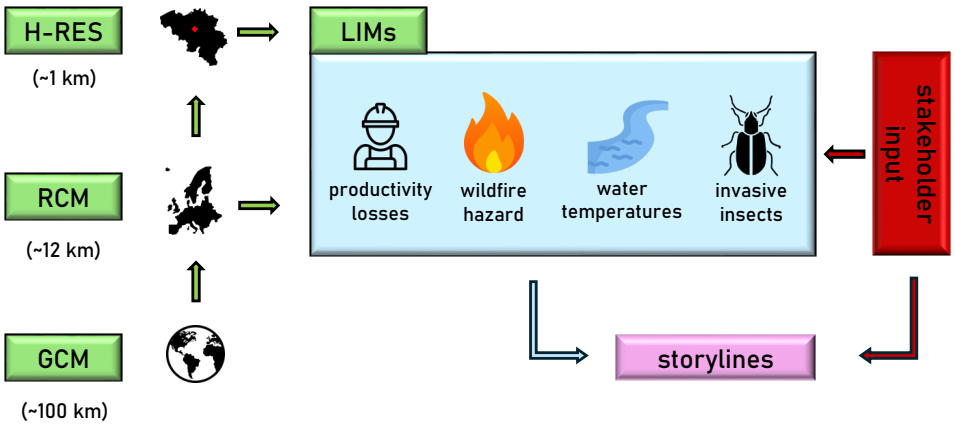

Figure 2.2: A schematic overview of the workflow for downscaling climate models to obtain input data for LIMs in storyline research. The listed LIMs are examples.

which gives the result in hPa. The above formula is based on the integrated Clausius-Clapeyron equation. Given dewpoint T_d, we can use it to calculate vapour pressure $e \equiv e_{sat}(T_d)$. The saturation vapour pressure at the given air temperature T_a is $e_s \equiv e_{sat}(T_a)$. Relative humidity can then simply be obtained as $\text{RH} = 100 \times e/e_s$.

2.2 Climate Models and Projections

This section contains a review of climate modelling and downscaling, as well as an overview of the models used in this thesis. Data from these models is used as input for *Local Impact Models* (LIMs) which are crucial to storyline research. Such models are optimally selected based on stakeholder needs. An overview of the general workflow is shown in figure 2.2.

2.2.1 Primitive Equations

The evolution of atmospheres is studied using climate (or weather) models. The system under investigation is governed by sets of mathematical equations - referred to as *primitive equations* - which are founded in physical principles applied to a so-called *air parcel*[52]:

$$\frac{D\mathbf{U}}{Dt} = -2\boldsymbol{\Omega} \times \mathbf{U} - \frac{\nabla p}{\rho} + \mathbf{g} + \mathbf{F_r} \qquad \text{(momentum equation)} \qquad (2.2)$$

$$\frac{DT}{Dt} = \frac{RT}{c_p}\frac{D\ln p}{Dt} + \frac{J}{c_p} \qquad \text{(thermodynamic energy equation)} \qquad (2.3)$$

$$\frac{D\rho}{Dt} = -\rho\nabla \cdot \mathbf{U} \qquad \text{(continuity equation)} \qquad (2.4)$$

$$p = \rho RT \qquad \text{(ideal gas law)} \qquad (2.5)$$

Equations 2.2, 2.3 and 2.4 are examples of *prognostic equations*, because they describe the time evolution of *prognostic variables* such as the wind velocity vector $\mathbf{U}$, temperature T and density ρ. Equation 2.5 features no time derivative, and is therefore a *diagnostic equation*. $\boldsymbol{\Omega}$ denotes the

Earth's angular velocity, $\mathbf{g}$ the gravity[1] and $\mathbf{F_r}$ is the frictional force exerted on the parcel. R is the ideal gas constant, c_p is the specific heat capacity of air at constant pressure and J is the rate of heat transfer. The total time derivative in the prognostic equations is the sum of the Eulerian derivative and an advective term:

$$\frac{D}{Dt} = \frac{\partial}{\partial t} + \mathbf{U} \cdot \nabla \tag{2.6}$$

In general, it is not possible to derive closed-form solutions to these dynamical equations, so that one must resort to numerical models to obtain approximate solutions.

2.2.2 Climate Modelling and Downscaling

The IPCC employs projections from a sophisticated type of climate model called a Global Circulation Model (GCM)[53]. GCMs are powerful tools to represent the climate system in three dimensions according to the governing equations and conservation laws such as the continuity equation and the ideal gas law[54]. A GCM is constructed by first defining a discrete mesh that surrounds the Earth at several vertical levels to represent the atmosphere. The evolution of the atmosphere is then computed by solving the equations for each time step in each grid point. For each of the cells of the partitioned atmosphere, the GCM computes a wide array of physical processes that affect the time evolution of the system, including radiative transfer in the atmosphere, but also large-scale heat transport, consequences of aerosols, changes in snow cover and sea ice, and surface fluxes of heat and moisture. Given the high computational cost of solving a GCM, these simulations remain rather coarse, with a typical horizontal resolution of 100-400 km. This means that many components of the climate system, such as urban surfaces or convective clouds, are not well represented. This makes it difficult to use these global models to assess the societal impact of climate change, which is felt mainly through extreme events depending on small-scale processes[55]. Stakeholders typically require information on a very local scale that is relevant to their sectors or policies. We thus need a method to derive smaller-scale information from the GCM, which is referred to as *downscaling*.

A Regional Climate Model (RCM) is a limited-area, high-resolution model that simulates the regional climate in the context of the changing global climate, given atmospheric conditions at the boundaries. The boundary conditions are provided by the low-resolution GCM in which the RCM is nested. This downscaling technique is called *dynamical downscaling*. RCMs are commonly applied at a grid resolution of a few tens of kilometers[56, 57].

RCMs are, however, still not sufficiently sophisticated for the study of urban effects and impacts, due to the still relatively coarse spatial resolution and the fact that they lack a scheme for incorporating urban effects. In principle, one could perform a further dynamical downscaling up to kilometric resolution[55], but this is computationally expensive, especially when the goal is to downscale a full ensemble. A more manageable approach that can be applied to downscale an ensemble of RCMs to the urban level, aiming specifically to resolve the UHI effect, is that of *statistical-dynamical downscaling*[3]. The method consists of calibrating RCM projections before downscaling to the city level, by incorporating the signature of urban-atmosphere interactions. This signature is obtained as the difference in all relevant meteorological variables between two high-resolution (below 10 km) climate simulations of a limited number of past years: one where surface exchanges between the urban canopy and the atmosphere are explicitly parametrised (H-RES UP), and one where they are not (H-RES NO-UP). The RCM can be converted to the signature resolution using a simple interpolation scheme. For each day of the RCM time series, the most analogous day in the H-RES NO-UP dataset is found using a least square scheme, and the associated urban signatures are added

[1] Note that the gravity $\mathbf{g}$ is defined to represent the combined effects of gravitational and centrifugal forces.

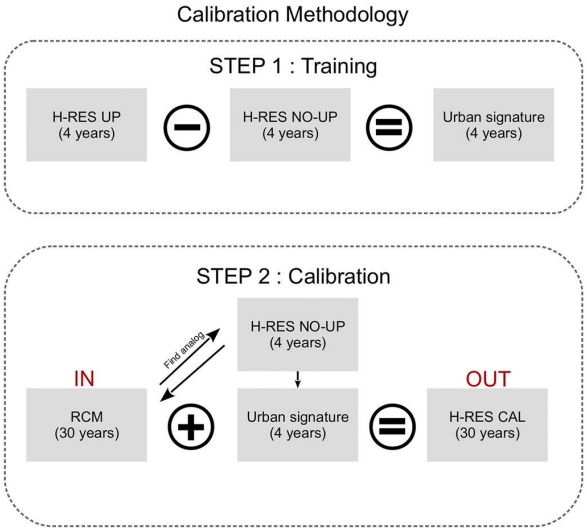

Figure 2.3: A schematic overview of the step-by-step calibration of RCM projections. Source: Duchêne et al. (2020)[3].

to the RCM results to obtain the calibrated RCM at signature resolution. This calibrated RCM can be used as input for downscaling to the city level. The statistical-dynamical downscaling approximates the full dynamical downscaling, but at a reduced computational cost on account of the calibration. A schematic of the workflow is shown in figure 2.3.

2.2.3 EURO-CORDEX

The *Coordinated Regional Climate Downscaling Experiment* (CORDEX) is an international initiative by the *World Climate Research Programme* (WCRP) aimed at producing high-resolution regional climate projections by downscaling GCM simulations[4]. EURO-CORDEX, in turn, is the European branch of the initiative, producing regional climate simulation ensembles that cover all of Europe. The domain of each of the EURO-CORDEX simulations is shown in figure 2.4. The GCMs used for the downscaling are sourced from the *Coupled Model Intercomparison Project Phase 5* (CMIP5)[58]. The resulting EURO-CORDEX ensemble is the one used in this thesis. It is worth mentioning that in the near future, the full EURO-CORDEX ensemble of experiments driven by CMIP6 GCM runs will become publicly available on Earth System Grid Federation nodes[59].

EURO-CORDEX ensembles focus on two spatial resolutions: the standard CORDEX resolution of about 50 km (0.44 °), and a finer resolution of about 12.5 km (0.11 °)[60]. The simulations incorporate different scenarios for the evolution of greenhouse gas emissions. Each of these scenarios corresponds to a different *Representative Concentration Pathway* (RCP). RCPs are labeled using the value of the radiative forcing in the year 2100 within the corresponding emission scenario[61]. In this thesis, we use projected hourly data for Belgium from RCP8.5 EURO-CORDEX runs sourced from CMIP5. The EURO-CORDEX RCM ensemble is known to be more suitable for capturing heat extremes and their local impacts with reduced biases and uncertainties compared to CMIP5 GCMs[62, 63].

We note that the CMIP6 phase projects climate evolution using an extended set of future scenarios[64, 65]. In addition to RCPs, CMIP6 employs scenarios rooted in socioeconomic trajectories. These *Shared Socioeconomic Pathways* (SSP) complement RCPs via shared policy assumptions. This will yield more reasonable future trajctories.

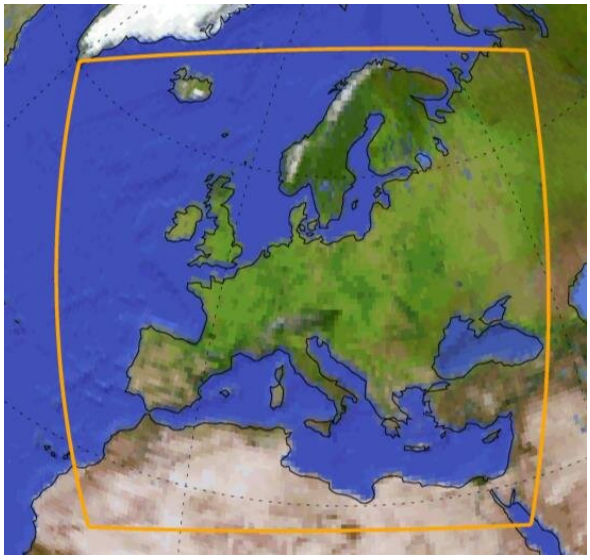

Figure 2.4: The EURO-CORDEX domain. Source: CORDEX (2024)[4].

In this study, a bias-corrected version of the EURO-CORDEX regional climate model ensemble is used to assess the return periods of selected extreme years, chosen for in-depth impact analysis of our primary results. The bias correction process results in an ensemble of GWL2.0 projections, which we pool into a single dataset for statistical analysis. Future heat extremes obtained through our data-mining approach will be evaluated against this bias-corrected dataset. The bias correction is not part of the thesis project, and the data is provided by the Belgian RMI.

2.2.4 Downscaled EURO-CORDEX Projections Over Brussels

The statistical-dynamical downscaling technique described in section 2.2.2 has been applied to EURO-CORDEX RCMs over the Brussels region by Duchêne et al. (2022) to produce an ensemble of 10 RCP8.5 simulations at the urban level[66]. These simulations boast a spatial resolution of 1 km and hourly outputs covering a 1971-2100 period. The calibrated regional projections are applied as the forcing for the *Land-Surface Model* (LSM) *Surface Externalisée* (SURFEX)[67]. The resulting time series were made available as spatial averages over the 19 communes that make up Brussels, but also at specific points that correspond to weather stations in the region[2].

[2] These weather stations are part of a Flemish citizen science project called VLINDER[68].

3 Methods

3.1 Mining Extremes: Basic Idea

As stated in section 1.3.1, storylines describing climate or weather extremes must provide realistic, plausible scenarios and circumstances. When looking for plausible heat extremes in a future climate, one could exploit the availability of large ensembles of global and regional climate model simulations spanning multiple socio-economic scenarios[64]. In a European context, the EURO-CORDEX ensemble is of particular interest as it comprises simulations with many RCMs coupled to several GCMs at a high-resolution of about 12.5 km[60]. Such climate simulation ensembles provide a comprehensive framework for assessing a wide range of possible future climates, allowing, in principle, for the study of extreme temperature events through *data-mining* approaches[35].

It is, however, not trivial to identify extreme heat events in projections from simulations corresponding to a specific counterfactual climate. Several methodologies are extensively described in the literature, such as ensemble boosting[69] or stochastic weather generators based on circulation analogues[30, 70]. In this thesis, years of extreme heat are identified in simulation data using climate-specific thresholds, which are determined via *Global Warming Scaling* (GWS).

3.2 Global Warming Scaling

3.2.1 Determining GWS Thresholds for Years of Extreme Heat

In section 1.2, we note that heat extremes do occur in Belgium, and they are expected to rise in frequency and severity as global warming continues. Historical records of these extremes are valuable to us when we want to construct realistic scenarios. We may attempt to transform such series to a counterfactual climate, and investigate temperature extremes in these modified series.

It is natural to regard extreme events as those for which one or several variables exceed a high threshold[71]. In this work, extreme heat events are identified as instances when these thresholds for several climate indices are simultaneously exceeded. We employ the method of GWS to robustly determine extreme-event thresholds in a specific counterfactual climate by modifying a standard bias-correction technique known as the delta-change method[72]. Both GCMs and RCMs exhibit systematic errors in their output, and bias correction methods serve to mitigate these[73]. The delta-change approach uses the GCM or RCM response to climate change to transform observed time series into future time series. In its most basic form, one first calculates the mean change in a climate variable, e.g. temperature, between the future period and historical reference period in the simulation. This change is then used to modify the observed time series. For instance, if the model predicts a 2 °C temperature increase, we add 2 °C to all historical observations, with the output being a new time series for a future climate.

We present a modified approach where the delta-change term is determined from observations directly, without input from simulations, to determine local thresholds for extreme heat events in a warmer climate characterised by a specific global mean surface temperature increase or GWL. As has been noted, there is a difference between global and local warming rates, so the translation between the two is absolutely necessary. This requires a *Local-to-Global Warming Ratio* (LGWR); the ratio between the warming rates at the local and global levels. Calculation of the LGWR is discussed in section 3.2.2. Once global warming can be translated to a *Local Warming Level* (LWL), the temperature delta-change term ΔT can be computed as the absolute difference between LWLs for a future period at a certain GWL and the historical period:

$$\Delta T = \text{LGWR} \times \left(\text{GWL}^{\text{CF}} - \text{GWL}^{\text{ref.}} \right) \tag{3.1}$$

where GWL^{CF} and $\text{GWL}^{\text{ref.}}$ respectively refer to the GWLs in the counterfactual climate and the climate of the reference period. This ΔT is then added to all temperature measurements of the historical period allowing us to delta-change any observed temperature time series to a warmer climate, as demonstrated in Figure 3.1.

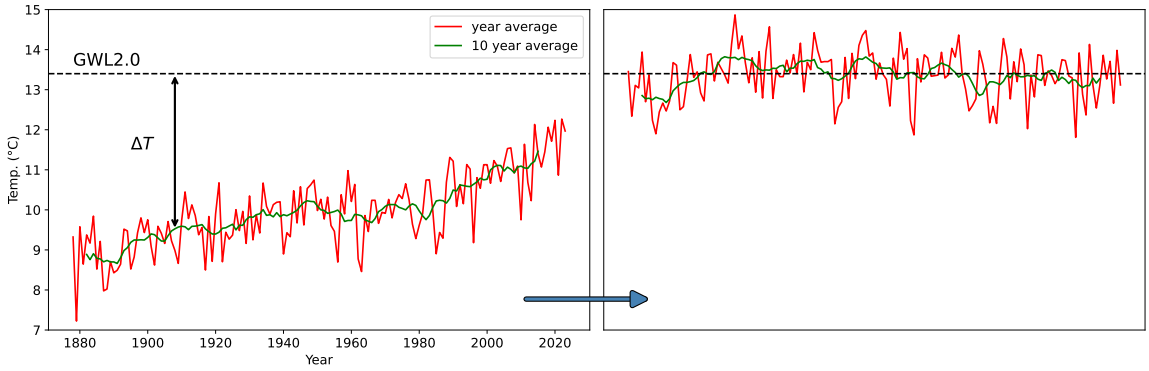

Figure 3.1: Illustration of the delta-change method to transform the observational temperature time series from Brussels (1878-2023) into a time series at GWL2.0.

The resulting output of this transformation to a counterfactual climate is a long series of temperatures that are assumed to be plausible in this particular climate. We may then source our thresholds from this transformed dataset, as is explained below.

The next step is to select climate indices that may act as indicators for the heat extremes we aim to characterise in this investigation. Important examples of such indicators on an annual basis, as used in this thesis, include[55, 74]:

- **Heat intensity (HI)**: the cumulative sum of positive differences between daily maximal temperature and the predefined threshold of 25°C, summed over the entire year. The heat intensity is a measure of the amount of time the temperature exceeds this threshold, and is expressed in Cooling Degree Days (CDD), as it is an indicator for air-conditioning and energy use.
- **Annual peak temperature ($T_{\mathbf{max}}$)**: the highest temperature reached during the year, expressed in °C. This parameter can be seen as an indicator of the *degree of tropicality* of heat extremes during the corresponding year.

Additional indices worth mentioning are:

- **Tropical Nights**: the total number of days in the year where the temperature did not fall below the predefined threshold of 20°C. This parameter can be important in assessing thermal discomfort during periods of elevated heat stress[75].
- **Heatwave days**: the length of the longest heatwave of the year, expressed in number of days. This parameter indicates the duration of the heat extremes.

For each of these annual indices, we determine respective extreme values in the transformed time series. These delta-changed historical extremes are then taken as the sought-after extreme-event thresholds. It may thus be understood that a year of extreme heat in the counterfactual climate under study is one for which the GWS thresholds of all relevant climate indices are exceeded. In this thesis, extreme-heat years are identified in projections from simulations using the GWS thresholds for HI and T_{max}.

3.2.2 The Local-to-Global Warming Ratio

It has been made clear that the application of the GWS scheme 3.1 requires the translation of global warming to local warming through the LGWR:

$$\text{LGWR} = \frac{\text{LWL}^2 - \text{LWL}^1}{\text{GWL}^2 - \text{GWL}^1} \tag{3.2}$$

Here, the superscripts 1 and 2 mark the start and end respectively of the reference period over which we determine the LGWR. There are several ways to determine such a ratio, and these methods should yield similar, but non-identical results, depending also on the intervals over which the local and global anomalies are averaged.

For the approach used in this thesis, the steps are outlined below:

1. The first step is to average both global and local anomalies over 10-year ranges. This reduces sensitivity to the choice of the range over which we calculate the ratios. GISTEMP v4 gives estimated values of the global surface temperature anomaly with respect to the 1951-1980 average. Local anomalies are determined from the observed temperature data provided by the RMI, averaged yearly, and given with respect to the calculated 1951-1980 Uccle average[1], so that the two sets of anomalies are comparable.
2. Next, a range of years is selected in which both the global and local temperature increases are approximately linear. We choose the range 1940 - 2018 for our analysis. Choosing 1940 as our starting year is sensible as we do not consider earlier events in determining the thresholds used for extreme event identification[2]. 2018, in turn, is simply the final year for which a 10-year average of the anomaly can be computed, given that the time domain of the used temperature datasets does not go beyond 2023.
3. Finally, we apply equation 3.2 to this range, and take the result to be the LGWR.

An apparent downside here is that we assume fixed warming rates, but the linear relation between LWL and GWL has been established worldwide[76]. The validity of the approach can be tested in several ways. If the assumption of approximate linearity in the chosen range is correct, a linear regression performed on the anomaly values should result in a good fit, and moreover, the ratio

[1] By the 1951-1890 period, RMI measurements had indeed been moved to Uccle, so it is appropriate to refer to an Uccle average.

[2] This is explained further in section 4.1.2.

between the slopes of both curves should match the obtained LGWR.

We determine the LGWR seperately for maximum, minimum and average temperature. It is expected that these quantities will scale differently with respect to the GMST anomaly[77, 78]. Indeed, in the latter half of the 20th century, a phenomenon known as *diurnal asymmetric warming* took place, wherein land surface temperatures increased more rapidly during the night than during the day, thereby decreasing the *Diurnal Temperature Range* (DTR)[78]. DTR changes are very complex and depend on many factors, such as cloud cover, aerosols and land use change. Recent studies even indicate a reversal of the asymmetric warming relative to the late 20th century[77]. Moreover, the phenomenon exhibits significant regional variations[79]. Series of daily maximum, minimum and average temperatures are therefore transformed separately according to their respective LGWRs.

3.3 Identifying Extreme Years in Ensembles

3.3.1 Two-Sample Kolmogorov-Smirnov Tests

The *Kolmogorov-Smirnov* (KS) test is a nonparametric test of the equality of one-dimensional probability distributions[80]. It can be used as a goodness-of-fit test, to determine whether two distributions differ, or to determine whether an underlying probability distribution differs from a hypothesised distribution. Traditional tests of this type like the Mann-Whitney test[81] detect differences between means or medians, but the KS test considers the distribution functions collectively.

For our purposes, the two-sample KS test is of great importance. Intuitively, this test tells us how likely it is that we would encounter two given sets of samples if they were drawn from the same (but unknown) probability distribution. It does this through the KS statistic, which quantifies a distance between the *empirical distribution functions* (EDFs) of the two samples.

Assume we have two general independent random samples. The first sample comes from population 1 and is denoted $(X_1, X_2, \ldots, X_n)$ and is of size n. The second sample $(Y_1, Y_2, \ldots, Y_m)$ is of size m and comes from population 2. The unknown distribution functions of populations 1 and 2 are respectively written as $G_1(x)$ and $G_2(x)$.

The to be tested hypotheses are the following:

$$\begin{aligned} &\mathbf{H_0} : G_1(x) = G_2(x)\ \forall x \\ &\mathbf{H_1} : G_1(x) \neq G_2(x) \text{ for at least one value of } x \end{aligned} \tag{3.3}$$

where H_0 represents the *null hypothesis* and H_1 the *alternative hypothesis*. In the case of the two-sided or two-sample KS test, the null hypothesis states that the two samples are drawn from the same distribution.

The statistical test $D_{n,m}$ itself is defined as the greatest vertical distance between the EDFs $F_{1,n}$ and $F_{2,m}$ of the two samples:

$$D_{n,m} = \sup_x |F_{1,n}(x) - F_{2,m}(x)| \tag{3.4}$$

Indeed, it follows from the *Glivenko-Cantelli Lemma* that $D_{n,m}$ will converge in probability to zero for large enough samples drawn from identical distributions[82]:

$$D_{n,m} \xrightarrow{\text{p}} 0 \text{ if } n, m \to \infty \tag{3.5}$$

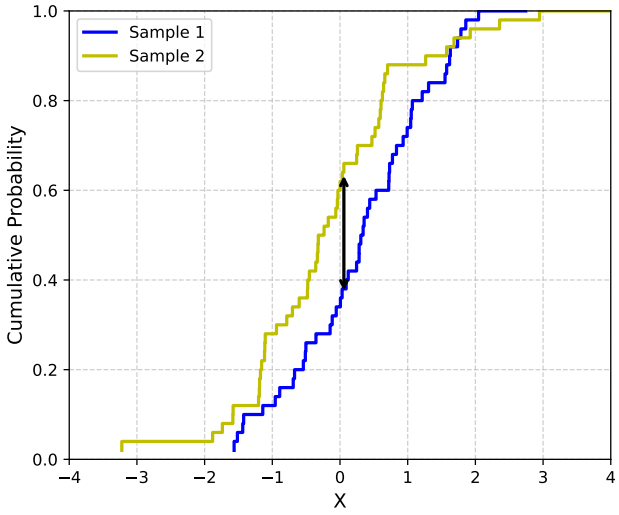

Figure 3.2: Illustration of the KS statistic as the maximal distance between the EDFs of two randomly drawn samples.

The KS statistic is visualised in figure 3.2. The null hypothesis H_0 is rejected at significance level α if this KS statistic $D_{n,m}$ is larger than the critical value $C_{n,m,\alpha}$. For sufficiently small sample sizes m and n, critical values at commonly used significance levels α are tabulated in so-called *Smirnov tables*[83]. For large sample sizes, we may use[82]:

$$C_{n,m,\alpha} = c(\alpha)\sqrt{\frac{n+m}{n \cdot m}} \tag{3.6}$$

where $c(\alpha)$ is the inverse of the *Kolmogorov distribution* at α. It can be calculated as follows[84]:

$$c(\alpha) = \sqrt{-\ln\left(\frac{\alpha}{2}\right) \cdot \frac{1}{2}} \tag{3.7}$$

We will use KS tests to select simulations from the ensembles whose historical runs produce temperatures with statistical properties comparable to the observed temperature series. The tests are performed using the `scipy.stats` Python module.

3.3.2 Selecting Simulations

It is clear from figure 3.3 that some simulation runs will be severely biased with respect to observed temperature series. To identify extreme heat years in projections from simulations, without resorting to rigorous bias correction methods, we first need to select those simulation runs which sufficiently well reproduce the statistical properties of historically observed temperatures. We probe the statistical similarity between simulated and observed distributions using two-sample KS tests, as introduced in section 3.3.1. We want to work with those simulation runs which can be assumed

to produce plausible future heat extremes or years of extreme heat. We therefore, for every run, perform three separate KS tests to compare daily maximum temperature (TX[3]), daily minimum temperature (TN) and annual HI between observed and simulated series over the period 1971-2023. Values for 1971-2005 are drawn from historical runs, while values for 2006-2023 are taken from RCP8.5 runs. Simulation runs not passing the testing phase are discarded for now.

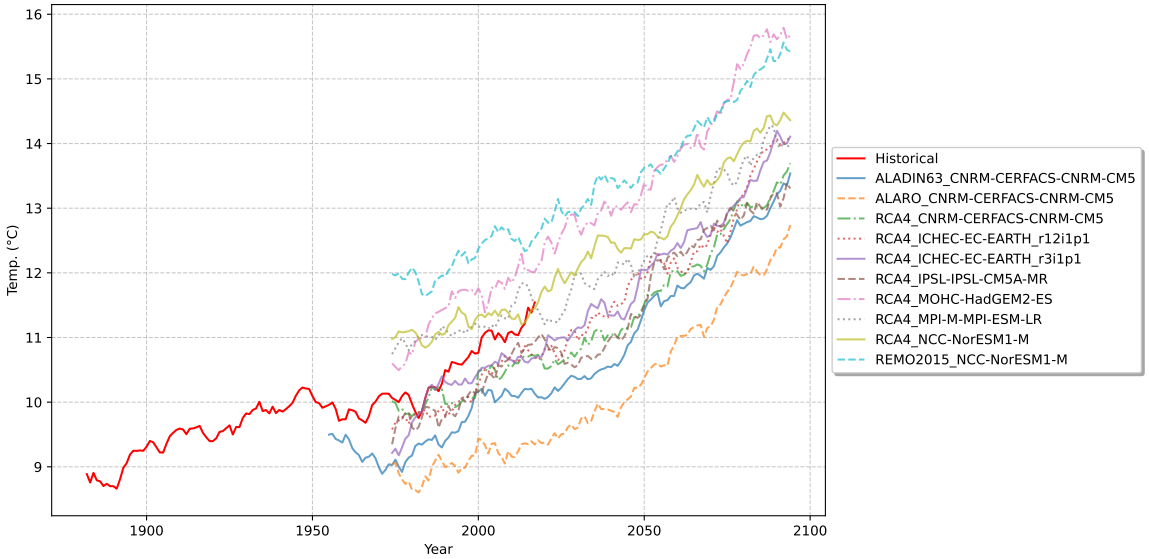

Figure 3.3: Illustrative plot of simulated temperatures compared to observed temperatures for the ten statistically-dynamically downscaled RCP8.5 runs over Brussels, averaged over ten years.

In order to make this selection of simulations, we need to formulate a criterion which marks sufficient agreement between observed and simulated distributions. For tests on the annual HI, both sample sizes are $n = m = 53$. This allows us to simply interpret equation 3.6 as the threshold for match failure, where we choose a significance level of $\alpha = 0.05$. The resulting KS statistic threshold is then 0.264. For the daily temperature tests, this choice is less straightforward due to the large sample size of several thousands of daily temperature measurements. It can be understood from equation 3.6 that for such large samples the null hypothesis will almost certainly be rejected at every meaningful significance level. This is because the KS test is designed to be sensitive to any differences between the distributions under comparison, no matter how trivial. $C_{n,m,\alpha}$ is therefore not a useful threshold in this case, and we can only choose a somewhat arbitrary value that is sufficiently low to distinguish those runs that best reproduce observed statistics from those that do not. In storyline research for the city of Paris, Yiou et al. (2024) worked with comparable daily temperature sample sizes and adopted a KS statistic threshold of 0.1[35]. We will use that same cut-off value in this study. An overview of sample sizes and KS statistic thresholds is given in table 3.1.

The simulation runs that survive the application of the three KS tests are assumed to produce plausible future events. We apply this simulation selection procedure to the EURO-CORDEX ensemble of RCP8.5 runs, as well as the ensemble of statistically-dynamically downscaled runs over Brussels.

[3]Not to be confused in notation with T_{max}, which indicates annual peak temperature.

Parameter	n	m	KS Threshold
HI	53	53	0.264
TX	19358	19358	0.1
TN	19358	19358	0.1

Table 3.1: Table of KS statistic thresholds for the parameters HI, TX and TN.

While rigorous and computationally expensive bias correction is avoided, a major downside of this method of selecting simulations is that biased simulation runs will be discarded, even though their output contains valuable trend information. For this reason, the selected simulations are complemented with time-shifted simulations.

3.3.3 Shifting Simulations

As explained, model simulations may be too strongly biased with respect to observed distributions and as such, we cannot assume their projections yield plausible future events in a warming climate. Bias correction quickly becomes cumbersome in storyline research, because of the need for multivariate modifications and for the correction of dependencies between variables[73].We implement a method that can avoid such difficulties by attempting to line up simulated distributions with similar observed distributions by shifting the simulated series along the time axis.

Instead of selecting simulations as described in section 3.3.2, we again consider simulation output in the form of daily temperature series, but now we look for a range of 53 years - anywhere along the time axis - that is consistent with observations of the recent past, which we again take to be 1971-2023. The degree of reproduction is assessed using KS tests on daily TX, daily TN and annual HI, with the KS statistic thresholds listed in table 3.1. If present, we choose the range that passes the KS tests while requiring the smallest possible time shift to do so.

If such a matching time window is found, we shift the entire temperature series along the time axis until this window is aligned with the recent past, and we look for years of extreme heat in the newly shifted projections for the near future. The shifting procedure is visualised in figure 3.4. If no matching window is found, the simulation run is discarded.

We apply the simulation shifting procedure to the EURO-CORDEX runs that were discarded during the simulation selection procedure because of their biases.

3.3.4 Identifying and Selecting Years of Extreme Heat

Once simulation runs have been selected, we can search for years of extreme heat in the corresponding projections. As stated in section 3.2.1, an extreme heat year is marked by the simultaneous exceedance of all relevant GWS thresholds. In this study, we will mine the ensembles for years where GWS thresholds for two annual parameters are exceeded: HI and T_{max}. We will collect all such years as they occur in the projections from both the EURO-CORDEX simulations ensemble and the ten statistically-dynamically downscaled EURO-CORDEX runs over Brussels. The latter are included because of their potential applicability in constructing storylines at the urban level.

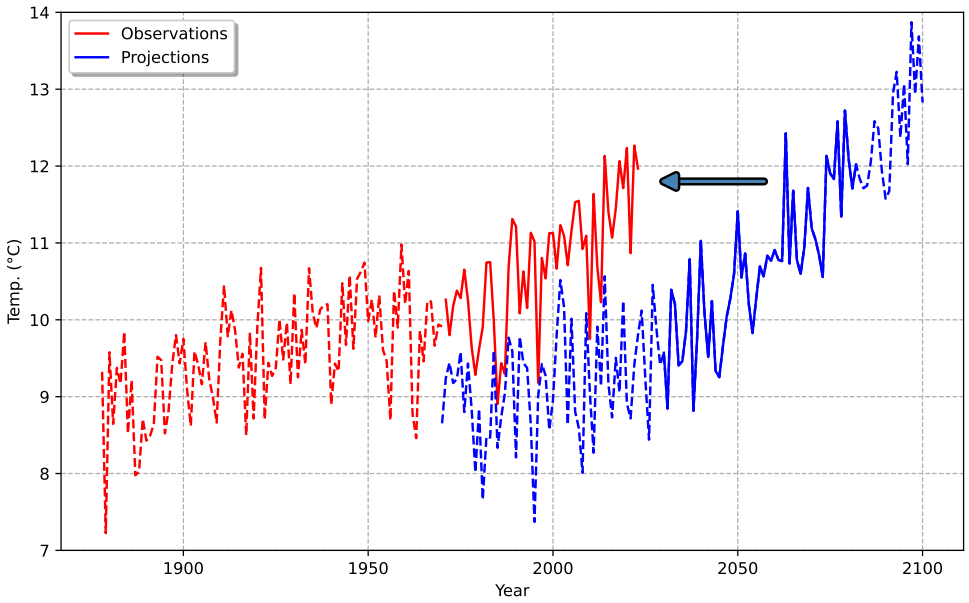

Figure 3.4: Illustrative plot of the procedure for shifting simulated series along the time axis.

To demonstrate applicability of the methodology, we select a year from these mined events that matches additional criteria and use the resulting data as input for some basic local impact models. A *worst-case* GWL2.0 year is chosen from all of the extreme years mined from the ensemble by identifying the first year for which GWS thresholds for tropical nights and heatwave days are also simultaneously exceeded. We refer to this example year as the worst-case year because it represents four scaled historical extremes compounded into a single GWL2.0 event, and the earliest plausible occurrence of such an event according to our analysis[4].

While valuable in some cases, the EURO-CORDEX runs with lower resolution of ∼50 km are excluded from this selection with the intent of obtaining more spatially detailed impact assessments.

3.4 Impact Analysis

As stated in section 1.5, we aim to construct concrete extreme-heat storylines for Belgium as a proof of concept to finalise the thesis investigation. This involves several impact models and calculations, the details of which are outlined in this section.

3.4.1 Heat Stress

Prolongued periods of extreme heat can pose a challenge to public health and civil protection services[85]. The most commonly used index to quantify *heat stress* is the so-called *Wet Bulb Globe Temperature* (WBGT)[86, 87]. WBGT is a combination of three local climate parameters: the natural

[4]The so-called worst-case year should evidently not be confused with the most extreme year mined from the ensemble.

wet bulb temperature (T_{nwb}), the globe temperature (T_g) and the air temperature (T_a). The outdoor WBGT - the version used in this work - is then given by the following relation:

$$\text{WBGT} = 0.7 \times T_{nwb} + 0.2 \times T_g + 0.1 \times T_a \tag{3.8}$$

Generally speaking, T_{nwb} and T_g are not regularly measured at weather stations due to the need for specialised equipment[86]. These fields are also not included in climate simulations output, so we need to resort to modelling approaches to assess heatstress during a simulated heatwave.

Many techniques have been proposed to calculate outdoor WBGT from meteorological data, and the most popular one is *Liljegren's method*[88, 89]. This iterative method uses heat exchange principles for the calculation of T_{nwb} and T_g. It requires air temperature, surface pressure, relative humidity, horizontal wind speed and shortwave radiation as input variables. The method has been extensively calibrated and validated to be accurate up to 1 °C[88]. We perform three-hourly, gridded WBGT calculations using the `PyWBGT` Python package[90]. These three-hourly results are then linearly interpolated to hourly WBGT data. A detailed mathematical formulation of the method can be found in appendix C.

3.4.2 Lost Working Hours

Exposure to extreme heat and excessive heat stress can greatly affect individuals performing physically demanding work[91]. It has been shown that future heat exposure will exceed critical levels for a physically active workforce significantly more often than in the current climate in large parts of Europe[92]. Under such conditions, labour productivity might experience consequential reductions. It is therefore interesting to model productivity losses during prolongued periods of extreme heat.

In this thesis, we model *Lost Working Hours* (LWH) as a function of WBGT. We make use of existing models for productivity losses in different environments and for different metabolic loads - which indicate how physically demanding the work is - based on ISO heat exposure metrics[93]. We compute hourly *workability* (WA) levels for a heavy workload (metabolic rate $M = 400$ W), which take on a value between 0 (indicating inability to work) and 1 (indicating no productivity loss). The workability is given by[94]:

$$\text{WA}_h = \max\left\{0; \min\left[1; \left(\frac{\text{WBGT}_{\text{lim, rest}} - \text{WBGT}_h}{\text{WBGT}_{\text{lim, rest}} - \text{WBGT}_{\text{lim}}}\right)\right]\right\} \tag{3.9}$$

where h denotes the hour of day and:

$$\text{WBGT}_{\text{lim}} = 34.9 - \frac{M}{46} \tag{3.10}$$

represents the threshold WBGT value, exceedance of which calls for a limitation of the working time to a fraction of the hour according to ISO standards, and $\text{WBGT}_{\text{lim, rest}}$ can be calculated using equation 3.10 for the resting metabolic rate $M = 117$ W[93].

We take *productivity losses* (PL) to be $\text{PL}_h = 1 - \text{WA}_h$ and given that these are calculated at hourly intervals we may simply sum the PLs during every working hour of the day to obtain daily LWH.

$$\mathrm{LWH}_d = \sum_{h \text{ in } d} PL_h = \sum_{h \text{ in } d} (1 - \mathrm{WA}_h) \tag{3.11}$$

LWH are evidently calculated at the same grid resolution as WBGT, and under the simplifying assumption that every day of the year is a potential work day with working hours between 6 h and 20 h.

3.4.3 Zeeschelde Water Temperatures

Water temperatures in rivers (and canals) are an important ecological parameter to study because of its influence on water quality and livability for aquatic organisms[95]. Strongly increased water temperatures in rivers or canals acting as sources for coolant near energy plants might have a severe impact on the efficiency of energy production[96, 97, 98]. For this reason, we will attempt to construct a model for water temperature in the Zeeschelde river, near the Belgian energy plants in Doel. The locations of interest are highlighted in figure 3.5.

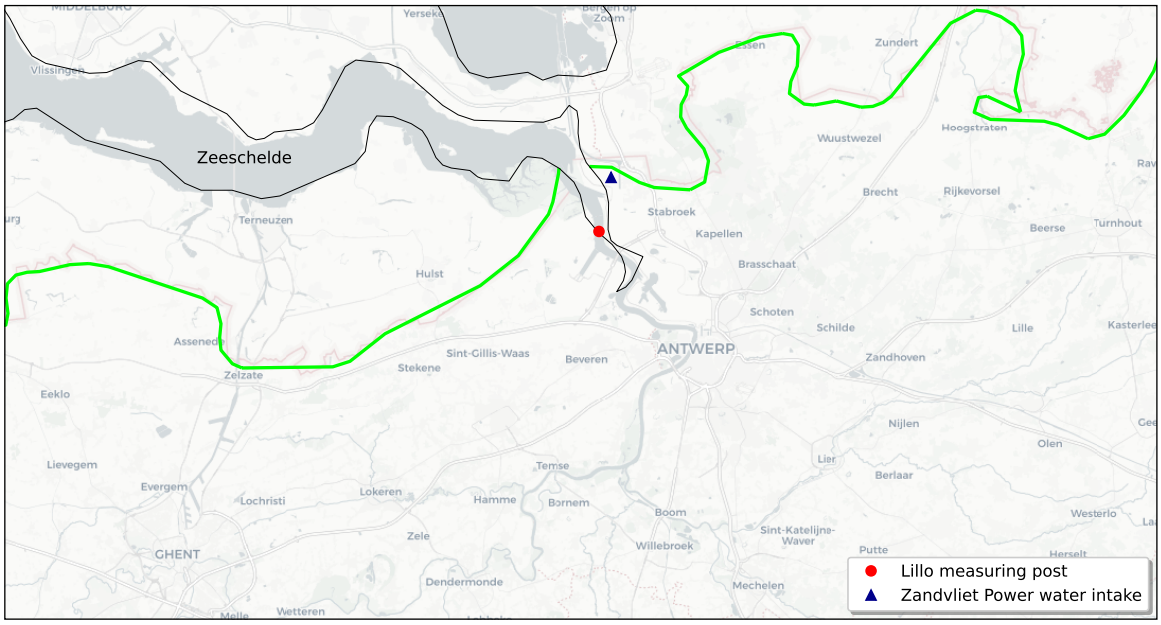

Figure 3.5: Map indicating the location of the Lillo measuring post in the vicinity of the energy plants in Doel.

We implement a multivariate linear regression model to estimate the temperature T_w of the Zeeschelde near the Lillo measuring post using several meteorological variables. Several similar models exist[99], and we have adopted some components of said models. Specifically, our model is of the form:

$$T_w = a + b \times T_a + c \times T_a^{30\mathrm{D}} + d \times S + \alpha \times \sin\left(\frac{2\pi}{365} N_\mathrm{D}\right) + \beta \times \cos\left(\frac{2\pi}{365} N_\mathrm{D}\right) \tag{3.12}$$

where T_a is the ambient air temperature, $T_a^{30\mathrm{D}}$ is the average air temperature during the previous 30 days and S is the mean daily downwelling shortwave solar irradiance. The fifth and sixth term on the right hand side of equation 3.12 represent seasonal variations in the water temperature of

the Zeeschelde, with N_{D} denoting the number of the day of the year (out of 365).

The model parameters are fitted using water temperature data from the Lillo measuring post from 1st October 2015 until 2nd February 2021. 20% of the sample data is randomly selected for testing the quality of the fit. These selected data entries are not considered during the fitting procedure. Fit quality is assessed by means of the *root mean square error* (RMSE) and R^2 coefficient.

3.4.4 Wildfire Hazard

While Belgium has generally not been regarded as a country prone to wildfires, a recent study by the Climate Risk Assessment Center in collaboration with the National Geographic Institute has highlighted the increasing risk of wildfires during extreme weather events exacerbated by climate change[100]. The report states that Belgium has no adequately coordinated wildfire management policies and that resources are insufficient. Moreover, the landscape is fragmented and natural areas are often nearby urban environments, adding to the societal threat. Assessment of wildfire hazard during future heatwaves in a storyline context is therefore an important addition to this study.

We will implement the Canadian Fire Weather Index (FWI) to assess the risk of wildfires for given meteorological conditions during the worst-case GWL2.0 year[101]. The diagram in figure 3.6 illustrates the determination of the FWI and its different components.

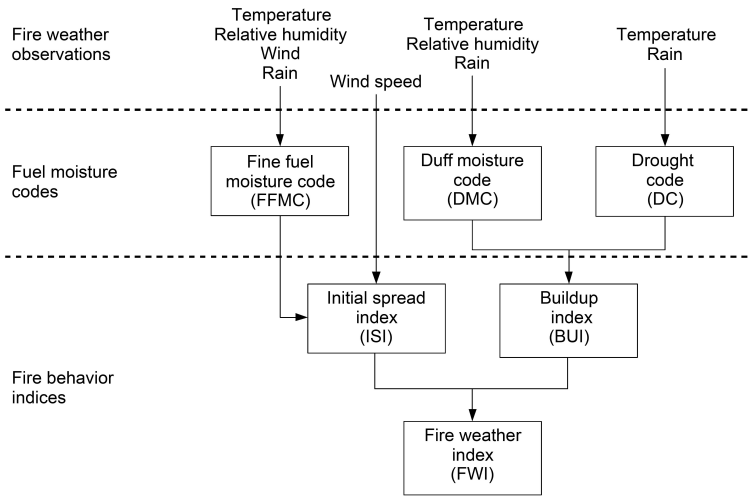

Figure 3.6: Schematic overview of the different components that make up the FWI. Source: Lehtonen et al. (2014)[5].

FWI calculations are not performed throughout the entire year, but start once the noon temperature exceeds 12 °C for three consecutive days, with the third day as the startup day. We end calculations on the last day of November. The main components are calculated based on consecutive daily observations of temperature (T), relative humidity (RH), surface (10 m) wind speed (U) and 24-hour precipitation (P).

Firstly, the *Fine Fuel Moisture Code* (FFMC) is a measure of the dryness of litter and small surface fuels, like grass or pine needles. The *Duff Moisture Code* (DMC) is a measure of the dryness of small subsurface organic material at moderate depth. The *Drought Code* (DC) is a numeric rating of the dryness of deep, compact organic layers. It is an important parameter in assessing seasonal drought effects on forest fuels.

The *Initial Spread Index* (ISI) represents the expected spread rate of a wildfire, right after ignition. It takes FFMC and wind speed into account, because dry fine fuels and high wind speeds will evidently increase spread rates. The *Buildup Index* (BUI) is a numeric rating of the total amount of fuel available for combustion, based on DMC and DC results.

Finally, ISI and BUI can be combined into the FWI, which measures wildfire hazard at the considered location under current meteorological conditions.

The components are an assessment of relative potential for wildfires, and explicit mathematical details regarding their calculation can be found in appendix D. We perform calculations using the `PyFWI` Python module.

3.4.5 Invasive Insect Species

Climate change has the potential to significantly influence the spread and dynamics of individual insect species. Specifically, rising temperatures may impact insect voltinism, which is the number of broods or generations of a particular organism that occur over a year[102], the assumption being that increased surface temperatures would permit multivoltine species to increase yearly generations[103].

We will investigate the voltinism of three non-native and invasive species of insects that pose a threat to Belgian agriculture. The brown marmorated stink bug (*Halyomorpha halys*) was first observed in Belgium in 2011 and feeds on fruit orchards and vegetable crops[104]. The Japanese beetle (*Popillia japonica*) and the false codling moth (*Thaumatotibia leucotreta*) are not known to be present in Belgium but have been identified elsewhere in Europe on native or imported crops[105, 106], and both species are included on the European Union's list of priority pests[107].

(a) (b) (c)

Figure 3.7: Illustrative photographs of the three invasive species under study: the brown marmorated stink bug (*Halyomorpha halys*) (a), the Japanese beetle (*Popillia japonica*) (b), and the false codling moth (*Thaumatotibia leucotreta*) (c). Source: USDA (2018)[6].

To model voltinism during a certain year, we require information about the developmental temperature thresholds for the species under study. `CLIMEX` is a niche software package developed with the aim of studying the effects of climate on invasive species[108]. `CLIMEX` models can be fitted to climate and species distribution data, and from this the developmental parameters can be obtained.

Such growth indices are the minimum temperature (DV0) and maximum temperature (DV3) for population growth, and the total amount of heat required for the growth of one generation (PDD). This last parameter is expressed in terms of *Growing Degree Days* (GDD). Given daily average temperatures T, we can calculate the total number of GDD across the studied year as follows:

$$\mathrm{GDD_{yr}} = \sum_{d} \Delta_d\left(T\right) \tag{3.13}$$

with:

$$\Delta_d\left(T\right) = \begin{cases} T - \mathrm{DV0} & \text{if DV0} < T < \mathrm{DV3} \\ 0 & \text{else} \end{cases} \tag{3.14}$$

The number of generations during said year may then simply be calculated as $\mathrm{GDD_{yr}}/\mathrm{PDD}$.

Species	DV0 (°C)	DV3 (°C)	PDD (GDD)
Brown marmorated stink bug	12.0	33.0	595
Japanese beetle	10.0	34.0	525
False codling moth	11.7	40.0	450

Table 3.2: Table of `CLIMEX` growth indices for the three invasive species under study: the brown marmorated stink bug (*Halyomorpha halys*), the Japanese beetle (*Popillia japonica*) and the false codling moth (*Thaumatotibia leucotreta*).

The literature already contains studies in which `CLIMEX` models are fitted for the brown marmorated stink bug[109], the Japanese beetle[110] and the false codling moth[111]. The resulting growth indices are listed in table 3.2. We will assess voltinism during the chosen worst-case GWL2.0 year for the three species using these adopted values.

3.4.6 Air Quality

Climate change is expected to directly impact air quality[112]. Ozone and particulate matter levels are strongly influenced by incoming radiation, temperature, wind and humidity. In general, pollution peaks coincide with stable atmospheric conditions. Heatwaves and atmospheric stagnation episodes favour air quality extremes. Increases in pollution can pose a severe threat to public health[113, 114] and even food security[115]. It is therefore relevant to assess pollution peaks. We do this by identifying days of atmospheric stagnation.

The most commonly used metric for identifying air stagnation conditions is the *Horton Air Stagnation Index* (H-ASI)[116]. According to the H-ASI, stagnant days exhibit weak near-surface and mid-tropospheric winds, as well as a lack of rainfall. Specifically, an H-ASI stagnant day is defined as one for which three conditions are simultaneously met[112]:

1. $P < 1$ mm.
2. $U < 3.2$ m/s.
3. $U_{500} < 13$ m/s.

with P the 24-hour precipitation, U the daily mean surface (10 m) wind speed, and U_{500} the daily mean 500 hPa wind speed. The H-ASI definition reflects the fact that rainfall and near-surface wind lower polluting particle concentrations through dissolution and advection, respectively. In this project, H-ASI stagnant days are identified for the chosen worst-case GWL2.0 year based on the data for P, U and U_{500} from the corresponding run, evaluated at the Uccle grid point.

3.4.7 Energy Consumption for Heating and Cooling

Climate change is expected to strongly affect energy demands for the heating and cooling of buildings[117]. It is therefore interesting to investigate energy consumption for cooling and heating during the worst-case GWL2.0 year. To this end, we simulate a medium-sized, single-story office building using the simulation software EnergyPlus[118]. The simulation setup and collection of the results is done using the OpenStudio platform[119].

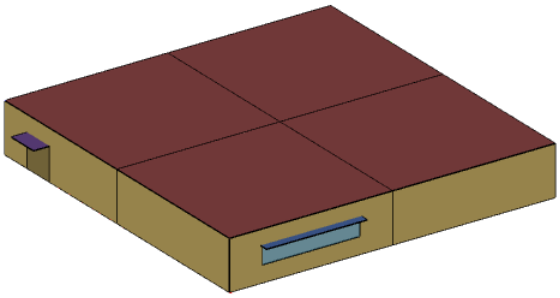

Figure 3.8: Geometry of the simulated medium-sized, single-story office building.

The simulated building covers a total surface area of 400 m^2 and is partitioned into four rooms of identical size. The building has one door, one window, and is constructed using conventional materials. The building has a regular packaged HVAC[5] unit, with cooling setpoint set to 23.5 °C, while the heating setpoint is set to 18.5 °C. The energy consumption and activity schedules are set to those of a typical medium-sized office space. The geometry of the building is shown in figure 3.8.

An *EnergyPlus Weather* (EPW) file is generated for Brussels using meteorological data from the chosen worst-case year. A reference EPW file for Brussels representing the late 20th century climate is built into OpenStudio. The latter file contains data from a series of hourly measurements on chosen days between 1983 and 1999, which are combined into a single dataset representing a hypothetical year. We simulate the energy consumption of the aforementioned building during the worst-case GWL2.0 year and the representative late 20th century year. In both simulations, the hottest and coldest days of the year are used as design days for automatically sizing the HVAC equipment.

3.5 Evaluating Global Warming Scaling via Extreme Value Theory

While the storyline approach, as explained in section 1.3, is inherently non-probabilistic and event-specific, we may benefit from an analysis of the statistical properties of, for example, the chosen worst-case GWL2.0 year. Calculating return periods of said year in the climate under study (GWL2.0) allows us to more clearly frame the relative extreme nature of the analysed event. The main parameter we use for assessing years of extreme heat is the HI, expressed in CDD. The parameter is introduced in section 3.2.1. We will investigate return periods and return levels of different HI values using *Extreme Value Theory* (EVT). The analysis is done using bias-corrected EURO-CORDEX runs for a GWL2.0 climate, which are described in section 2.2.3. A brief overview of relevant concepts from EVT is given in appendix B. Extreme value behaviour of the HI in GWL2.0 is investigated using the *Peaks-Over-Threshold* (POT) method. The optimal threshold is determined

[5] HVAC is a common abbreviation for Heating, Ventilation, Air Conditioning.

using mean residual life plots and parameter stability plots[6], and a GPD is fitted via maximum-likelihood estimation. We will then check the fit quality using diagnostic quantile plots and probability plots[80]. The quantile plot shows empirical quantiles against theoretical quantiles, while the probability plot compares the cumulative distribution function of the fitted GPD to the empirical cumulative distribution calculated from the data. If the fit quality proves satisfactory, return values and periods are calculated. Confidence levels for the return periods are obtained using a *bootstrapping* procedure[120, 121]. This involves resampling the exceedance data with replacement and refitting the GPD in each iteration using maximum-likelihood estimation. For each bootstrap sample, return periods are recalculated for a fixed set of HI values, generating a distribution of return period estimates. From these distributions, confidence intervals are derived by extracting percentiles corresponding to the desired significance level of $\alpha = 0.1$. The GPD function is called numerically from the `scipy.stats` Python module.

[6] See appendix B

4 Results

4.1 Global Warming Scaling Results

4.1.1 Local-to-Global Warming Ratios

Local T_{max} and T_{min} anomalies are compared to global GMST anomalies in figure 4.1. Anomalies for the average local temperature are not shown for clarity reasons. It is clear that the three different LGWRs will vary slightly.

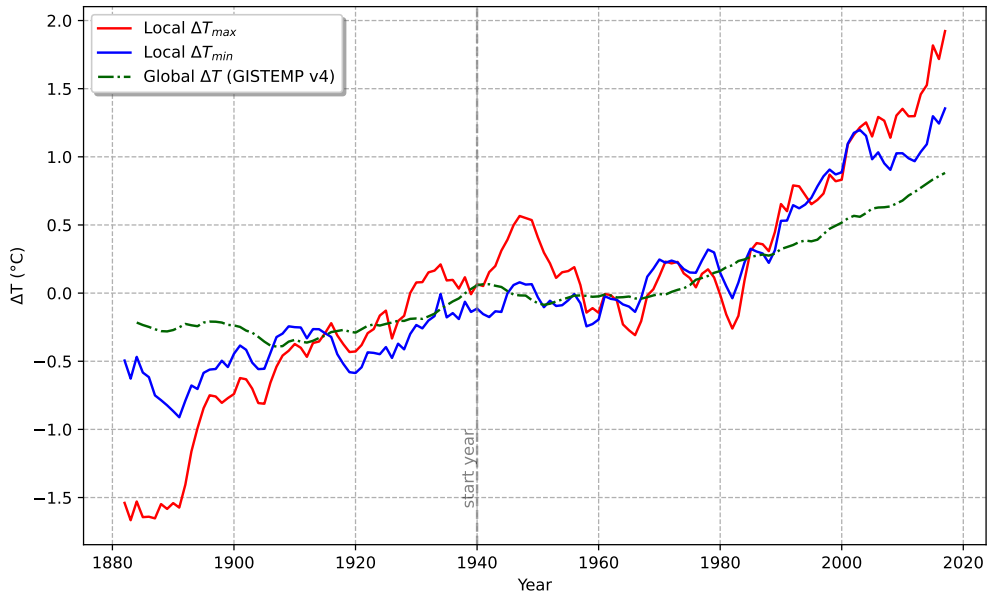

Figure 4.1: Plot of the local (Brussels) anomalies for T_{max} and T_{min} relative to the conventional 1951-1980 average, along with the global anomaly from GISTEMP v4, all represented as a centered 10-year moving average.

The computed LGWRs are given in table 4.1. These values indicate that T_{max} increases more rapidly with global warming than T_{min}. We find that local warming in Brussels is roughly twice as rapid as globally averaged warming, a ratio that is in agreement with a study of local warming for the Netherlands performed by the Royal Netherlands Meteorological Institute (2021)[122]. Before averaging them out over 10-year periods, a linear fit was also performed on the anomalies from 1940 onwards, and the LGWRs calculated from the fitted slopes are in agreement with the obtained values.

Parameter	1951-1980 average (°C)	LGWR	Linear fit result
T_{max}	13.54	2.25	1.90 ± 0.48
T_{min}	6.26	1.78	1.74 ± 0.38
T	9.90	2.02	1.82 ± 0.39

Table 4.1: Table of LGWRs for max. temperature T_{max}, min. temperature T_{min} and average temperature T.

4.1.2 Global Warming Scaling Thresholds

The Brussels temperature series is delta-transformed to a GWL2.0 climate, and this way we get adjusted series for our four relevant indices (HI, T_{max}, Tropical Nights and Heatwave Days), as shown in figure 4.2.

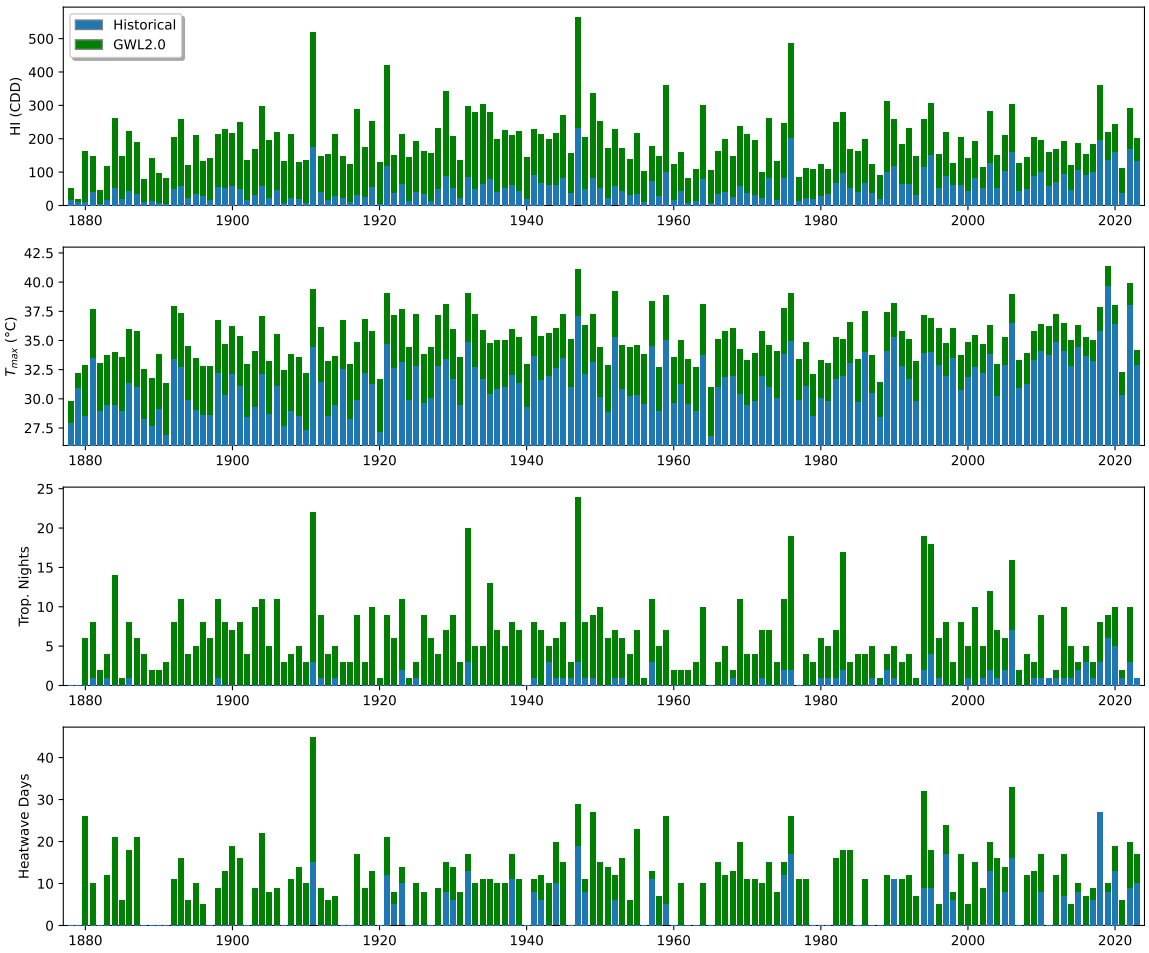

Figure 4.2: Results of the GWS delta-change transformation for HI, T_{max}, Tropical Nights and Heatwave Days.

Extremes of the transformed series, i.e. GWS thresholds, are listed in table 4.2. In determining these thresholds, we only took into account the transformed version of the time series from 1940 onwards. We list three reasons for doing so:

1. The translation of global to local warming is relatively robust in this period. During 1940-2018, warming shows approximately linear behaviour both locally and globally, as noted in section 3.2.2.
2. The further we look back in time, the larger uncertainties may be due to, for example, homogenisation issues, as explained in section 2.1.1.
3. As emphasised in Section 1.3, a key strength of the storyline approach lies in its ability to evoke the *episodic memory* of stakeholders, policymakers, and the general public by constructing plausible future weather events grounded in observed event-based science. Consequently, it is reasonable to exclude extremes from the distant past, as such events are beyond the lived experience of the current population and thus less likely to resonate.

Parameter	HI (CDD)	T_{max} (°C)	Trop. Nights	Heatwave Days
GWS Threshold	566.08	41.34	24	33

Table 4.2: Table of GWS Thresholds for HI, T_{max}, Tropical Nights and Heatwave Days.

4.2 Mining Years of Extreme Heat

4.2.1 Extreme-Heat Years for EURO-CORDEX Runs

The results of the KS testing procedure described in section 3.3.2 are listed in table 4.3 for the thirteen EURO-CORDEX runs that survive its application and are thus not discarded. As a visual consistency check, we show the annual average temperatures over the testing range for these runs in figure 4.3. It is clear that there are no clear biases, and the selected runs share the same temperature ranges as the observational series.

GCM	Member	RCM	Domain	D_{HI}	D_{TX}	D_{TN}
MOHC-HadGEM2-ES	r1i1p1	HIRHAM5 v1	EUR-11	0.245	0.059	0.075
MPI-M-MPI-ESM-LR	r3i1p1	REMO2015 v1	EUR-11	0.170	0.039	0.042
NCC-NorESM1-M	r1i1p1	REMO2015 v1	EUR-11	0.245	0.026	0.088
MOHC-HadGEM2-ES	r1i1p1	RACMO22E v2	EUR-11	0.151	0.049	0.089
MOHC-HadGEM2-ES	**r1i1p1**	**HadREM3-GA7-05 v1**	**EUR-11**	0.226	0.048	0.049
MPI-M-MPI-ESM-LR	r1i1p1	REMO2009 v1	EUR-11	0.151	0.045	0.048
MPI-M-MPI-ESM-LR	r2i1p1	REMO2009 v1	EUR-11	0.113	0.041	0.044
MPI-M-MPI-ESM-LR	r1i1p1	REMO2015 v1	EUR-22	0.132	0.040	0.056
NCC-NorESM1-M	r1i1p1	REMO2015 v1	EUR-22	0.245	0.026	0.100
MOHC-HadGEM2-ES	**r1i1p1**	**CCLM5-0-6 v1**	**EUR-44**	0.208	0.093	0.040
MPI-M-MPI-ESM-LR	r2i1p1	REMO2009 v1	EUR-44	0.231	0.064	0.073
CCCma-CanESM2	**r1i1p1**	**RCA4 v1**	**EUR-44**	0.212	0.071	0.051
MIROC-MIROC5	**r1i1p1**	**RCA4 v1**	**EUR-44**	0.173	0.055	0.055

Table 4.3: Kolmogorov-Smirnov test results for EURO-CORDEX runs. D_{HI}, D_{TX}, D_{TN} denote the KS statistic for the parameters HI, TX and TN respectively. Runs that exhibit extreme years, marked by the GWL2.0 GWS tresholds for HI and T_{max}, are highlighted in bold.

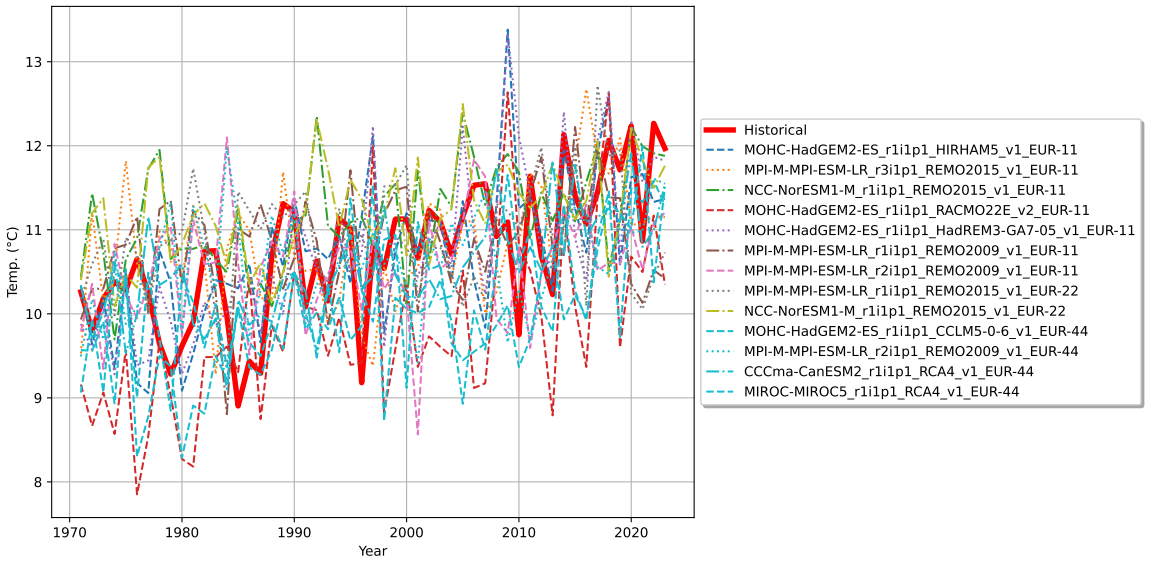

Figure 4.3: Comparison of annual average temperatures between observational series and surviving EURO-CORDEX runs, over the KS testing range.

The EURO-CORDEX runs that do not survive application of the selection procedure are subjected

to the shifting procedure in an attempt to find more usable runs. This yields an additional 31 shifted runs that reproduce observed distributions sufficiently well. The results for these runs are given in table 4.4.

GCM	Member	RCM	Domain	Years Shifted	D_{HI}	D_{TX}	D_{TN}
MPI-M-MPI-ESM-LR	r1i1p1	COSMO-crCLIM-v1-1	EUR-11	47	0.245	0.044	0.089
MPI-M-MPI-ESM-LR	r2i1p1	COSMO-crCLIM-v1-1	EUR-11	39	0.245	0.039	0.076
CNRM-CERFACS-CNRM-CM5	r1i1p1	CCLM4-8-17	EUR-11	44	0.094	0.099	0.072
ICHEC-EC-EARTH	r12i1p1	CCLM4-8-17	EUR-11	37	0.245	0.059	0.034
MPI-M-MPI-ESM-LR	r1i1p1	CCLM4-8-17	EUR-11	48	0.245	0.054	0.054
CNRM-CERFACS-CNRM-CM5	r1i1p1	ALADIN63	EUR-11	28	0.245	0.070	0.100
MOHC-HadGEM2-ES	r1i1p1	HIRHAM5	EUR-11	2	0.245	0.060	0.075
NCC-NorESM1-M	r1i1p1	WRF381P	EUR-11	7	0.245	0.059	0.045
CNRM-CERFACS-CNRM-CM5	r1i1p1	RACMO22E	EUR-11	69	0.245	0.029	0.029
ICHEC-EC-EARTH	r12i1p1	RACMO22E	EUR-11	66	0.245	0.052	0.044
ICHEC-EC-EARTH	r1i1p1	RACMO22E	EUR-11	61	0.245	0.046	0.053
ICHEC-EC-EARTH	r3i1p1	RACMO22E	EUR-11	49	0.245	0.057	0.066
IPSL-IPSL-CM5A-MR	r1i1p1	RACMO22E	EUR-11	45	0.245	0.074	0.065
MPI-M-MPI-ESM-LR	r1i1p1	RACMO22E	EUR-11	34	0.245	0.073	0.044
CNRM-CERFACS-CNRM-CM5	r1i1p1	RCA4	EUR-11	58	0.245	0.033	0.032
ICHEC-EC-EARTH	r12i1p1	RCA4	EUR-11	51	0.245	0.054	0.056
ICHEC-EC-EARTH	r1i1p1	RCA4	EUR-11	27	0.245	0.069	0.083
ICHEC-EC-EARTH	r3i1p1	RCA4	EUR-11	45	0.245	0.055	0.054
IPSL-IPSL-CM5A-MR	**r1i1p1**	**RCA4**	**EUR-11**	24	0.245	0.100	0.089
MPI-M-MPI-ESM-LR	r1i1p1	RCA4	EUR-11	38	0.245	0.059	0.061
MPI-M-MPI-ESM-LR	r2i1p1	RCA4	EUR-11	42	0.245	0.073	0.071
MPI-M-MPI-ESM-LR	r3i1p1	RCA4	EUR-11	34	0.245	0.070	0.055
NCC-NorESM1-M	r1i1p1	RCA4	EUR-11	49	0.245	0.098	0.097
MPI-M-MPI-ESM-LR	r1i1p1	CCLM4-8-17	EUR-44	65	0.245	0.061	0.077
MIROC-MIROC5	r1i1p1	CCLM5-0-6	EUR-44	14	0.245	0.086	0.060
MPI-M-MPI-ESM-LR	r1i1p1	REMO2009	EUR-44	6	0.245	0.046	0.088
CSIRO-QCCCE-CSIRO-Mk3-6-0	**r1i1p1**	**RCA4**	**EUR-44**	4	0.189	0.099	0.084
ICHEC-EC-EARTH	r12i1p1	RCA4	EUR-44	50	0.245	0.082	0.056
IPSL-IPSL-CM5A-MR	**r1i1p1**	**RCA4**	**EUR-44**	32	0.208	0.100	0.062
MPI-M-MPI-ESM-LR	**r1i1p1**	**RCA4**	**EUR-44**	15	0.245	0.095	0.043
NOAA-GFDL-GFDL-ESM2M	r1i1p1	RCA4	EUR-44	69	0.245	0.095	0.046

Table 4.4: Kolmogorov-Smirnov test results for shifted EURO-CORDEX runs. D_{HI}, D_{TX}, D_{TN} denote the KS statistic for the parameters HI, TX and TN respectively. Runs that exhibit extreme years, marked by the GWL2.0 GWS tresholds for HI and T_{max}, are highlighted in bold.

Once a selection is made of simulation runs - both shifted and unshifted - that reproduce historically observed ranges, one can identify years of extreme heat in the projections from those runs using the GWS thresholds reported on in section 4.1.2. The results are listed in table 4.5, excluding runs without extreme years. The upper part of the table contains extreme years mined from selected simulations, while the bottom part is dedicated to years mined from shifted simulations. For every identified year of extreme heat, we also log the GWL for that year. This GWL is calculated from the local temperature anomaly using the LGWR for average temperature T obtained in section 4.1.1. We thus calculate 10-year running averages of the projected local temperature anomaly relative to the observed, historical 1951-1980 Uccle average, and transform this to a global anomaly through division by the LGWR of 2.02. The GWL, being the anomaly with respect to pre-industrial levels, is then obtained by substracting the 1880-1909 average of such anomalies relative to the Uccle reference period.

GCM	Member	RCM	Domain	N	1st year	1st GWL
MOHC-HadGEM2-ES	r1i1p1	HadREM3-GA7-05 v1	EUR-11	18	2042	1.58
MOHC-HadGEM2-ES	r1i1p1	CCLM5-0-6 v1	EUR-44	3	2084	2.49
CCCma-CanESM2	r1i1p1	RCA4 v1	EUR-44	4	2086	2.63
MIROC-MIROC5	r1i1p1	RCA4 v1	EUR-44	1	2087	2.18
IPSL-IPSL-CM5A-MR	r1i1p1	RCA4 v1	EUR-11	2	2053	1.98
CSIRO-QCCCE-CSIRO-Mk3-6-0	r1i1p1	RCA4 v1	EUR-44	6	2060	1.67
IPSL-IPSL-CM5A-MR	r1i1p1	RCA4 v1	EUR-44	1	2045	2.02
MPI-M-MPI-ESM-LR	r1i1p1	RCA4 v1	EUR-44	1	2070	2.83

Table 4.5: Overview of results for extreme year identification in projections from selected (top part) and shifted (bottom part) EURO-CORDEX runs. N is the total number of identified extreme years.

4.2.2 Extreme-Heat Years for Statistically-Dynamically Downscaled Runs

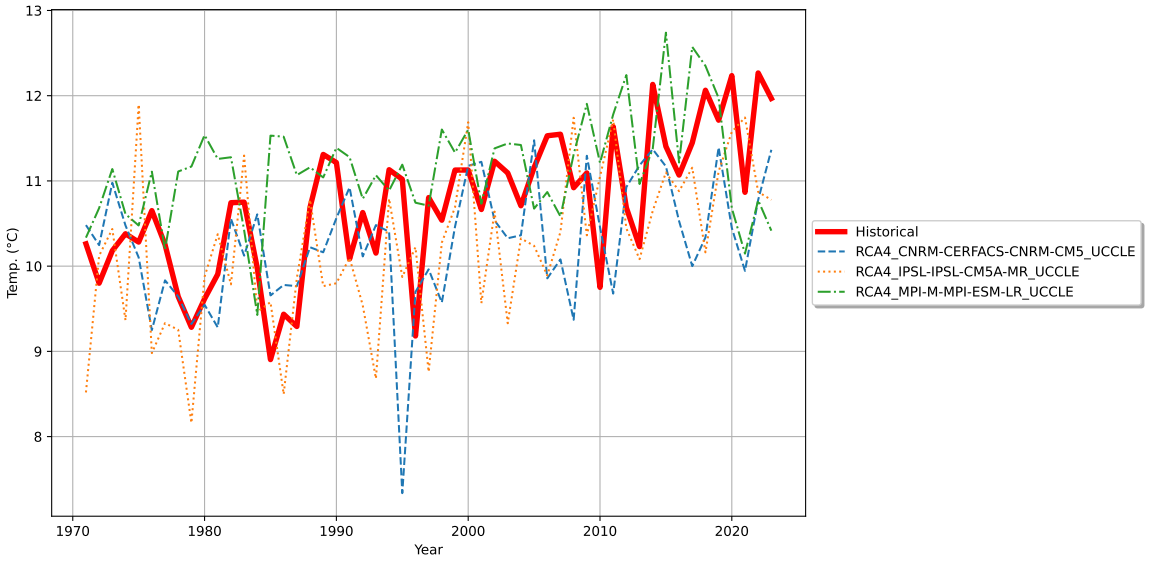

Figure 4.4: Comparison of annual average temperatures between observational series and surviving statistically-dynamically downscaled EURO-CORDEX runs, over the KS testing range.

We report on the results for extreme event identification in projections from statistically-dynamically downscaled EURO-CORDEX runs over the Brussels region in an identical fashion. Results for the KS testing procedure are shown in table 4.6 and figure 4.4. The ensemble consists of only 10 simulation runs, and the number of runs that agree with observed distributions is evidently lower than for the full EURO-CORDEX ensemble. The selected runs are not simply the downscaled versions of the surviving EURO-CORDEX runs, because the downscaling procedure introduces a temperature bias.

Extreme years are identified using GWS thresholds for HI and T_{max}. The results are listed in table 4.7.

GCM	RCM	D_{HI}	D_{TX}	D_{TN}
CNRM-CERFACS-CNRM-CM5	RCA4	0.132	0.038	0.058
IPSL-IPSL-CM5A-MR	**RCA4**	0.189	0.078	0.073
MPI-M-MPI-ESM-LR	**RCA4**	0.094	0.051	0.050

Table 4.6: Kolmogorov-Smirnov test results for downscaled EURO-CORDEX runs over Brussels. D_{HI}, D_{TX}, D_{TN} denote the KS statistic for the parameters HI, TX and TN respectively. Runs that exhibit extreme years, marked by the GWL2.0 GWS tresholds for HI and T_{max}, are highlighted in bold.

GCM	RCM	N	1st year	1st GWL
IPSL-IPSL-CM5A-MR	RCA4	2	2077	1.77
MPI-M-MPI-ESM-LR	RCA4	2	2085	2.20

Table 4.7: Overview of results for extreme year identification in projections from selected downscaled EURO-CORDEX runs. N is the total number of identified extreme years.

4.2.3 Summary and Worst-Case Year Selection

A summary of all the obtained years of extreme heat is shown in figure 4.5. It may appear from this figure that the shifting procedure samples extreme years that are mostly concentrated at the lower GWLs. This is because a shifted series does not cover the full temporal range up to 2100, so that shifted runs generally do not reach the same GWLs as selected runs, and events are necessarily identified at earlier levels. We note that many of the simulation runs that do pass the initial selection or shifting procedure do not yield extreme years. This potentially implies that climate simulations might underestimate heat extremes in Europe. We expand on this idea in section 6.

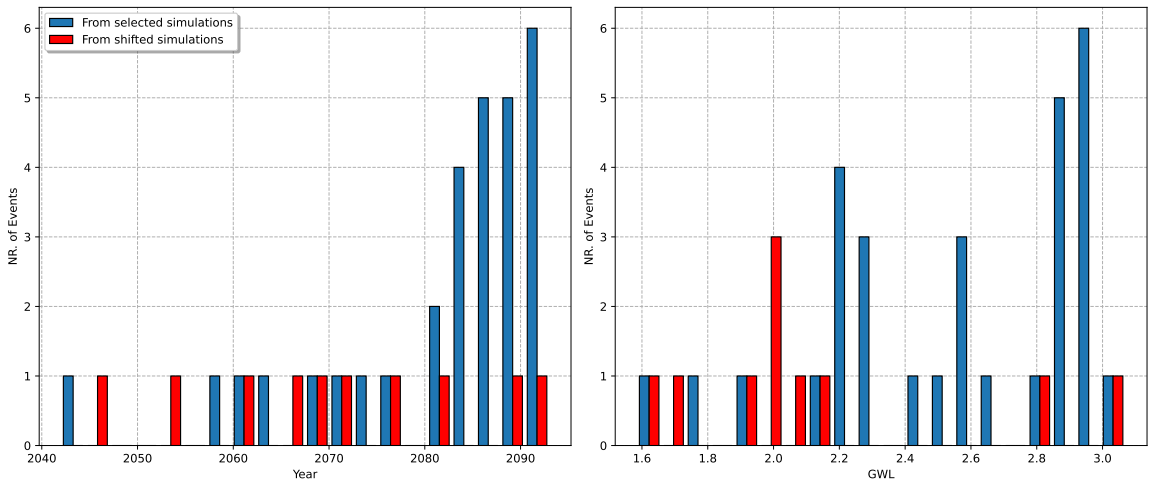

Figure 4.5: Overview of all the obtained years of extreme heat, marked by exceedance of GWL2.0 GWS thresholds for HI and T_{max}.

Across the remaining (high-resolution) simulation runs, the first occurrence of an extreme year for which GWS thresholds for tropical nights and heatwave days, as listed in table 4.2, are also simultaneously exceeded is the year 2059 from the RCP8.5 run of the RCM HadREM3-GA7-05 v1 (EUR-11) coupled to MOHC-HadGEM2-ES (r1i1p1). This year is thus selected as a plausible extreme heat year for Belgium in GWL2.0, during which all relevant climate indices cross their respective GWL2.0

thresholds, resulting in a hypothetical worst-case scenario compound event occurring in the near future. We will perform a concrete, storyline-oriented investigation of this particular worst-case year.

5 Analysis of the Worst-Case Year

We perform some general and impact analyses for the chosen worst-case year to probe the viability of the results from the GWS procedure. As explained at the end of section 4.2.3, we chose the year 2059 from projections of the RCP8.5 run of HadREM3-GA7-05 v1 coupled to MOHC-HadGEM2-ES for downscaling to a resolution of 12.5 km. Parameter values for this year are given in table 5.1, along with their respective differences to the GWS threshold values for GWL2.0. We note that the worst-case year is quite extreme in all parameters aside from T_{max}, even with respect to GWS thresholds. A simple back-translation from local to global warming using the LGWR for average temperature T from table 4.1 suggests a GWL of 2.13 °C for the chosen year 2059. We note once more that when we refer to 2059 in the following, we refer to the hypothetical worst-case year of extreme heat that results from the GWS procedure, and not the actual year itself, about which no claims or predictions are made.

Parameter	HI (CDD)	T_{max} (°C)	Trop. Nights	Heatwave Days
Value	610.85	41.75	34	48
GWS exceedance	44.77	0.41	10	15

Table 5.1: Table of key parameter values for the worst-case year and difference with GWS threshold values.

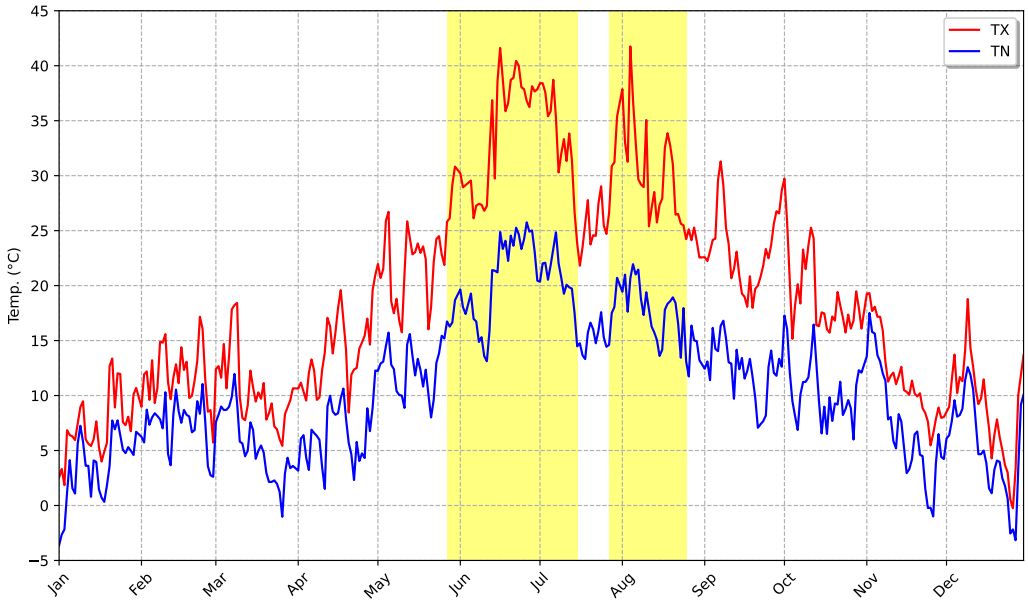

Figure 5.1: Plot of the local (Uccle) daily temperatures for the worst-case year 2059. The shaded yellow areas correspond to heatwaves according to the RMI definition.

TX and TN for 2025 are plotted in figure 5.1. We see that the summer months (JJA) are marked by two severe heatwaves. The first of these starts at the end of may and lasts 48 days, with the highest temperature (41.62 °C) being reached on the 16th of June. The second heatwave lasts 28 days, with

peak temperature (41.75 °C) being reached on the 4th of August. TX covering all of Belgium on these record days are shown in figure 5.2. It is clear that 40 °C temperatures are reached in large parts of Belgium. The extremeness of such temperatures can be understood through comparison with the highest TX ever recorded in Belgium, which is 41.8 °C as of 2025[123].

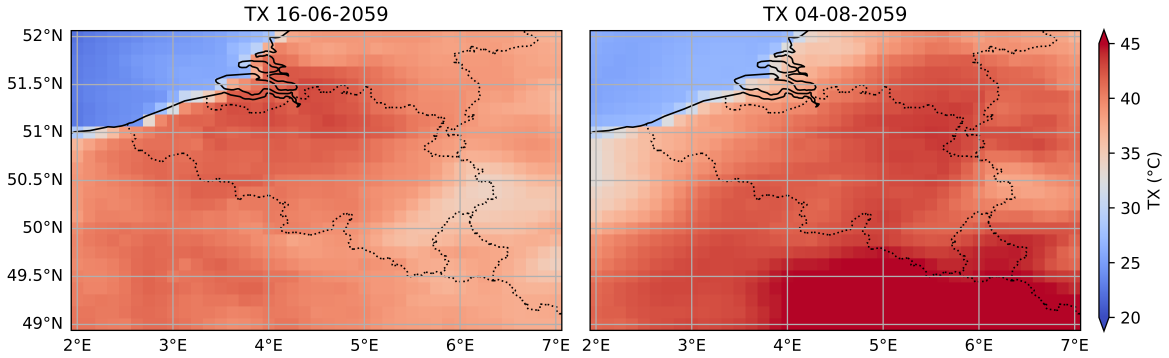

Figure 5.2: Map of TX values for every grid point covering Belgium on the hottest days of both heatwave periods.

To put these temperatures into perspective, we can make use of heat warning systems. In Belgium, two such systems exist: a heat plan developed by the federal government and a heat warning system developed by the RMI. We identify the different warning phases for 2059 and compare to the historically extreme year of 1976. We implement the warnings based on Uccle temperatures.

5.1 Heat Warning Systems

5.1.1 Federal Heat and Ozone Plan

We may start by investigating the different phases of the federal heat warning plan[124]. Development of the plan was prompted by the European heatwave of 2003. The current version of the plan dates from 2017. It is based on critical levels for both temperature as well as ozone concentrations, but for our purposes we only focus on the heat-related criteria of the plan.

The plan itself consists of three phases:

1. A monitoring phase (Normal)
2. A warning phase (Warning)
3. An alarm phase (Alarm)

which are declared when a specific set of criteria is met. Coordination of the corresponding measures are the responsibility of the regions (warning phase) or the federal authorities (alarm phase). The criteria are listed below:

1. The monitoring phase is the default phase which is automatically declared from the 15th of May until and including the 30th of September. It remains active while conditions for the other phases are not met.

2. The criterion for the warning phase is based on a temperature threshold. Specifically, this phase is declared when $T_{cum} \geq 17$ °C on the current day (D0). Here, the T_{cum} is the predicted HI across the next five days (D1 - D5) expressed in CDD. The warning phase is called off when $T_{cum} < 17$ °C on the current day and the predicted TX for D3 is below 25 °C.
3. The alarm phase is active while, simultaneously, the temperature threshold for the warning phase is met and TX ≥ 28 °C on D0.

We note that the actual alarm phase criterion is in fact more strict than the one presented here, because it includes additional ozone concentration thresholds as well as subjective evaluation criteria of currently implemented measures. Our implementation only focuses on objective heat-related criteria.

An overview for the described above phases of the federal heat plan as they would be declared for the worst-case year 2059 is shown in figure 5.3, as well as a comparison with past notably extreme years 1976 and 2018.

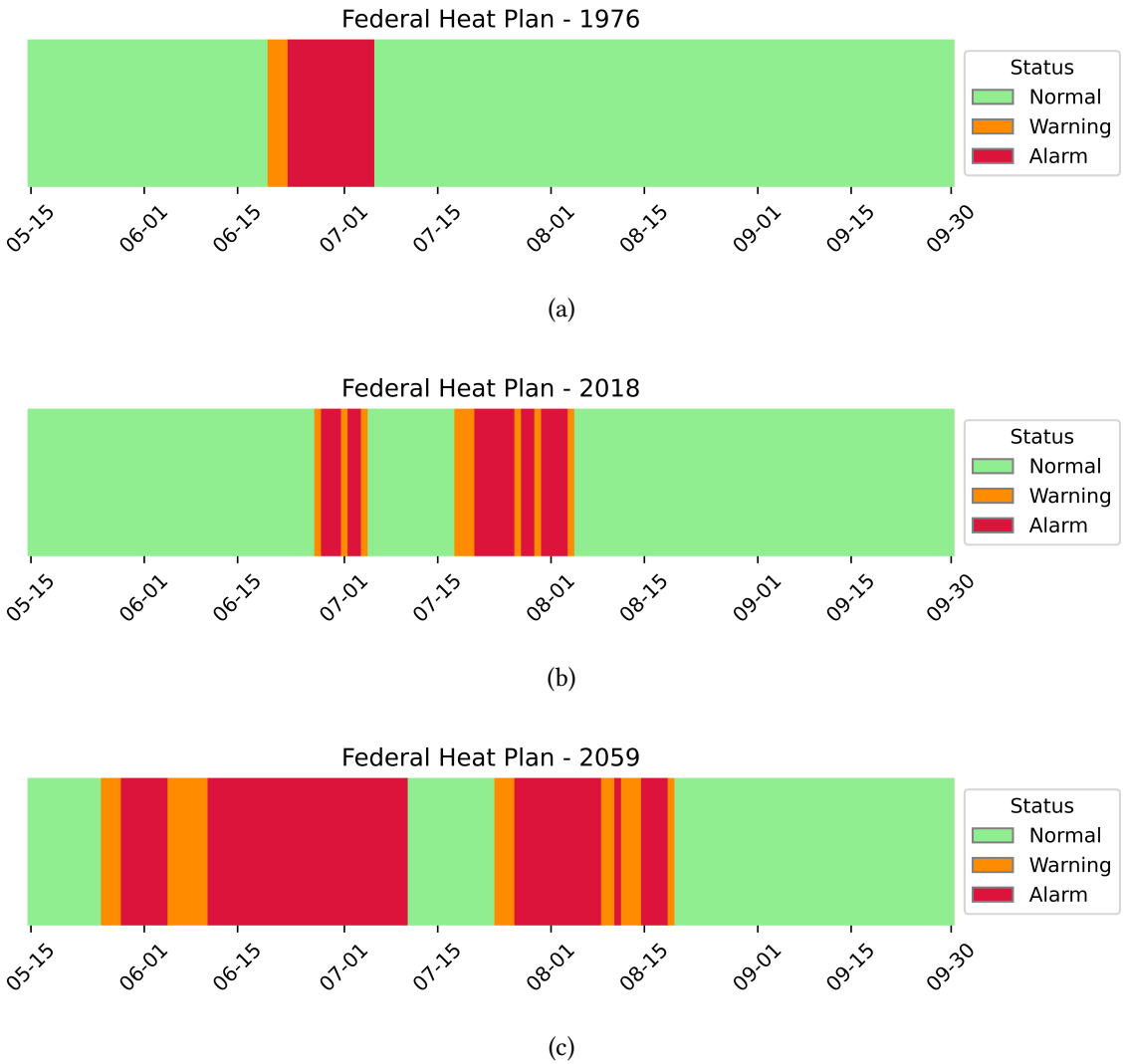

Figure 5.3: Overview of federal heat warning plan phases as they would be declared for the historically extreme years 1976 (a) and 2018 (b), and for the selected worst-case GWL2.0 year 2059 (c).

5.1.2 Royal Meteorological Institute Warnings

The Belgian RMI employs an alternative warning system[125]. It consists of four phases which are colour-coded:

- At code green no warning is activated.
- At code yellow, citizens are warned to be careful and measures should be taken to protect the elderly or other at-risk individuals.
- Code orange marks very high temperatures. At-risk individuals could benefit from measures such as wearing light clothing, drinking regularly, eating lightly, staying in a cooler place and keeping doors and windows shut. Citizens are advised to be careful and follow instructions from responsible authorities.
- Code red marks extremely high temperatures, and certain measures must be taken. Citizens are warned to stay hydrated, maintain salt content, stay restive in a cool place and avoid direct sunlight. Citizens should keep themselves and others safe and follow instructions from responsible authorities.

The different phases are defined in terms of heat-related criteria:

- Code green is the default phase.
- Code yellow is declared during a heatwave or when TX $\geq$ 32 °C.
- Code orange is declared during a heatwave when TX $\geq$ 32 °C for three successive days or when TX $\geq$ 35 °C.
- Code red is declared during a heatwave when TX $\geq$ 35 °C for three successive days or when TX $\geq$ 40 °C.

The RMI heat warning phases are declared per province separately. Here, we only look at the phases based on Uccle temperatures. These are shown in figure 5.4 for 2059, along with the results for 1976 and 2018 for comparison purposes.

It is clear from figures 5.3 and 5.4 that the worst-case year is one of prolonged extreme heat, and that the first heatwave especially would be significantly consequential. Such a year is thus well suited for stress-testing individual and societal resilience to unprecedented extremes in a GWL2.0 climate for Belgium.

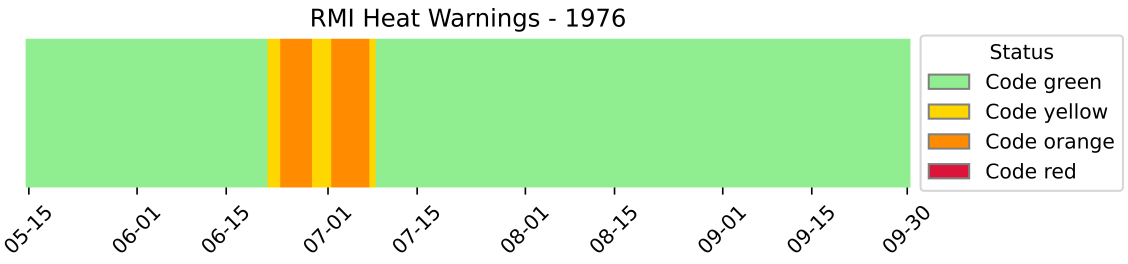

(a)

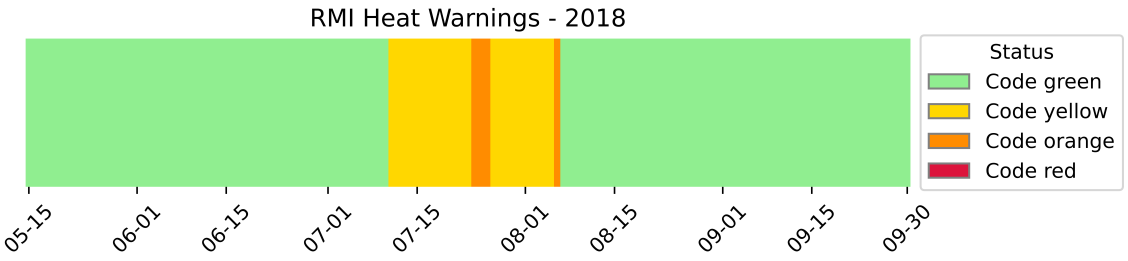

(b)

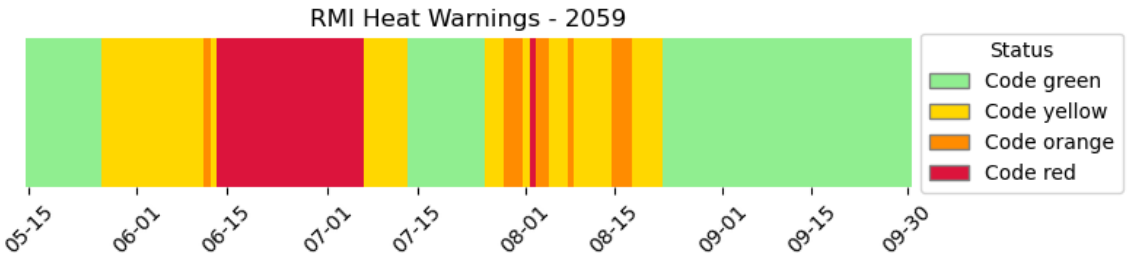

(c)

Figure 5.4: Overview of RMI heat warning phases as they would be declared for the historically extreme years 1976 (a) and 2018 (b), and for the selected worst-case GWL2.0 year 2059 (c).

5.2 Heat Stress and Productivity Losses

We now analyse the worst-case year in terms of heat stress. Results of WBGT calculations using Liljegren's method are shown in figure 5.5. This plot shows the daily maximum WBGT values for the worst-case year 2059, as well as for the historically extreme year 1976. The 1976 WBGT is modelled using meteorological data from ERA5, a gridded reanalysis dataset introduced in section 2.1.5. The coloured ranges in the background of the plot indicate recommended maximal exposure levels for average individuals unacclimatised to heat performing activities at different metabolic rates M, according to ISO 7243[93]. This figure makes clear that during most of the summer months (JJA), the worst-case GWL2.0 year exhibits much higher WBGTs than the historically extreme year.

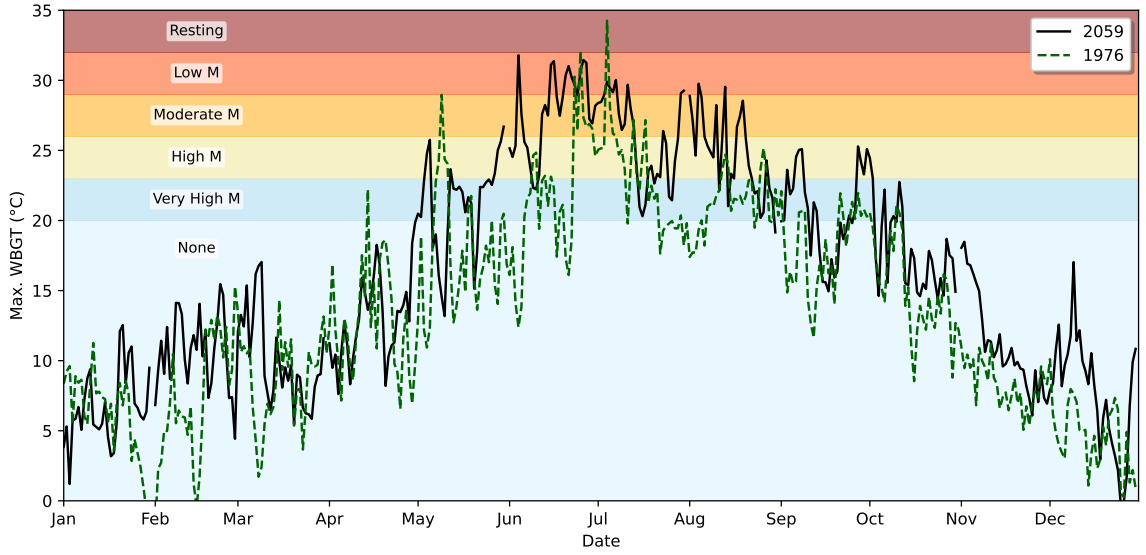

Figure 5.5: Plot of daily max. WBGT values for the worst-case year 2059 and the historically extreme year 1976. Background colors indicate recommended maximal exposure levels for different metabolic rates M, according to ISO 7243.

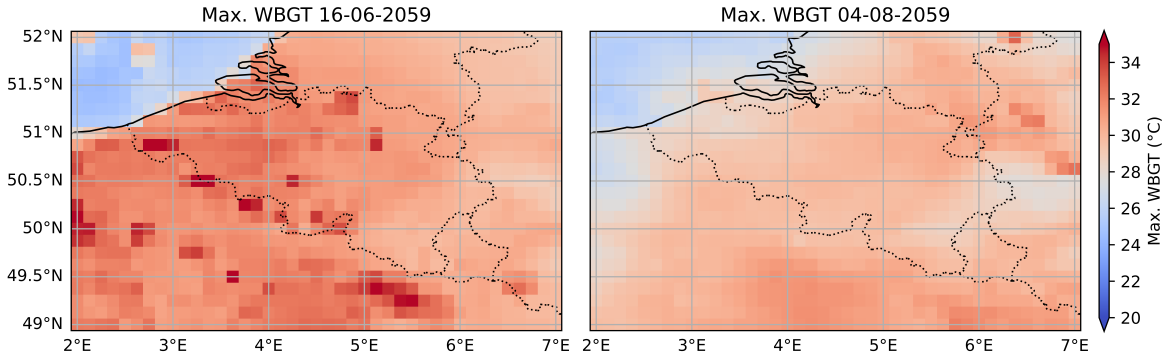

Figure 5.6: Map of Max. WBGT values for every grid point covering Belgium on the hottest days of both heatwave periods.

Figure 5.6 shows maps of maximum values for the WBGT index for every grid point in the relevant domain covering Belgium. We observe relatively severe WBGT values in most parts of Belgium. Urban effects, which are not resolved in EURO-CORDEX runs, are expected to exacerbate extreme heat stress and its effects[3]. The prolonged periods of extreme heat stress suggest significant pro-

ductivity losses for heavy outdoor work, which we may now verify using the modelling approach described in section 3.4.2 and the already calculated WBGT index values.

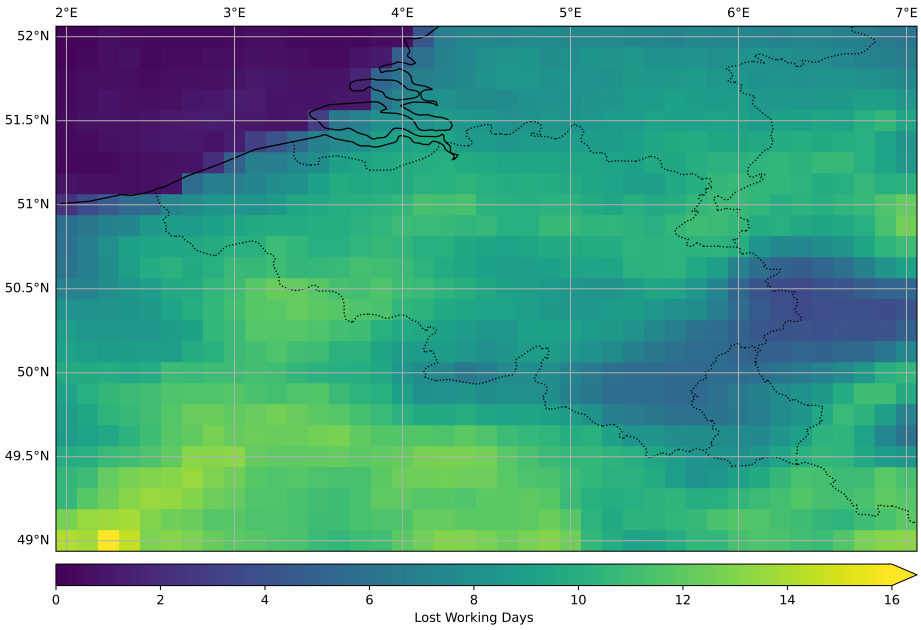

Figure 5.7: Map of lost working days across the entire worst-case year for every grid point.

Figure 5.7 shows the total loss of productivity for Belgium during the worst-case year in the form of *lost working days*, which is the summed LWH_d divided by 14, the number of working hours per day assuming a potential work day takes place between 6 h and 20 h. Note that this is a simplified result, in the sense that we do not account for varying work hours, foreseen breaks or holidays. The results therefore represent an upper limit relative to these restrictions. On the other hand, the results may be exacerbated when urban effects are taken into account.

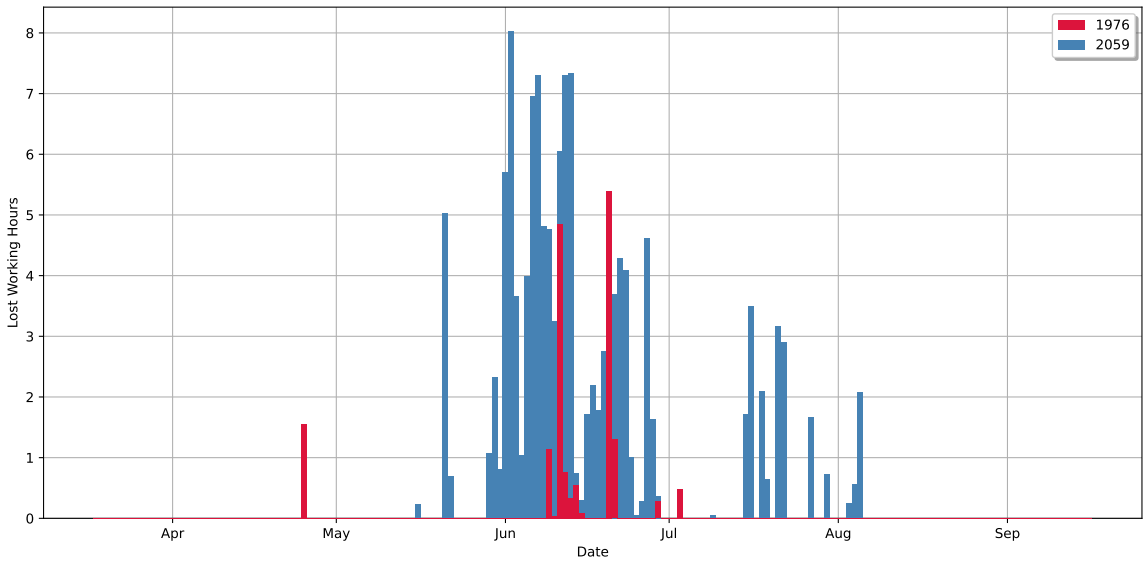

Figure 5.8: Plot of LWH_d in Uccle for the worst-case year 2059 and for 1976. No nonzero values occur outside of the displayed range of dates.

Productivity losses are far more severe than in previous extreme years, such as 1976. The total LWH across the entire worst-case year evaluated in Uccle amounts to **133.3 hours**, which is equivalent to 9.5 lost working days in total. This is much higher than the result of the Uccle LWH calculation for 1976, which yields a total of **16.8 hours**, or 1.2 days. An overview of this comparison is given in figure 5.8.

5.3 Zeeschelde Water Temperatures

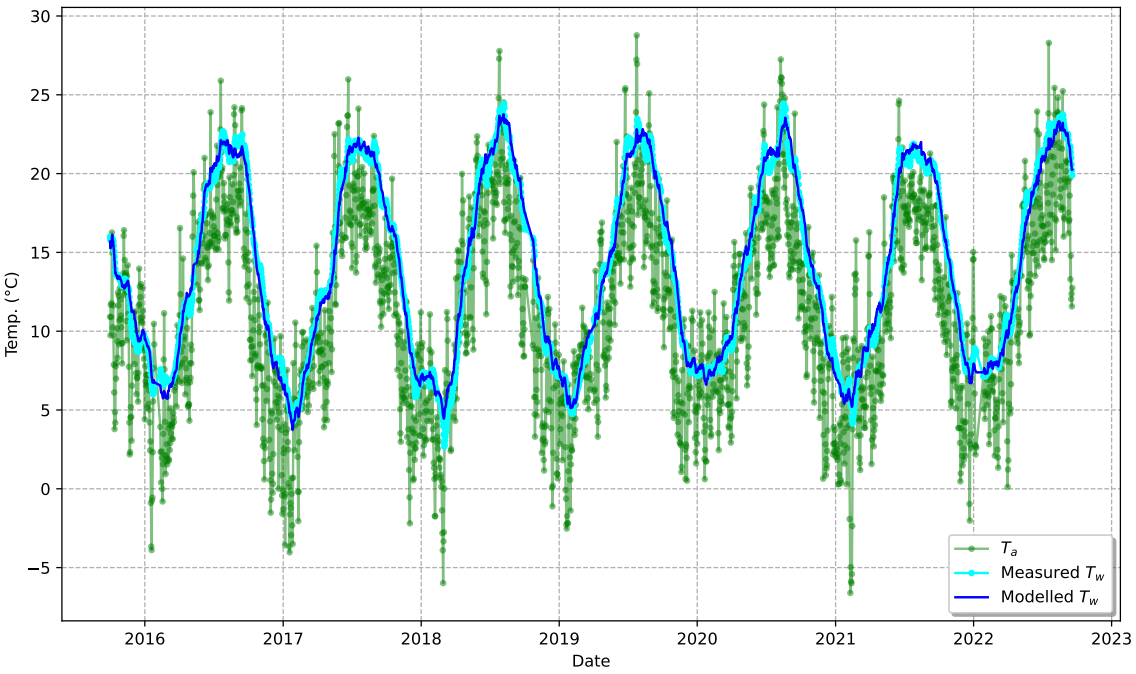

Figure 5.9: Plot of modelled and measured water temperatures for the Zeeschelde at the Lillo measuring post, along with measured local air temperatures for reference.

We can now investigate Zeeschelde temperatures during the worst-case year 2059 using the model introduced in section 3.4.3, which is of the form:

$$T_w = a + b \times T_a + c \times T_a^{30\mathrm{D}} + d \times S + \alpha \times \sin\left(\frac{2\pi}{365} N_{\mathrm{D}}\right) + \beta \times \cos\left(\frac{2\pi}{365} N_{\mathrm{D}}\right) \tag{5.1}$$

We recall that T_a is the air temperature on the current day, $T_a^{30\mathrm{D}}$, the average air temperature of the previous 30 days, S is the surface shortwave solar irradiance on the current day and the final two terms in equation 5.1 represent seasonal variations. The model is fitted using available data from the Lillo measuring post as described in sections 2.1.3, 2.1.4 and 3.4.3. Results for the fitted parameter values are listed in table 5.2. When applied to and evaluated against the testing portion of the data, the RMSE was found to be 0.60 °C, and the model achieved $R^2 = 0.99$. This proves that the model reliably estimates Zeeschelde water temperatures based on available meteorological variables. The quality of the model fit is visualised in figure 5.9, where available T_w measurements from the Lillo post are compared against output of the model using E-OBS data from the corresponding grid point.

Parameter	a (°C)	b	c	d (°Cm^2W^{-1})	α (°C)	β (°C)	RMSE (°C)	R^2
Value	14.17	0.26	2.93	0.13	1.29	2.25	0.60	0.99

Table 5.2: Table of fitted parameter values (left part) and fit quality metrics (right part) for the Zeeschelde T_w model.

The model can now be applied to the worst-case year 2059. The result is shown in figure 5.10.

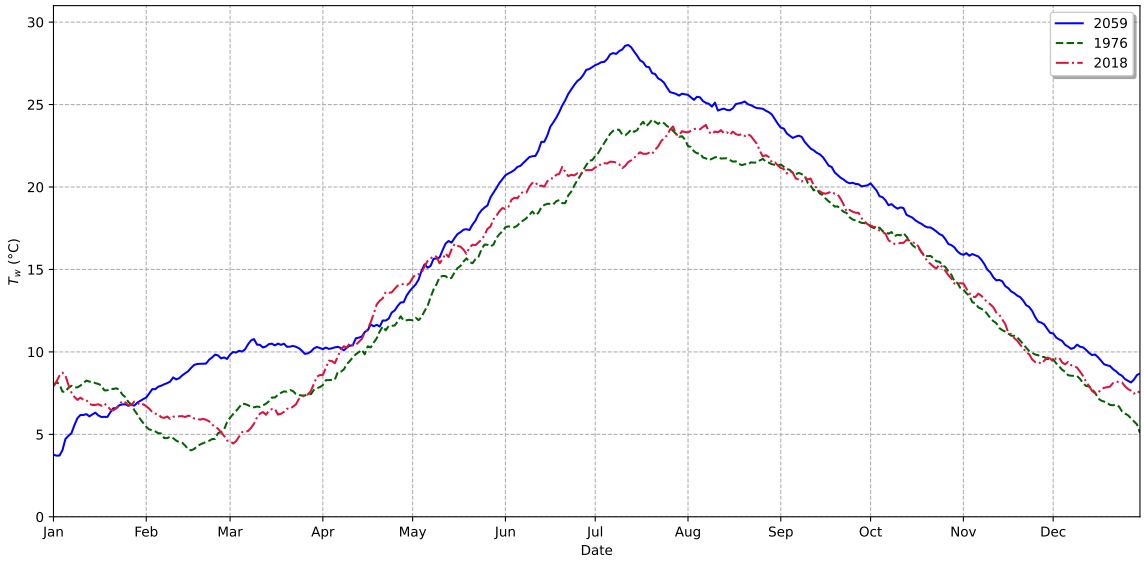

Figure 5.10: Plot of modelled water temperatures for the Zeeschelde at the Lillo measuring post during the worst-case year 2059 and comparison with historically extreme years 1976 and 2018.

Higher temperatures are reached during the worst-case year than during the historically extreme years. In 2059, we find a peak T_w of **28.61 °C**. The highest water temperature during 1976 is, according to the model, 24.09 °C.

5.4 Wildfire Hazard

Figure 5.11 shows the daily precipitation totals P for the worst-case year 2059. The total rainfall at Uccle during said year amounts to **795.4 mm**. This does not indicate any extreme drought, as the average yearly precipitation total for Uccle (1991-2020) is reported to be 837.1 mm[126]. This is especially true when we compare 2059 to a historically dry year such as 1976, for which we calculated a total rainfall of 574.4 mm in Uccle according to ERA5 data. However, we do find that the summer (JJA) rainfall for the worst-case year 2059 is **125.1 mm**, which is comparable to the 1976 value of 127.1 mm and much lower than the (1991-2020) average summer rainfall for Uccle, which is 234.2 mm[127]. The summer of the worst-case year is therefore comparable to historically extreme years in terms of drought, and more extreme in terms of temperatures. We expect that this will be consequential for fire hazard metrics.

We may focus, for example, on the Natura2000 territory of the Kalmthoutse Heide, which lies at the border between Belgium and the Netherlands, 25 km north of urban Antwerp, and covers about 1000 ha of diverse vegetation[128]. The territory is prone to wildfires during exceptionally dry periods.

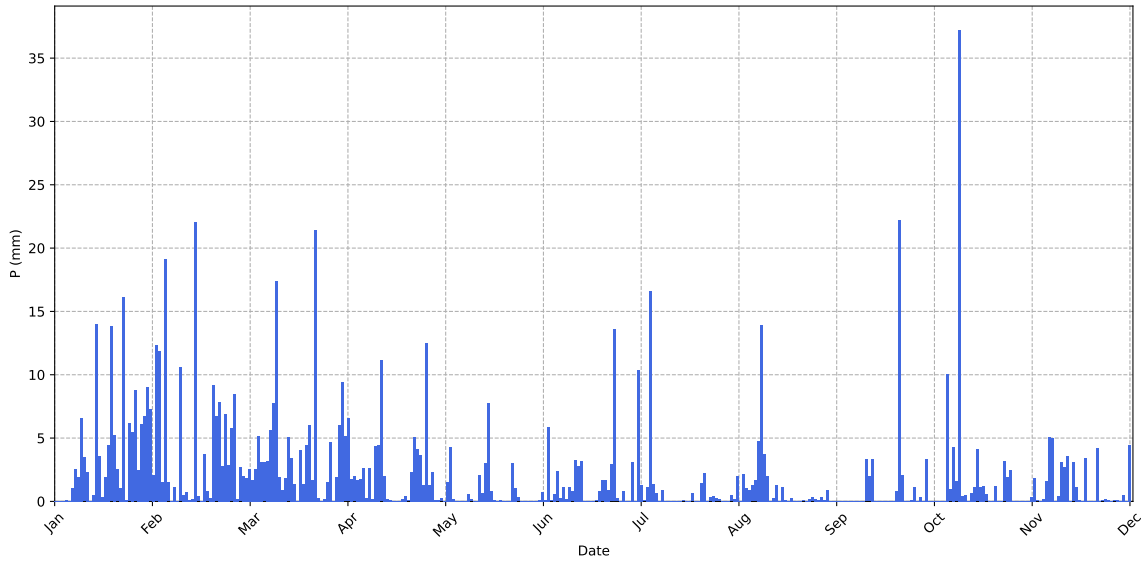

Figure 5.11: Plot of daily precipitation values at Uccle for the worst-case year 2059.

Relatively large fires took place in 1976, 1996, and most recently in 2011. These fires destroyed 120 ha, 330 ha, and 370 ha of the core area respectively[128, 129].The evolution of the FWI, introduced in section 3.4.4, is shown in figure 5.12 for the Kalmthoutse Heide during the worst-case year 2059, as well as during 1976. Calculations for 1976 are again performed using ERA5 data.

Figure 5.12 also displays the different danger classes used to interpret fire hazard from FWI results. The Copernicus Emergency Management Service (CEMS) uses the following danger class definitions for Europe[130]:

- Very Low : FWI < 5.2
- Low : $5.2 \leq$ FWI < 11.2
- Moderate : $11.2 \leq$ FWI < 21.3
- High : $21.3 \leq$ FWI < 38.0
- Very High : $38.0 \leq$ FWI < 50.0
- Extreme : FWI ≥ 50

From figure 5.12, it is clear that the worst-case year exhibits much more frequent and more severe fire hazards than a historically extreme year like 1976. The worst-case year FWI peaks at **72.5** - which is well into the extreme danger class - on the 13th of June. On this day, meteorological conditions are favourable for wildfires in large parts of the country, as can be seen in figure 5.13. For 1976, we calculate a peak FWI of 49.9 at Kalmthout.

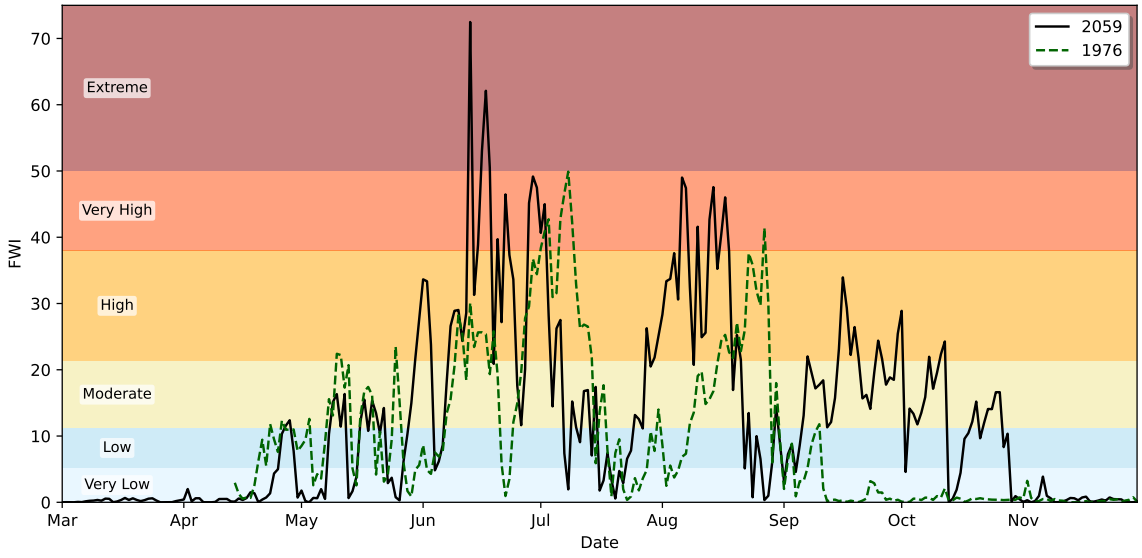

Figure 5.12: Plot of daily FWI values for Kalmthoutse Heide during fire hazard monitoring for the worst-case year 2059 and the historically extreme year 1976. Background colours indicate FWI danger classes.

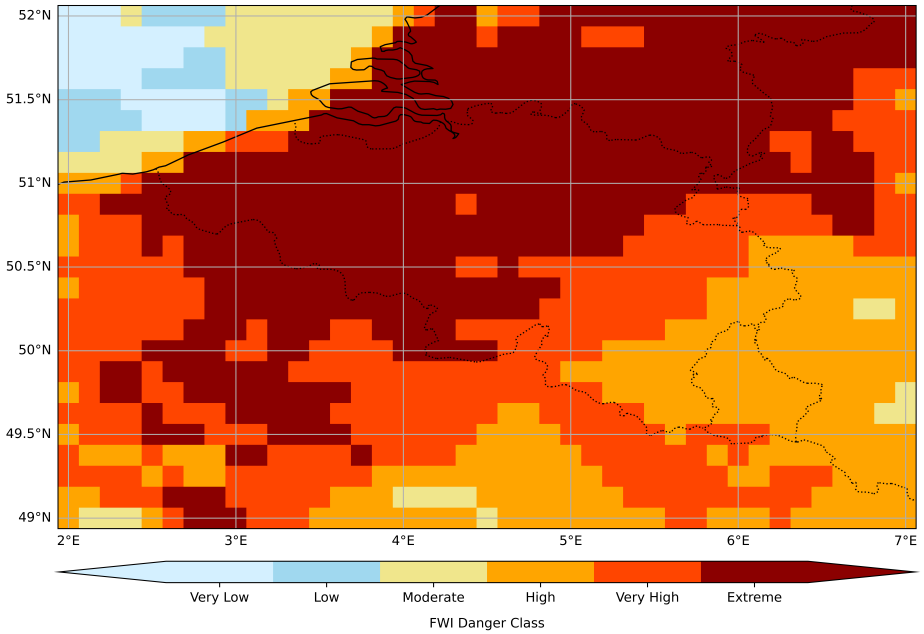

Figure 5.13: Map of wildfire danger in Belgium on the most hazardous day of the worst-case year 2059.

5.5 Invasive Insect Species

Following the approach described in section 3.4.5, we calculate the number of generations that can grow in a year for populations of three invasive insect species: the brown marmorated stink bug (*Halyomorpha halys*), the Japanese beetle (*Popillia japonica*) and the false codling moth (*Thaumatotibia leucotreta*). The resulting voltinism maps for Belgium are shown in figure 5.15, both for the historically extreme year 1976 and the chosen worst-case year 2059. Calculations for 1976 are based on temperature data from ERA5. The plots show how favourable temperature conditions *would be* for the studied potential populations if the corresponding species were present in Belgium. We reiterate that the marmorated stink bug has been observed in Belgium as early as 2011, but as of 2025 the remaining two species are not known to be present. In presenting the results, we refrain from rounding generation counts to integer numbers to more clearly show any potential spatial patterns. A decimal number of generations means that most populations produce the closest integer number of generations, but some populations might differ[131].

From figure 5.15, we clearly note an increased number of generations during the worst-case year for all considered species. We may also evaluate voltinism for these species at a specific location of interest. The Sint-Truiden Fruit Valley is located at the center of the Haspengouwen region, which is known as an active region for fruit cultivation. An overview of the calculated generation counts for the three species, evaluated at the Fruit Valley, is shown in figure 5.14, for the worst-case year 2059 along with a comparison to 1976.

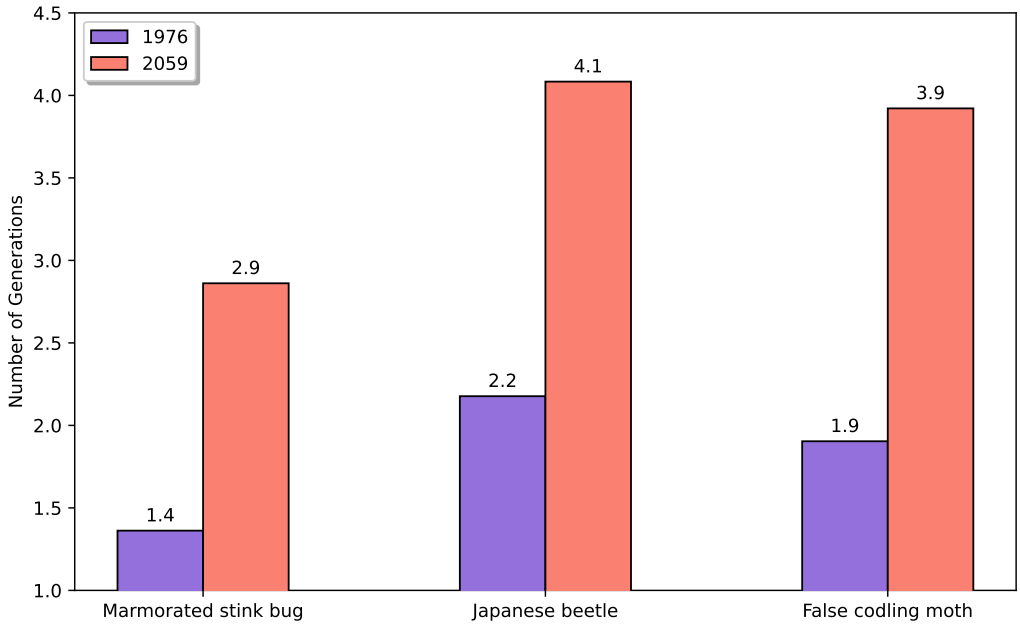

Figure 5.14: Comparative overview of the calculated voltinism of the brown marmorated stink bug (*Halyomorpha halys*), the Japanese beetle (*Popillia japonica*) and the false codling moth (*Thaumatotibia leucotreta*), evaluated at the Sint-Truiden Fruit Valley.

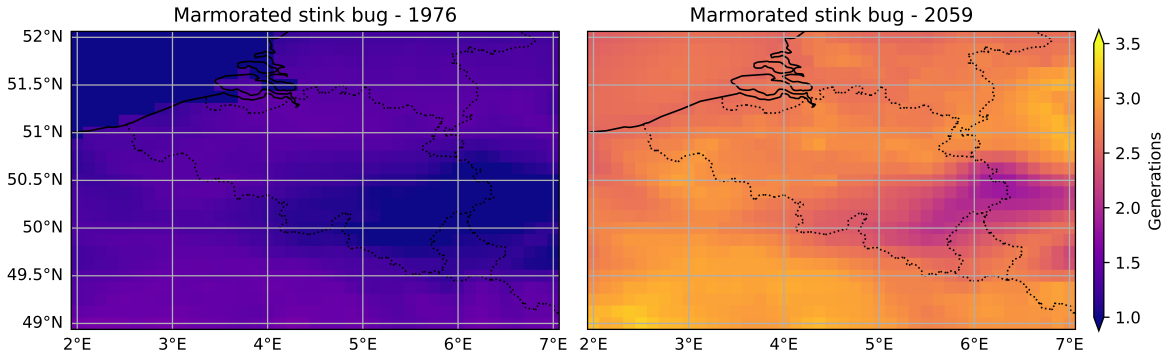

(a)

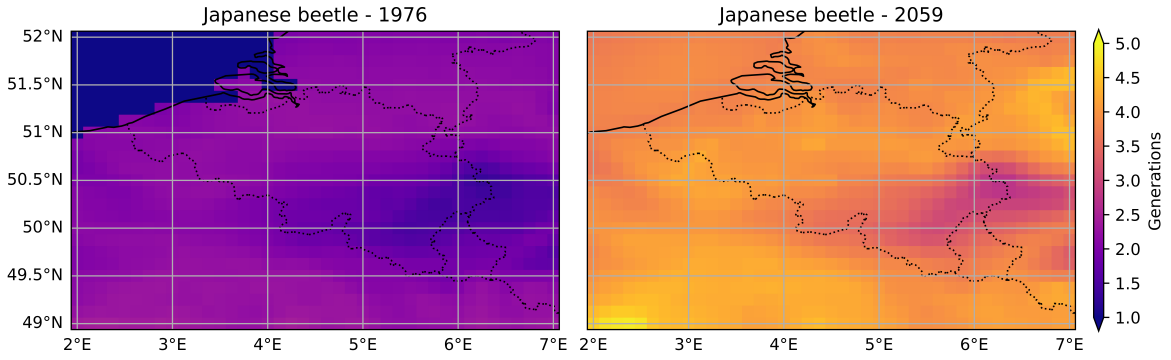

(b)

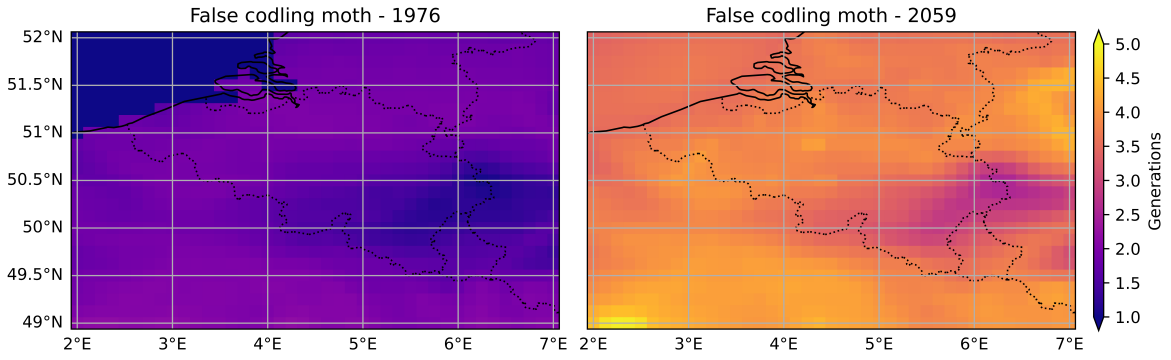

(c)

Figure 5.15: Comparative maps showing the calculated voltinism for 1976 (left) and the worst-case year 2059 (right) of three invasive species under study: the brown marmorated stink bug (*Halyomorpha halys*) (a), the Japanese beetle (*Popillia japonica*) (b) and the false codling moth (*Thaumatotibia leucotreta*) (c).

5.6 Air Quality

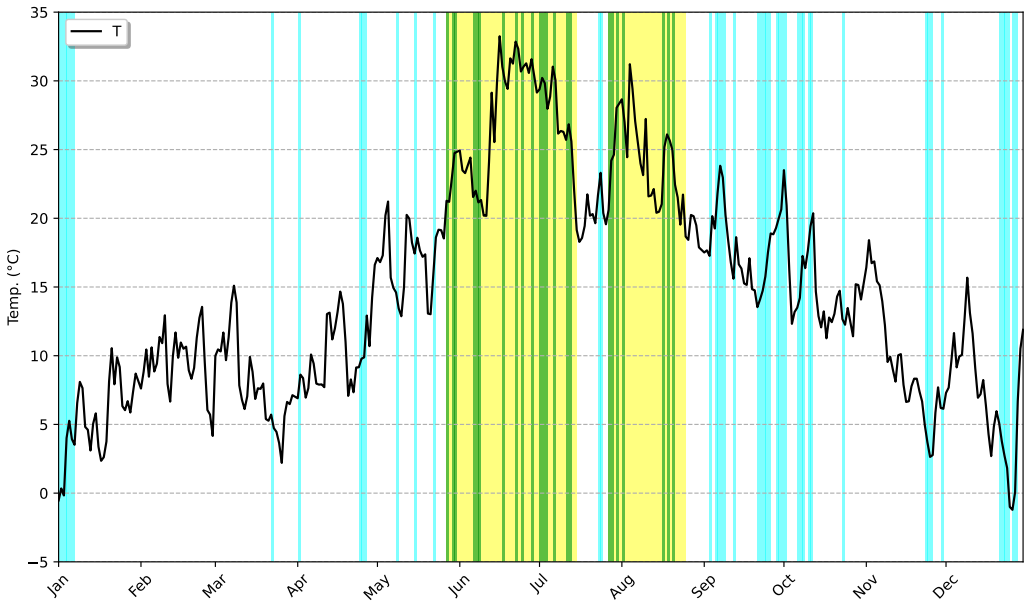

Figure 5.16: Plot displaying daily average temperatures T as well as stagnation conditions for the worst-case year 2059, evaluated for Uccle. The shaded yellow areas correspond to heatwaves according to the RMI definition. Shaded blue areas correspond to H-ASI stagnant days that do not coincide with heatwave days, while shaded green areas mark days that are simultaneously a heatwave day and an H-ASI stagnant day.

Stagnant days, which generally correspond to air pollution peaks, are identified for the worst-case year 2059 using the H-ASI definition formulated in section 3.4.6. The results for the Uccle grid point are shown in figure 5.16. We find a total of **70 stagnant days** across the entire year. This result is in line with the study by Van Nieuwenhuyse et al. (2023), in which it is reported that for Belgium, on average, roughly 20% of days are H-ASI stagnant, based on both ERA5 and CORDEX analyses[112]. Our results for the worst-case year also contain **23 stagnant heatwave days**, during which pollution and negative health effects would likely be exacerbated.

5.7 Energy Consumption for Heating and Cooling

Conditioning type	WCY load (kWh)	RPY load (kWh)	Difference (kWh)	Fractional difference (%)
Heating	7608	11804	4196	-36
Cooling	5023	3006	2017	+67

Table 5.3: Table listing annual heating and cooling loads for the simulated medium-sized, single-story office building in Brussels during the worst-case GWL2.0 year (WCY) and the representative late 20th century year (RPY).

Monthly heating and cooling loads for the simulated building described in section 3.4.7 are shown in figure 5.17, both during the worst-case year 2059 as well as during the representative late 20th century year. Monthly dry-bulb temperatures are plotted as well. Annual heating and cooling loads for both years are listed in table 5.3, along with absolute and fractional changes in energy demand.

We see that the cooling load is 67% higher during the worst-case year 2059 than during the late 20th century year, while the heating load is 36% lower. According to these results, however, the reduction in heating loads as a result of warmer temperatures significantly outweighs the increase in cooling loads.

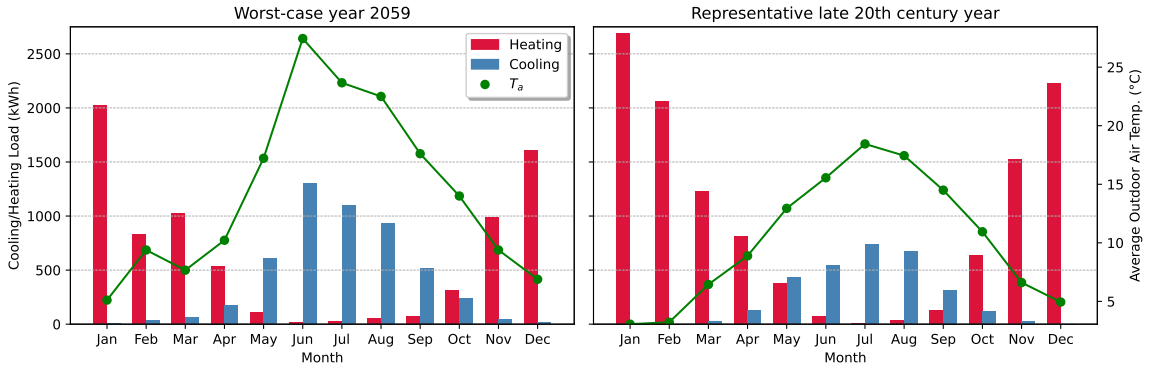

Figure 5.17: Plot of the monthly heating and cooling loads for the simulated medium-sized, single-story office building in Brussels during the worst-case GWL2.0 year (left) and the representative late 20th century year (right).

5.8 Circulation Patterns

In this final section we review the physical consistency of the mined event by looking at circulation patterns. A plot of *Sea Level Pressure* (SLP) and temperature at 850 hPa (T_{850}) is shown in figure 5.18 for the hottest day of the worst-case year 2059, which is the 16th of June.

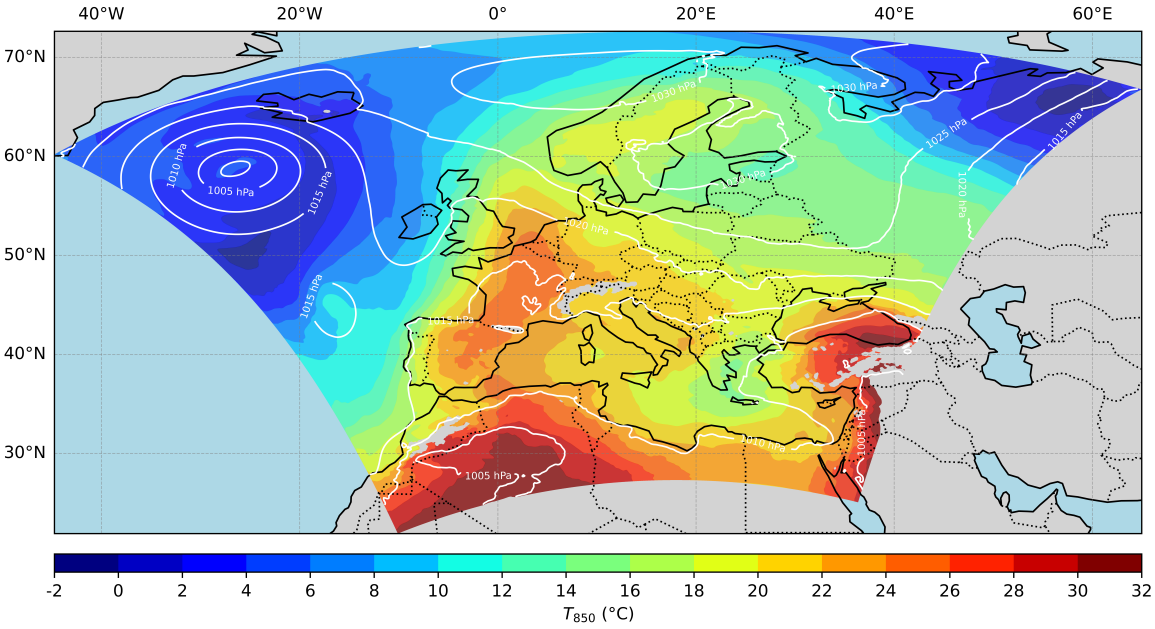

Figure 5.18: Map of SLP (white contours) and T_{850} (shaded contours) for the hottest day of the worst-case year 2059.

We note a pattern of anticyclonic blocking over the Baltic sea. This blocking persists for several weeks. Such atmospheric conditions are consistent with observed heatwaves in Western Europe[132, 133]. During the first half of June and leading up to the hottest day, we remark a relatively strong cyclone west of the British Isles, as can also be seen in figure 5.18. Such a cyclone is likely responsible for southerly advection, conveying warm air from North Africa into Western Europe[35]. We conclude that circulation patterns during the mined event are in line with what would be expected for a persistent Western-European heatwave.

6 Statistical Evaluation of the Results

In this chapter, we evaluate the GWS results and, more specifically, the selection of the worst-case year using EVT methods. As explained in section 3.5, we make use of the POT approach to model the extreme behaviour of the HI parameter in a GWL2.0 climate. To this end, we must first determine the optimal threshold u_0 using a mean residual life plot and parameter stability plots.

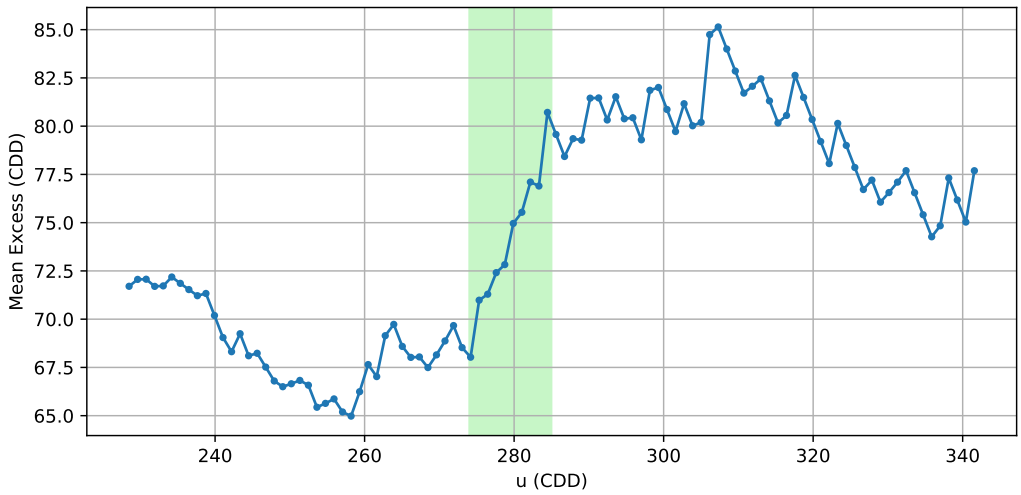

Figure 6.1: Mean residual life plot showing mean excesses as a function of POT threshold choice for the pooled, bias-corrected GWL2.0 EURO-CORDEX runs. The shaded green area corresponds to the identified threshold range for linear behaviour.

The mean residual life plot is shown in figure 6.1. We identify approximate linear behaviour of the mean excesses with respect to the threshold choice u in the range bounded by $u \approx 274$ CDD and $u \approx 285$ CDD. This range thus represents a range of possible optimal thresholds. To make our final choice, we rely on parameter stability plots. These plots are shown in figure 6.2.

From inspection of figure 6.2, we deduce that $\mathbf{u_0 \approx 282}$ **CDD** is a viable threshold. This is equivalent to the **95th percentile** for the pooled, bias-corrected GWL2.0 EURO-CORDEX runs, after rounding to an integer value. We use this threshold to define exceedances to which the GPD model is fitted. The diagnostic plots for checking the fit quality are shown in figure 6.3.

All data points are located on or close to the diagonal line, both in the quantile plot as in the probability plot, indicating that the fit quality is satisfactory. Figure 6.4 shows the plot of the return values and return periods for HI in GWL2.0. For the worst-case year 2059, we find HI = 610.85 CDD, as reported in section 5. According to the statistical calculations performed here, this corresponds to a return period of **719.4 years**, with a 90% confidence interval ranging from 320.5 years to 2137.4 years.

While uncertainties on the estimated return period for the worst-case year 2059 are large, owing to the rare nature of such an event, we conclude that according to analysis of the EURO-CORDEX ensemble, it is a very extreme event in terms of HI even in a GWL2.0 climate. Comparisons can

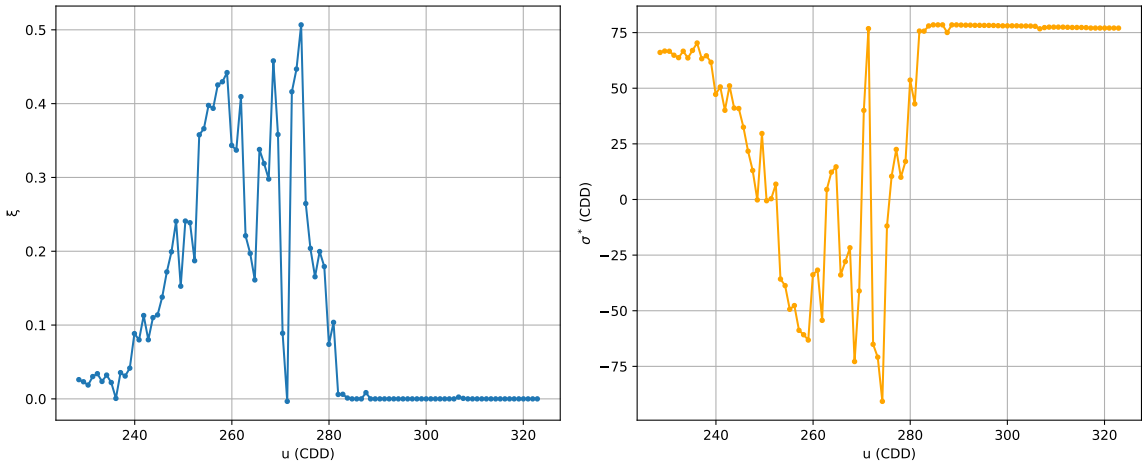

Figure 6.2: Parameter stability plots displaying how the shape parameter ξ (left) and the redefined scale parameter σ^* (right) scale with changing threshold definitions for the GPD model.

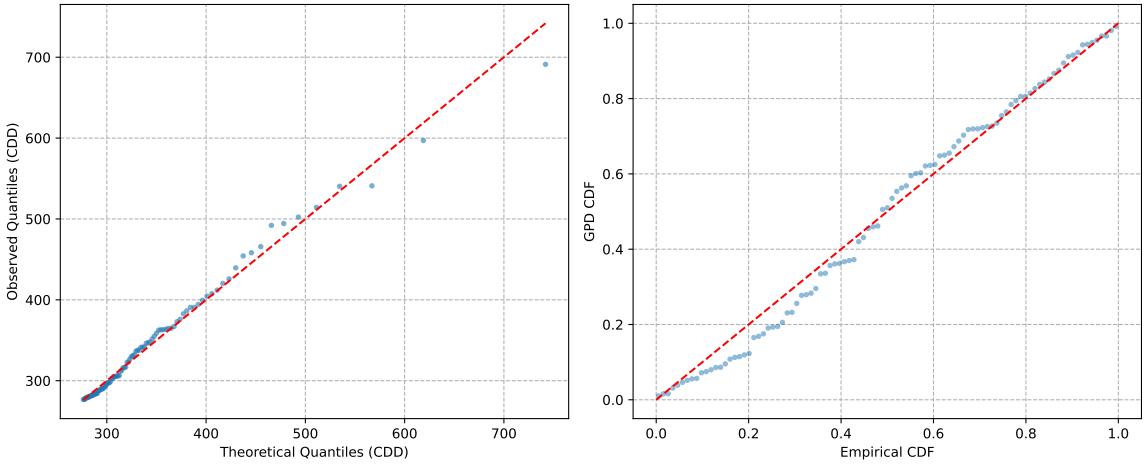

Figure 6.3: Diagnostic plots showing the quality of the GPD fit to the GWL2.0 HI exceedances: a quantile plot (left) and a probability plot (right).

be made with extraordinary heatwaves that have been observed in the past. In the literature, the record-shattering 2021 Pacific Northwest heatwave has been assigned an estimated return period of 1000 years[27, 134], or even much higher than that[135]. According to the statistics presented here, an event like the worst-case year 2059 would likely be of a similar record shattering order for the GWL2.0 climate, like the 2021 event was for the current climate.

One possible cause of the (perhaps too) extreme nature of the GWS event is that we overestimate LGWRs because we work with observational temperature series from one point only. In a recent study by Corre et al. (2025), such a ratio is calculated with data covering all of mainland France, and an LGWR of 1.34 is reported for local and global warming with respect to pre-industrial levels[136]. This is obviously much lower than the LGWRs reported in section 4.1.1 based on the Uccle temperature series. Furthermore, the GWS thresholds themselves already represent extremes, and we mine events from the ensemble that exceed said thresholds, necessarily making them even more extreme.

However, as we briefly mentioned in section 1.1, it is currently still difficult to capture trends in

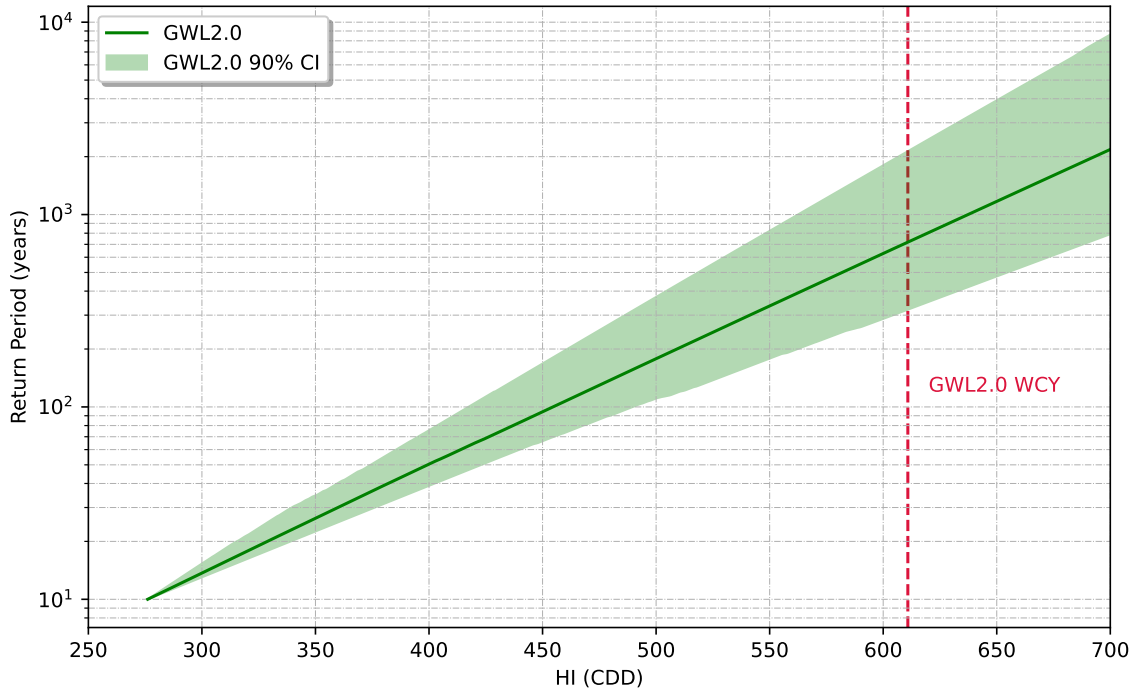

Figure 6.4: Plot of return values and return periods for HI as determined from the pooled, bias-corrected GWL2.0 EURO-CORDEX runs. The value associated with the worst-case year 2059 (610.85 CDD) is marked by a dashed red line.

temperature extremes using climate models. Recent studies have reported that these models often underestimate the frequency and intensity of extreme heat events, particularly in Western and Central Europe. One significant factor contributing to this underestimation is the models' inadequate representation of atmospheric circulation changes[13]. For instance, an increase in southerly airflows over Western Europe has been linked to a substantial portion of the observed warming trends, a phenomenon not fully captured by current models. Additionally, many models fail to account for the reduction in aerosol concentrations over recent decades, which has led to increased solar radiation and subsequent warming - a process known as *brightening*[137]. Furthermore, the misrepresentation of historical temperature variability and distribution in models can lead to significant underestimations of future heat extremes, as observation-constrained model studies have shown[138]. This is indeed the motivation for the development of a GWS framework; we circumvent model shortcomings by using observations and the delta-change method to determine threshold values. As this statistical analysis is based on (bias-corrected) model projections for GWL2.0, we may interpret the high return period of the chosen year to partially be the result of this discrepancy between observations and model simulations. The fact remains that the GWS results, and especially the chosen worst-case year, represent an upper limit to the severity of GWL2.0 heat extremes, owing to the threshold-based nature of the methodology.

7 Discussion

7.1 Performance, Open Challenges and Future Research

In this section, we review the performance and some shortcomings of the ensemble-mining framework and the impact analysis presented in this thesis, and we formulate possible avenues of future research.

The GWS method is developed with the aim of efficiently mining plausible years of extreme heat in a given climate from large simulation ensembles. It was applied in this project to mine such years from EURO-CORDEX projections in a Belgian GWL2.0 climate. An analysis of a chosen mined extreme year in terms of impact and statistical properties shows that the method appears suitable for obtaining very extreme, record-shattering events in a given climate. The method also has some shortcomings which must be adressed. A major component of the method is the translation of global to local warming using observational series. However, the procedure for this, as performed in this thesis work, is perhaps not sufficiently robust. Localised observations may be influenced by many factors, and varying the range over which the LGWR is determined leads to slightly different results. When propagated into the rest of the methodology, these variations may become significant. A potential way to eliminate such worries is to combine observations from a set of local weather stations that cover the area of interest. A study of the uncertainties introduced by LGWR calculations would also be beneficial. The statistical analysis of the extreme year in chapter 6 indeed suggests that the calculated LGWRs may be too high.

Secondly, the GWS thresholds are based on observational series as well, and as such they are extremely sensitive to outliers in these series. For example; the year 1947 is a record extreme year in terms of HI, so that when this year is not included in determining the GWS thresholds, we come up with less extreme GWL2.0 heatwave characteristics. Furthermore, if T_{max} would not be included as a relevant climate index, the worst-case year 2059 discussed in chapter 5 would actually qualify as a GWL2.5 year based on remaining thresholds. It would clearly be very valuable to investigate the sensitivity of GWS to choices for the climate indices and the included data ranges. This inherent weakness of GWS can be avoided by following a completely different approach. One could apply an EVT analysis, like the one in chapter 6 to the delta-changed observational time series for several indices (HI, $T_{max}, \dots$). One could then select return values of said indices corresponding to a chosen return period. These return values are then our new thresholds. After selecting or shifting simulation projections following the procedures outlined in section 3.3, we may mine years from the ensemble using these thresholds. Additional research would be required to assess the viability of this approach, and to compare its results with those of GWS.

An inherent downside to the GWS methodology as it is presented in section 3.2.1 is that the detrending step does not take into account changes in climate variability, as the temporal structure of the observed series is preserved[139]. The fact that climate variability is preserved in the delta-change transformation of the observational series is somewhat unattractive. It would be interesting to see if results vary when the detrending is combined with extreme-value statistics to account for this limitation.

As explained in chapter 6, the years mined from the ensemble through GWS may always be extraordinarily extreme. In this case, we may use GWS to answer the question: *What is the worst possible heat extreme we may encounter in a given climate?* The selection of a worst-case year, however, does not seem to yield extremes that are *typical*[1] for said climate. One might argue that this is in contrast to the plausibility-based nature of the storyline approach. It would be interesting to investigate an alternative to the extreme event identification step in the full GWS approach. Instead of selecting years which cross the thresholds, we may select years for which the climate indices or parameters have values close to these thresholds, which we may in turn regard as extreme event reference values.

The EURO-CORDEX ensemble used in this thesis was sourced from CMIP5 RCP8.5 runs. However, in recent years, the CMIP5 RCPs have faced scrutiny and it has been considered questionable to regard RCP8.5 as the so-called *business-as-usual* scenario as it would require a dedicated return to coal as an energy source[65]. As explained in section 2.2.3, CMIP6 employs more sophisticated SSP-RCP trajectories yielding more reasonable future scenarios. The study performed in this thesis can be repeated using EURO-CORDEX runs coupled to CMIP6 GCMs, and the results may be compared.

Methods like GWS are difficult to validate, because the results cannot be compared to observed events. One could potentially combine several storyline-oriented techniques, such as SWGs or PGW[2], and check whether the obtained results are comparable to GWS results. Another option is to perform the full GWS analysis for extreme events in the current climate, say GWL1.5, and check if the method can reproduce characteristics of recently observed heatwaves.

Finally, the impact analysis performed in this thesis was done using basic and simple local impact models. A more thorough impact analysis would ideally be a coordinated effort of several Belgian climate research groups, guided by the needs expressed by relevant stakeholders during, for example, stakeholder meetings of the kind introduced in section 1.3.3.

7.2 Summary

In this thesis, we propose an ensemble-mining approach based on *Global Warming Scaling* (GWS) to construct plausible future heatwave storylines for Belgium, focusing on a GWL2.0 scenario. The storyline framework is presented as an alternative to probabilistic climate modelling (MoCoDoT), aiming instead for physically consistent, locally relevant representations of extreme weather with concrete societal applications.

The threshold-based identification of extreme heat years in ensemble simulations makes use of observed historical data and a modified delta-change method. This approach avoids some of the complexity and computational cost of more traditional bias correction methods or alternatives like ensemble boosting. However, the method inherently preserves historical variability and does not account for changes in variability or extremeness in the future, which is a limitation.

Simulation runs are selected from the large ensemble, consisting of EURO-CORDEX RCP8.5 runs and a smaller set of statistically-dynamically downscaled runs over the Brussels region, based on how well they reproduce observed distributions for TX, TN and HI. Selected runs are assumed to produce plausible extremes in a future climate. The selection procedure is complemented with a

[1] Of course, an extreme event is atypical per definition. We may regard typical extremes as events that are relatively likely to occur in a given climate, but are still outliers relative to the climate baseline.

[2] See section 1.3.2.

shifting procedure, where projections from discarded EURO-CORDEX runs are shifted along the time axis until they match the statistics of historical observations. Combined results yield a total of 47 mineable simulation runs. Extreme-heat years are identified in these projections using GWS thresholds for HI and T_{max} for GWL2.0, resulting in 40 potential events. GWS thresholds for tropical night count and length of the longest heatwave are employed to select a worst-case year from this set. We select the year 2059 from the RCM HadREM3-GA7-05 v1 (EUR-11) coupled to the GCM MOHC-HadGEM2-ES (r1i1p1).

Preliminary modelling for the worst-case year (2059) shows important plausible impacts: increased WBGT values and associated lost working hours due to heat stress, elevated Zeeschelde water temperatures near energy plants (with possible implications for cooling efficiency), and enhanced wildfire risks. We also note a potential increase in voltinism of invasive insect species, atmospheric conditions that may negatively impact air quality and changes in heating and cooling demands. A study of synoptic conditions shows that the mined event is consistent with characteristic atmospheric conditions during observed Western-European heatwaves. Such storyline-oriented investigations can be important to stakeholders and policy-making individuals.

A detailed statistical analysis of the chosen worst-case GWL2.0 year in terms of HI, regarded as the dominant climate index, based on a full bias-corrected EURO-CORDEX ensemble for GWL2.0, shows that said year is extraordinarily extreme, even in the warmer climate conditions. We calculate a return period of 719.4 years, but the 90% confidence interval reaches up to 2137.4 years. Such return periods are comparable to the record-shattering 2021 North American heatwave with respect to current climate conditions. We conclude from this that the event selection procedure of the GWS framework may be biased to produce such extraordinarily rare events. We also note, however, that climate models, in their current capacity, tend to be too conservative when it comes to capturing heat extremes. We point to further research for an in-depth study of the shortcomings of both observation-based an model-based approaches for local assessment, and the discrepancies between them.

Further open challenges remain. The GWS method needs refinement to better reflect future variability and compounding extremes. Sensitivity to methodological choices needs to be investigated thoroughly. Furthermore, impact modelling (especially health-related and socio-economic) would benefit from stakeholder input to guide the choice of metrics and thresholds. Finally, better integration of these physical storylines into risk communication frameworks is necessary for them to meaningfully inform policy.

A Nederlandstalige Samenvatting

Hitte-extremen zijn moeilijk te onderzoeken door hun zeldzaamheid. Hoewel observaties en klimaatsimulaties essentiële inzichten bieden in toekomstige klimaatextremen, resoneren ruwe statistieken alleen vaak niet met het bredere publiek. *Verhaallijnen* of *toekomstige-weersverhalen* kunnen de kloof overbruggen tussen abstracte wetenschap en door mensen beleefde extreme weersomstandigheden, waardoor klimaatverandering tastbaar, herkenbaar en concreet wordt. Zulke verhaallijnen werpen licht op vragen als: *Hoe erg zouden de 2024 Balkanhittegolven geweest zijn in een warmer klimaat?* of *Waren ze mogelijk in een pre-industrieel klimaat?* In dit project onderzoeken we een data-mining methode om extreme-hitteverhaallijnen te construeren in een contrafeitelijk Belgisch klimaat. De methode, genaamd Global Warming Scaling (GWS), wordt gebruikt om extreme-hittedrempels in een contrafeitelijk klimaat te bepalen d.m.v. observationele data en extreme-hittesituaties worden geïdentificeerd in standaard EURO-CORDEX simulaties en in simulaties gekalibreerd naar een hogere resolutie met resolvering van stedelijke effecten.

De identificatie van extreme-hittejaren gebeurt op basis van drempelwaarden die worden afgeleid uit observationele temperatuursreeksen van dagelijkse metingen te Ukkel, gecombineerd met een aangepaste biascorrigerende delta-change methode. Deze aanpak vermijdt de complexiteit en rekenlast van traditionele rigoureuze en spatiale bias-correctie of alternatieven zoals ensemble boosting. Een belangrijke beperking is wel dat de historische variabiliteit behouden blijft, waardoor veranderingen in toekomstige variabiliteit of extremiteit niet worden meegenomen in de analyse.

Uit het volledige ensemble wordt een set simulatieruns geselecteerd op basis van de mate waarin deze runs de verdelingen van dagelijkse maximumtemperatuur (TX), minimumtemperatuur (TN) en jaarlijkse hitte-intensiteit (HI) uit de waarnemingen correct weergeven. We nemen dan aan dat geselecteerde runs plausibele extremen genereren in een toekomstig Belgisch klimaat. Om waardevolle informatie uit de niet-geselecteerde runs toch te benutten, wordt een aanvullende shifting-procedure toegepast waarin projecties in hun geheel langs de tijdsas verschoven worden tot ze statistisch overeenkomen met historische observaties. Samen levert dit 47 bruikbare simulatieruns op. In deze projecties worden extreme hittejaren geïdentificeerd aan de hand van GWS-drempelwaarden voor HI en T_{max} voor een GWL2.0 klimaat, wat 40 potentiële jaren oplevert. Door bijkomende drempels toe te passen voor het aantal tropische nachten en de duur van de langste hittegolf wordt een *worst-case* jaar geselecteerd. Dit blijkt het jaar 2059 te zijn, afkomstig uit de HadREM3-GA7-05 v1 (EUR-11) RCM gekoppeld aan de MOHC-HadGEM2-ES GCM (r1i1p1).

Voor dit *worst-case* jaar wordt een beperkte impactanalyse uitgevoerd. We modelleren hittestress aan de hand van de *Wet Bulb Globe Temperature* (WBGT) index, die we berekenenen via de gekende methode van Liljegren. Verhoogde hittestress wordt vertaald naar productiviteitsverlies en verloren werkuren. Voor het gekozen jaar 2059 leidt de langdurige hitte tot significante productiviteitsverliezen over heel België. Ook stellen we een model op voor watertemperaturen in de Zeeschelde nabij energiecentrales (met mogelijke gevolgen voor koelcapaciteit) als functie van luchttemperatuur, straling en seizoensvariaties. We merken dat de Zeeschelde aanzienlijk opwarmt tijdens het *worst-case* jaar in vergelijking met historische extreme-hittejaren. Tenslotte modelleren we bosbrandgevaar op basis van de Canadese *Fire Weather Index* (FWI) en vinden we een sterk verhoogd risico op bosbranden in grote delen van het land tijdens de periodes van langdurige hitte en de droge zomermaanden. We vonden ook een potentiële toename in het jaarlijkse aantal generaties

van invasieve insectensoorten, atmosferische condities die gepaard kunnen gaan met achteruitgaande luchtkwaliteit en veranderingen in het energieverbruik voor koeling en verwarming van gebouwen. Als controle op de fysische consistentie van het gemijnde jaar onderzoeken we ook de gesimuleerde synoptische condities en vergelijken we deze met de condities die geobserveerde hittegolven in West-Europa kenmerken. Dergelijke verhaallijn-gebaseerde analyses kunnen bijzonder waardevol zijn voor beleidsmakers en belanghebbenden.

Een gedetailleerde statistische analyse door middel van extreme-waardenstatistiek van het gekozen *worst-case* jaar, op basis van HI als dominante klimaatsindicator en gebruikmakend van een volledig bias-gecorrigeerd EURO-CORDEX ensemble voor GWL2.0, toont aan dat dit jaar uitzonderlijk extreem is, zelfs voor deze warmere klimaatcondities. We berekenen een terugkeerperiode van 719,4 jaar, met een 90%-betrouwbaarheidsinterval dat oploopt tot 2137,4 jaar. Dergelijke terugkeerperiodes zijn vergelijkbaar met de recordbrekende hittegolf van 2021 in Noord-Amerika ten opzichte van het huidige klimaat. Hieruit concluderen we dat de methode voor de selectie van extremen binnen het GWS-raamwerk mogelijk een bias bevat die leidt tot de selectie van uitzonderlijk zeldzame gebeurtenissen. We bemerken echter ook dat klimaatmodellen, in hun huidige capaciteit, doorgaans te conservatief zijn in het inschatten van hitte-extremen. We verwijzen naar verder onderzoek voor een diepgaande studie van de tekortkomingen van zowel op observatie gebaseerde als modelgebaseerde methodes voor verhaallijnstudies op lokaal niveau, en de verschillen tussen beide.

Er zijn ook verdere open vragen en tekortkomingen. GWS kan verfijnd worden om ook toekomstige variabiliteit in rekening te brengen. Ook de gevoeligheid van de resultaten voor methodologische keuzes verdient verdere studie. Het kan nuttig zijn om stakeholders te betrekken bij de impactmodellering, en om hun inbreng in acht te nemen bij het maken van methodologische keuzes. Een betere integratie van deze fysisch onderbouwde storylines in bestaande kaders voor risicocommunicatie is essentieel om ze daadwerkelijk beleidsrelevant te maken.

B Extreme Value Theory

In this appendix we review the relevant aspects of *Extreme Value Theory* (EVT) as it is used in this thesis. To this end, we mainly follow the work of Coles (2013), which contains more details for the interested reader[71]. Though only the Generalised Pareto Distribution is used in this thesis, we include a description of the Generalised Extreme Value Distribution as well.

B.1 Generalised Extreme Value Distribution

Let $X_1, X_2, \ldots$ denote a sequence of independent random variables sharing a commong distribution function F. We denote the maximum of n of these variables as $M_n = \max(X_1, \ldots X_n)$. Theoretically speaking, the distribution of n can be derived exactly for all n. Let z be some reference value, then:

$$\begin{aligned} P(M_n \leq z) &= P(X_1 \leq z, \ldots, X_n \leq z) \\ &= P(X_1 \leq z) \times \cdots \times P(X_n \leq z) \\ &= [F(z)]^n \end{aligned} \tag{B.1}$$

In practice, however, the distribution function F is unknown. One could resort to standard statistical methods for estimating F, and plug the result into the right hand side of equation B.1, but F^n may be very sensitive to small discrepancies in the estimation of F itself. The basis of EVT is to accept that F is unknown, and to search for approximations of F^n that can be estimated using only extreme data.

We essentially want to work towards an extreme value analog of the central limit theorem. We therefore proceed by letting $n \to \infty$. This alone turns out to be insufficient. Let z_+ be the smallest value such that $F(z) = 1$, then $F^n(z) \to 0$ as $n \to \infty$ for any $z < z_+$. We solve this issue by renormalising M_n:

$$M_n^* = \frac{M_n - b_n}{a_n} \tag{B.2}$$

with $\{a_n > 0\}$, $\{b_n\}$ sequences of constants that stabilise the distribution of M_n^* as n increases. The range of possible limit distributions for M_n^* is given by the *extremal types theorem*, which is omitted here for brevity. Instead, we immediately reformulate the theorem using the *Generalised Extreme Value* (GEV) distribution. The full reasoning and a sketch of the proof can be found in Coles (2013)[71].

Theorem B.1.1. *If there exist sequences of constants* $\{a_n > 0\}$, $\{b_n\}$ *such that:*

$$P\left(\frac{M_n - b_n}{a_n} \leq z\right) \to G(z) \;\; as \;\; n \to \infty \tag{B.3}$$

for a non-degenerate distribution function G, then G is a member of the family of so-called GEV distribution functions:

$$G(z) = \exp\left\{-\left[1+\xi\left(\frac{z-\mu}{\sigma}\right)\right]^{-1/\xi}\right\} \tag{B.4}$$

defined on $\{z : 1+\xi(z-\mu)/\sigma > 0\}$, *where* $-\infty < \mu < \infty$, $\sigma > 0$ *and* $-\infty < \xi < \infty$.

Now, if for large n, renormalised maxima can be approximated using a GEV function, then the same holds for the original maxima. Indeed, suppose that $P(M_n^* \leq z) \approx G(z)$, with M_n^* as defined in equation B.2. Now redefine z as $a_n z + b_n$, so that:

$$P(M_n \leq z) \approx G\left(\frac{z-b_n}{a_n}\right) \tag{B.5}$$

The distribution on the right hand side will still be a GEV distribution.

For a sequence of independent observations $X_1, X_2, \ldots$, the extreme values can be modelled using the Generalized Extreme Value (GEV) distribution. The series is divided into blocks of size n, with the maximum from each block extracted, resulting in a new series of *block maxima* $M_{n,1}, M_{n,2}, \ldots$ A GEV distribution is fitted to these block maxima. Equation B.4 can be inverted to obtain estimates of extreme quantiles of the block maxima distribution:

$$z_p = \begin{cases} \mu - \frac{\sigma}{\xi}\left[1-\{-\log(1-p)\}^{-\xi}\right], & \xi \neq 0, \\ \mu - \sigma\log\{-\log(1-p)\}, & \xi = 0. \end{cases} \tag{B.6}$$

where $G(z_p) = 1-p$. z_p is commonly referred to as the *return level* associated with *return period* $1/p$. The terminology reflects the fact that, to a reasonable degree of accuracy, z_p is expected to be exceeded on average once every $1/p$ blocks.

The classical EVT approach as described here applies to series of independent random variables, but can be generalised to stationary series as well[140].

B.2 Generalised Pareto Distribution

The modelling of only block maxima can be a wasteful way to investigate extremes, as potentially valuable extremes are discarded in favour of the block maxima. The *Peaks-Over-Threshold* (POT) method represents an alternative approach.

We again look at the series of identically distributed variables $X_1, X_2, \ldots$ The distribution function is denoted F. We now regard extreme events as those X_i that exceed a high threshold u. By Bayes' theorem, the behaviour of extremes for all X_i in the sequence can be described via:

$$P(X_i > u+y | X_i > u) = \frac{1-F(u+y)}{1-F(u)} \tag{B.7}$$

with $y > 0$. If F is known, then the distribution of threshold exceedances is also known. In practice, this is not the case. A family of approximations known as the *Generalised Pareto Distribution* (GPD) functions becomes applicable. A proof of the accompanying theorem can be found in Coles (2013)[71].

Theorem B.2.1. *We once again denote $M_n = \max(X_1, \ldots, X_n)$. Assume that the distribution function F satisfies theorem B.1.1, meaning that for large n we have:*

$$P(M_n \leq z) \approx G(z) \tag{B.8}$$

with G a GEV function with parameters μ, σ and ξ. Then, for sufficiently large u, the distribution of $X_i - u$ conditioned on $X_i > u$, for any X_i in the sequence, is approximated by the GPD family:

$$H(y) = 1 - \left(1 + \frac{\xi y}{\tilde{\sigma}}\right)^{-1/\xi} \tag{B.9}$$

defined on $\{y : y > 0 \wedge (1 + \xi y/\tilde{\sigma}) > 0\}$, with $\tilde{\sigma} = \sigma + \xi(u - \mu)$.

Theorem B.2.1 implies that, if block maxima have approximating distribution G, then threshold excesses have a corresponding approximate distribution within the GPD family. The parameters of the GPD describing threshold excesses are uniquely determined by those of the associated GEV distribution describing the block maxima.

The choice of the threshold u represents a bias-variance trade-off and can, in practice, be done using both mean residual life plots and parameter stability plots[141]. In a mean residual life plot, we plot mean excesses as a function of the threshold choice. The region in which the relationship is approximately linear represents a suitable range of potential threshold choices. We complement this result with parameter stability plots. This means that we fit a GPD model at different thresholds and look for the lowest threshold u_0 that gives a good approximation. For u exceeding the value for which a good approximation is obtained, the estimated shape parameter ξ remains constant, while the estimated Pareto scale parameter $\tilde{\sigma}$ is approximately linearly in u. A more convenient choice for the scale parameter is the redefined version $\sigma^* = \tilde{\sigma} - \xi u$, so that we have to identify constant behaviour for the σ^* estimate instead of linear behaviour for the $\tilde{\sigma}$ estimate.

Suppose now that the threshold (u) exceedances of variable X are suitably described by a GPD with scale parameters σ and shape parameter ξ. For $x > u$, this means, with $\xi \neq 0$:

$$P(X > x | X > u) = \left[1 + \xi\left(\frac{x - \mu}{\sigma}\right)\right]^{-1/\xi} \tag{B.10}$$

from which:

$$P(X > x) = \zeta_u \left[1 + \xi\left(\frac{x - \mu}{\sigma}\right)\right]^{-1/\xi} \tag{B.11}$$

with $\zeta_u = P(X > u)$. Therefore, the *m-observation return level* x_m is a solution of:

$$\frac{1}{m} = \zeta_u \left[1 + \xi\left(\frac{x - \mu}{\sigma}\right)\right]^{-1/\xi} \Leftrightarrow x_m = u + \frac{\sigma}{\xi}\left[(m\zeta_u)^{\xi} - 1\right] \tag{B.12}$$

on the condition that m is large enough to ensure $x_m > u$. If $\xi = 0$, a similar derivation yields:

$$x_m = u + \sigma \log(m\zeta_u) \tag{B.13}$$

Usual N-year return levels can be obtained from the x_m by setting $m = n_y N$, with n_y the number of observations per year. We find:

$$z_N = \begin{cases} u + \frac{\sigma}{\xi}\left[(N n_y \zeta_u)^{\xi} - 1\right], & \xi \neq 0, \\ u + \sigma \log(N n_y \zeta_u), & \xi = 0. \end{cases} \tag{B.14}$$

The parameters of the GPD can be most accurately obtained using maximum-likelihood estimation[142].

C Liljegren's Method

Liljegren's method for modelling WBGT is introduced in section 3.4.1. Here, we formulate the method in detail, following the original paper by Liljegren et al. (2008)[88], where more details can be found. The method has been calibrated using WBGT measurements and has been validated to be accurate within 1°C[89]. We require different models for natural wet bulb temperature T_{nwb} and globe temperature T_g.

C.1 Natural Wet Bulb Temperature Model

The natural wet bulb temperature T_{nwb} is defined as the temperature of an air parcel that is cooled to a relative humidity of 100% by evaporation of water into the parcel. In a saturated environment (100% relative humidity), T_{nwb} is equal to the dry bulb temperature T_a, while $T_{nwb} < T_a$ at lower humidity. T_{nwb} is influenced by evaporative cooling, convective heat transfer, and radiative heat exchange, and thus serves as a proxy for these processes. It is measured using a temperature sensor fitted with a wetted wick, which is completely exposed to the environment. The mass balance equation for the wick is given by:

$$\omega(1 - x_w) = k_x A(x_w - x_a), \tag{C.1}$$

where ω is the molar water vapour flux, x_w and x_a are the mole fractions of water vapor at the wick surface and in ambient air, respectively, k_x is the convective mass transfer coefficient, and A is the wick surface area.

According to the ideal gas law, we may write mole fractions as $x = e/P$, with P the barometric pressure, while e refers to the partial pressure of water vapour, which can be obtained from the relative humidity RH and the saturation vapour pressure e_{sat} at a given temperature using Buck's algorithm[143]. We assume saturation near the wick surface so that $e_w = e_{sat}\,(T_{nwb})$ and $e_a = \text{RH} \times e_{sat}\,(T_a)$. We obtain the following expression for the molar water vapour flux:

$$\omega = k_x A \left(\frac{e_{sat}\,(T_{nwb}) - \text{RH} \times e_{sat}\,(T_a)}{P - e_{sat}\,(T_{nwb})} \right) \tag{C.2}$$

The energy balance equation for the wick is:

$$\omega M_{H_2O} \Delta H = hA(T_a - T_{nwb}) + \Delta F_{net}, \tag{C.3}$$

where ΔH is the heat of vaporisation, h is the convective heat transfer coefficient, and ΔF_{net} represents net radiative heat flux. M represents (average) molecular weight. Combining this with equation C.2 and solving for the natural wet bulb temperature yields:

$$T_{nwb} = T_a - \frac{k_x \Delta H M_{H_2O}}{h} \left(\frac{e_{sat}\,(T_{nwb}) - \text{RH} \times e_{sat}\,(T_a)}{P - e_{sat}\,(T_{nwb})} \right) + \frac{\Delta F_{net}}{Ah} \tag{C.4}$$

Using the analogy between heat and mass transfer, k_x/h can be expressed as[144]:

$$\frac{k_x}{h} = \frac{1}{c_p M_{air}} \left(\frac{\text{Pr}}{\text{Sc}} \right)^a. \tag{C.5}$$

where Pr is the Prandtl number for air, Sc is the Schmidt number of water vapour in air, c_p is the specific heat at constant pressure and a is an empirical coefficient. The final equation for T_w is obtained as:

$$T_{nwb} = T_a - \frac{\Delta H}{c_p}\frac{M_{H_2O}}{M_{air}}\left(\frac{\mathrm{Pr}}{\mathrm{Sc}}\right)^a \left(\frac{e_{sat}\left(T_{nwb}\right) - \mathrm{RH} \times e_{sat}\left(T_a\right)}{P - e_{sat}\left(T_{nwb}\right)}\right) + \frac{\Delta F_{net}}{Ah}. \tag{C.6}$$

After some lengthy reasoning we may write for the net radiative transfer between wick and environment:

$$\begin{aligned}\frac{\Delta F_{\mathrm{net}}}{A} &= \sigma\varepsilon_w\left[\frac{1}{2}(1+\varepsilon_a)T_a^4 - T_{nwb}^4\right] \\ &\quad + (1-\alpha_w)S\left[(1-f_{\mathrm{dir}})\left(1+\frac{D}{4L}\right) + f_{\mathrm{dir}}\left(\frac{\tan(\theta)}{\pi}+\frac{D}{4L}\right) + \alpha_{\mathrm{sfc}}\right]\end{aligned} \tag{C.7}$$

with σ the Stefan-Boltzmann constant, ε_w and ε_a the emissivity of the wick and atmosphere respectively, and α_w, α_{sfc} the wick and surface albedo. In Liljegren et al. (2008), a subset of nighttime (for ε_w) and daytime (for α_w and α_{sfc}) WBGT data are compared with model calculations to derive the values $\varepsilon_w = 0.95$, $\alpha_w = 0.4$ and $\alpha_{\mathrm{sfc}} = 0.45$, while atmospheric emissivity is expressed in terms of partial water vapour pressure as $\varepsilon_a = 0.575 e_a^{0.143}$[88]. S denotes the total horizontal shortwave solar irradiance, and f_{dir} is the fraction of S directly due to the beam of the Sun. The solar zenith angle is written as θ. The wetted wick is treated as a cylinder with diameter D and length L.

C.2 Globe Temperature Model

The globe temperature T_g is measured using a hollow metal sphere which is painted black and equipped with an internal temperature sensor. It serves as a proxy for time-dependent radiative and convective heat transfer processes.

The energy balance equation for the globe reads:

$$\begin{aligned}A\varepsilon_g\sigma T_g^4 + Ah(T_g - T_a) &= \frac{A}{2}\varepsilon_g\sigma(\varepsilon_a T_a^4 + \varepsilon_{sfc}T_{sfc}^4) \\ &\quad + \frac{A}{2}(1-\alpha_g)(1-f_{dir})S \\ &\quad + \frac{A}{4\cos\theta}(1-\alpha_g)f_{dir}S \\ &\quad + \frac{A}{2}(1-\alpha_g)\alpha_{sfc}S\end{aligned} \tag{C.8}$$

where A is now the surface area of the metal sphere, ε_g and ε_{sfc} are the globe and surface emissivities, and α_g is the globe albedo. The temperature of the surface is T_{sfc}. The convective heat transfer coefficient h for the sphere is determined using empirical relations[88]. Furthermore, we take $\varepsilon_{sfc}T_{sfc}^4 = T_a^4$. The final equation for T_g is:

$$\begin{aligned}T_g^4 &= \frac{1}{2}(1+\varepsilon_a)T_a^4 \\ &\quad - \frac{h}{\varepsilon_g\sigma}(T_g - T_a) + \frac{S}{2\varepsilon_g\sigma}(1-\alpha_g)\left[1+\left(\frac{1}{2\cos(\theta)}-1\right)f_{dir} + \alpha_{sfc}\right]\end{aligned} \tag{C.9}$$

D The Canadian Fire Weather Index

In this appendix, we explain the calculations of the different components of the Canadian FWI, as introduced in section 3.4.4. We follow the description in the technical report by van Wagner and Pickett (1985) and van Wagner (1987), where more details can be found[145, 146].

D.1 Fine Fuel Moisture Code

The FFMC (like the DMC and DC) comprises two phases: a phase for wetting by rain and a phase for drying. Let FFMC_{t-1} denote the FFMC on the previous day. We first calculate the previous day's fine fuel moisture content as:

$$m_{t-1} = 147.2 \times \frac{101 - \text{FFMC}_{t-1}}{59.5 + \text{FFMC}_{t-1}} \tag{D.1}$$

Effective rainfall P_f is calculated from total rainfall P as:

$$P_f = P - 0.5 \text{ for } P > 0.5 \text{ mm} \tag{D.2}$$

so that in case of rain, the fine fuel moisture content of the current day can be calculated.

$$m_{r_t} = \begin{cases} m_{t-1} + 42.5 P_f \left(e^{\frac{-100}{251 - m_{t-1}}}\right)\left(1 - e^{\frac{-6.93}{P_f}}\right), & m_{t-1} \leq 150 \\ m_{t-1} + 42.5 P_f \left(e^{\frac{-100}{251 - m_{t-1}}}\right)\left(1 - e^{\frac{-6.93}{P_f}}\right) + 0.0015(m_{t-1} - 150)^2 \sqrt{P_f}, & m_{t-1} > 150 \end{cases} \tag{D.3}$$

where we also set $m_{r_t} = 250$ if $m_{r_t} > 250$. The next step is to calculate the equilibrium moisture content for the drying phases:

$$E_d = 0.942\text{RH}^{0.679} + 11e^{\frac{\text{RH}-100}{10}} + 0.18(21.1 - T)(1 - e^{-0.115\text{RH}}) \tag{D.4}$$

with RH the relative humidity (%) and T the temperature (°C) at noon. If $E_d < m_{t-1}$, the log drying rate is determined via:

$$k_d = k_0 \times 0.581 e^{0.0365T} \tag{D.5}$$

with:

$$k_0 = 0.424\left(1 - \left(\frac{\text{RH}}{100}\right)^{1.7}\right) + 0.0694\sqrt{U}\left(1 - \left(\frac{\text{RH}}{100}\right)^{8}\right) \tag{D.6}$$

with U the wind speed (km/h). In this case:

$$m_t = E_d + (m_{t-1} - E_d) \times 10^{-k_d} \tag{D.7}$$

However, if $E_d \geq m_{t-1}$, we must calculate m_t for the wetting phases instead. We have:

$$E_w = 0.618\text{RH}^{0.753} + 10e^{\frac{\text{RH}-100}{10}} + 0.18(21.1 - T)(1 - e^{-0.115\text{RH}}) \tag{D.8}$$

If then $E_w > m_{t-1}$, we determine the log wetting rate:

$$k_w = k_1 \times 0.581e^{0.0365T} \tag{D.9}$$

with:

$$k_1 = 0.424\left(1 - \left(\frac{100 - \text{RH}}{100}\right)^{1.7}\right) + 0.0694\sqrt{U}\left(1 - \left(\frac{100 - \text{RH}}{100}\right)^{8}\right) \tag{D.10}$$

so we obtain:

$$m_t = E_w - (E_w - m_{t-1}) \times 10^{-k_w} \tag{D.11}$$

Lastly, if $E_W \leq m_{t-1} \leq E_d$, we set $m_t = m_{t-1}$. We obtain the current day's FFMC as:

$$\text{FFMC}_t = 59.5 \times \frac{250 - m_t}{147.2 + m_t} \tag{D.12}$$

The FFMC value upon startup of FWI calculations is 85.

D.2 Duff Moisture Code

Let DMC_{t-1} be the DMC on the previous day. The previous day's duff moisture content is:

$$M_{t-1} = 20 + e^{5.6348 - \frac{\text{DMC}_{t-1}}{43.43}} \tag{D.13}$$

Effective rainfall is now calculated as:

$$P_f = 0.92P - 1.27 \text{ for } P > 1.5 \text{ mm} \tag{D.14}$$

so that duff moisture content after rain becomes:

$$M_{r_t} = M_{t-1} + \frac{1000 \cdot P_f}{48.77 + bP_f} \tag{D.15}$$

with slope parameter:

$$b = \begin{cases} \dfrac{100}{0.5 + 0.3\text{DMC}_{t-1}}, & \text{DMC}_{t-1} \leq 33 \\ 14 - 1.3\ln(\text{DMC}_{t-1}), & 33 < \text{DMC}_{t-1} \leq 65 \\ 6.2\ln(\text{DMC}_{t-1}) - 17.2, & \text{DMC}_{t-1} > 65 \end{cases} \tag{D.16}$$

We then set:

$$\text{DMC}_{t-1} = 244.72 - 43.43\ln(M_{r_t} - 20) \tag{D.17}$$

but only if $P > 1.5$ mm. Furthermore, if the right hand side of equation D.17 is negative, then $\text{DMC}_{t-1} = 0$. The log drying rate in duff moisture content is calculated:

$$k_d = 1.894(T_e + 1.1)(100 - \text{RH}) \times L_e \times 10^{-6} \tag{D.18}$$

where $T_e = \max(T, -1.1)$. L_e is the effective day-length, which is tabulated per month[145]. The DMC is now calculated as:

$$\text{DMC}_t = \text{DMC}_{t-1} + 100k_d \tag{D.19}$$

The DMC startup value is 6.

D.3 Drought Code

Let DC_{t-1} be the DC on the previous day. The previous day's DC moisture equivalent is determined using:

$$Q_{t-1} = 800e^{-\frac{\mathrm{DC}_{t-1}}{400}} \tag{D.20}$$

Effective rainfall is now calculated as:

$$P_f = 0.83P - 1.27 \text{ for } P > 2.8 \text{ mm} \tag{D.21}$$

so that the moisture equivalent after rain becomes:

$$Q_{r_t} = Q_{t-1} + 3.937P_f \tag{D.22}$$

We then set:

$$\mathrm{DC}_{t-1} = 400 \ln \left(\frac{800}{Q_{r_t}} \right) \tag{D.23}$$

but only if $P > 2.8$ mm. Furthermore, if the right hand side of equation D.23 is negative, then $\mathrm{DC}_{t-1} = 0$. The potential evapotranspiration is calculated:

$$V = 0.36(T_{12} + 2.8) + L_f \tag{D.24}$$

where $T_e = \max(T, -2.8)$. L_f is the day-length factor, which is tabulated per month[145]. Note that V cannot be negative. The DMC is now calculated as:

$$\mathrm{DC}_t = \mathrm{DC}_{t-1} + 0.5V \tag{D.25}$$

The DC startup value is 15.

D.4 Initial Spread Index

We define the wind function as:

$$f(U) = e^{0.05039U} \tag{D.26}$$

and the fine fuel moisture function as:

$$f(F) = 91.9e^{-0.1386m} \left(1 + \frac{m^{5.31}}{4.93 \times 10^7} \right) \tag{D.27}$$

with m the fuel moisture content, to be determined using equation D.1. We then set:

$$\mathrm{ISI} = 0.208 \times f(U) \times f(F) \tag{D.28}$$

D.5 Buildup Index

If $\mathrm{DMC} \leq 0.4 \times \mathrm{DC}$, we set:

$$\mathrm{BUI} = 0.8 \times \frac{\mathrm{DMC} \times \mathrm{DC}}{\mathrm{DMC} + 0.4\mathrm{DC}} \tag{D.29}$$

Otherwise:

$$\mathrm{BUI} = \mathrm{DMC} - \left(1 - \frac{0.8\mathrm{DC}}{\mathrm{DMC} + 0.4\mathrm{DC}} \right) \times \left[0.92 + (0.0114\mathrm{DMC})^{1.7} \right] \tag{D.30}$$

D.6 Fire Weather Index

BUI is first converted to a measure of mass of fuel consumed via the equation:

$$f(D) = \begin{cases} 0.626\text{BUI}^{0.809} + 2, & \text{BUI} \leq 80 \\ \dfrac{1000}{25 + 108.64e^{-0.023\text{BUI}}}, & \text{BUI} > 80 \end{cases} \tag{D.31}$$

We then calculate the FWI using:

$$\text{FWI} = \begin{cases} e^{2.72(0.434 \ln B)^{0.647}}, & B > 1 \\ B, & B \leq 1 \end{cases} \tag{D.32}$$

with:

$$B = 0.1 \times \text{ISI} \times f(D) \tag{D.33}$$

Bibliography

[1] A. Fischer, K. Strassmann, M. Croci-Maspoli, A. Hama, R. Knutti, S. Kotlarski, C. Schär, C. Schnadt Poberaj, N. Ban, M. Bavay, U. Beyerle, D. Bresch, S. Brönnimann, P. Burlando, A. Casanueva, S. Fatichi, I. Feigenwinter, E. Fischer, M. Hirschi, M. Liniger, C. Marty, I. Medhaug, N. Peleg, M. Pickl, C. Raible, J. Rajczak, O. Rössler, S. Scherrer, C. Schwierz, S. Seneviratne, M. Skelton, S. Sørland, C. Spirig, F. Tschurr, J. Zeder, and E. Zubler, "Climate Scenarios for Switzerland CH2018 – Approach and Implications," *Climate Services*, vol. 26, 2022.

[2] GISTEMP Team, "GISS Surface Temperature Analysis (GISTEMP), Version 4," 2025.

[3] F. Duchêne, B. V. Schaeybroeck, S. Caluwaerts, R. D. Troch, R. Hamdi, and P. Termonia, "A Statistical–Dynamical Methodology to Downscale Regional Climate Projections to Urban Scale," *Journal of Applied Meteorology and Climatology*, vol. 59, no. 6, pp. 1109 – 1123, 2020.

[4] World Climate Research Programme (WCRP), "Coordinated Regional Climate Downscaling Experiment (CORDEX)," 2024.

[5] I. Lehtonen, K. Ruosteenoja, A. Venäläinen, and H. Gregow, "The Projected 21st Century Forest-Fire Risk in Finland Under Different Greenhouse Gas Scenarios," 2014.

[6] United States Department of Agriculture (USDA), "Invasive.org," 2018.

[7] K. Abbass, M. Z. Qasim, H. Song, M. Murshed, H. Mahmood, and I. Younis, "A Review of the Global Climate Change Impacts, Adaptation, and Sustainable Mitigation Measures," *Environmental Science and Pollution Research*, vol. 29, pp. 42539–42559, Apr. 2022.

[8] Intergovernmental Panel on Climate Change (IPCC), *Weather and Climate Extreme Events in a Changing Climate*, p. 1513–1766. Cambridge University Press, 2023.

[9] M. Journée, E. Goudenhoofdt, S. Vannitsem, and L. Delobbe, "Quantitative Rainfall Analysis of the 2021 Mid-July Flood Event in Belgium," *Hydrology and Earth System Sciences*, vol. 27, no. 17, pp. 3169–3189, 2023.

[10] Royal Meteorological Institute, "Dry Spring 2025," 2025.

[11] K. van der Wiel, G. Lenderink, and H. de Vries, "Physical Storylines of Future European Drought Events Like 2018 Based on Ensemble Climate Modelling," *Weather and Climate Extremes*, vol. 33, p. 100350, 2021.

[12] G. J. van Oldenborgh, K. van der Wiel, S. Kew, S. Philip, F. Otto, R. Vautard, A. King, F. Lott, J. Arrighi, R. Singh, and M. van Aalst, "Pathways and Pitfalls in Extreme Event Attribution," *Climatic Change*, vol. 166, p. 13, May 2021.

[13] R. Vautard, J. Cattiaux, T. Happé, J. Singh, R. Bonnet, C. Cassou, D. Coumou, F. D'Andrea, D. Faranda, E. Fischer, A. Ribes, S. Sippel, and P. Yiou, "Heat Extremes in Western Europe Increasing Faster Than Simulated due to Atmospheric Circulation Trends," *Nature Communications*, vol. 14, p. 6803, Oct 2023.

[14] D. G. Miralles, P. Gentine, S. I. Seneviratne, and A. J. Teuling, "Land–Atmospheric Feedbacks During Droughts and Heatwaves: State of the Science and Current Challenges," *Annals of the New York Academy of Sciences*, vol. 1436, no. 1, pp. 19–35, 2019.

[15] Intergovernmental Panel on Climate Change (IPCC), "Climate Change 2023: Synthesis Report. Contribution of Working Groups I, II and III to the Sixth Assessment Report of the Intergovernmental Panel on Climate Change," pp. 35–115, 2023.

[16] H. de Vries, G. Lenderink, E. van Meijgaard, B. van Ulft, and W. de Rooy, "Western Europe's Extreme July 2019 Heatwave in a Warmer World," *Environmental Research: Climate*, vol. 3, jun 2024.

[17] M. Rantanen, A. Y. Karpechko, A. Lipponen, K. Nordling, O. Hyvärinen, K. Ruosteenoja, T. Vihma, and A. Laaksonen, "The Arctic has Warmed Nearly Four Times Faster Than the Globe Since 1979," *Communications Earth & Environment*, vol. 3, p. 168, Aug 2022.

[18] Z. Liu, W. Zhan, B. Bechtel, J. Voogt, J. Lai, T. Chakraborty, Z.-H. Wang, M. Li, F. Huang, and X. Lee, "Surface Warming in Global Cities is Substantially More Rapid Than in Rural Background Areas," *Communications Earth & Environment*, vol. 3, p. 219, Sep 2022.

[19] Royal Meteorological Institute, *De Evolutie van het Klimaat in België*, pp. 4–32. D. Gellens, 2020.

[20] W. Hazeleger, B. J. J. M. van den Hurk, E. Min, G. J. van Oldenborgh, A. C. Petersen, D. A. Stainforth, E. Vasileiadou, and L. A. Smith, "Tales of Future Weather," *Nature Climate Change*, vol. 5, pp. 107–113, Feb 2015.

[21] J. Sillmann, T. G. Shepherd, B. van den Hurk, W. Hazeleger, O. Martius, J. Slingo, and J. Zscheischler, "Event-Based Storylines to Address Climate Risk," *Earth's Future*, vol. 9, no. 2, 2021.

[22] T. G. Shepherd, "A Common Framework for Approaches to Extreme Event Attribution," *Current Climate Change Reports*, vol. 2, pp. 28–38, Mar 2016.

[23] T. G. Shepherd, E. Boyd, R. A. Calel, S. C. Chapman, S. Dessai, I. M. Dima-West, H. J. Fowler, R. James, D. Maraun, O. Martius, C. A. Senior, A. H. Sobel, D. A. Stainforth, S. F. B. Tett, K. E. Trenberth, B. J. J. M. van den Hurk, N. W. Watkins, R. L. Wilby, and D. A. Zenghelis, "Storylines: an Alternative Approach to Representing Uncertainty in Physical Aspects of Climate Change," *Climatic Change*, vol. 151, pp. 555–571, Dec 2018.

[24] A. Ciullo, O. Martius, E. Strobl, and D. N. Bresch, "A Framework for Building Climate Storylines Based on Downward Counterfactuals: The Case of the European Union Solidarity Fund," *Climate Risk Management*, vol. 33, p. 100349, 2021.

[25] S. E. Perkins-Kirkpatrick, L. V. Alexander, A. D. King, S. F. Kew, S. Y. Philip, C. Barnes, D. Maraun, R. F. Stuart-Smith, A. Jézéquel, E. Bevacqua, S. Burgess, E. Fischer, G. C. Hegerl, J. Kimutai, G. Koren, K. A. Lawal, S.-K. Min, M. New, R. C. Odoulami, C. M. Patricola, I. Pinto, A. Ribes, T. A. Shaw, W. Thiery, B. Trewin, R. Vautard, M. Wehner, and J. Zscheischler, "Frontiers in Attributing Climate Extremes and Associated Impacts," *Frontiers in Climate*, vol. 6, 2024.

[26] B. J. van den Hurk, M. Baldissera Pacchetti, E. Boere, A. Ciullo, L. Coulter, S. Dessai, E. Ercin, H. M. Goulart, R. Hamed, S. Hochrainer-Stigler, E. Koks, P. Kubiczek, A. Levermann, R. Mechler, M. van Meersbergen, B. Mester, R. Middelanis, K. Minderhoud, J. Mysiak, S. Nirandjan, G. van den Oord, C. Otto, P. Sayers, J. Schewe, T. G. Shepherd, J. Sillmann, D. Stuparu, T. Vogt,

and K. Witpas, "Climate Impact Storylines for Assessing Socio-Economic Responses to Remote Events," *Climate Risk Management*, vol. 40, p. 100500, 2023.

[27] E. M. Fischer, U. Beyerle, L. Bloin-Wibe, C. Gessner, V. Humphrey, F. Lehner, A. G. Pendergrass, S. Sippel, J. Zeder, and R. Knutti, "Storylines for Unprecedented Heatwaves Based on Ensemble Boosting," *Nature Communications*, vol. 14, p. 4643, Aug 2023.

[28] P. Ailliot, D. Allard, V. Monbet, and P. Naveau, "Stochastic Weather Generators: an Overview of Weather Type Models," *Journal de la société française de statistique*, vol. 156, no. 1, pp. 101–113, 2015.

[29] P. Yiou, "AnaWEGE: a Weather Generator Based on Analogues of Atmospheric Circulation," *Geoscientific Model Development*, vol. 7, no. 2, pp. 531–543, 2014.

[30] P. Yiou and A. Jézéquel, "Simulation of Extreme Heat Waves With Empirical Importance Sampling," *Geoscientific Model Development*, vol. 13, no. 2, pp. 763–781, 2020.

[31] P. Pfleiderer, A. Jézéquel, J. Legrand, N. Legrix, I. Markantonis, E. Vignotto, and P. Yiou, "Simulating Compound Weather Extremes Responsible for Critical Crop Failure With Stochastic Weather Generators," *Earth System Dynamics*, vol. 12, no. 1, pp. 103–120, 2021.

[32] M. I. Brunner, E. Gilleland, and A. W. Wood, "Space-Time Dependence of Compound Hot-Dry Events in the United States: Assessment Using a Multi-Site Multi-Variable Weather Generator," *Earth System Dynamics*, vol. 12, no. 2, pp. 621–634, 2021.

[33] T. Schreiber and A. Schmitz, "Surrogate Time Series," *Physica D: Nonlinear Phenomena*, vol. 142, no. 3, pp. 346–382, 2000.

[34] C. Schär, C. Frei, D. Lüthi, and H. C. Davies, "Surrogate Climate-Change Scenarios for Regional Climate Models," *Geophysical Research Letters*, vol. 23, no. 6, pp. 669–672, 1996.

[35] P. Yiou, R. Vautard, Y. Robin, N. de Noblet-Ducoudré, F. D'Andrea, and R. Noyelle, "How Could 50 °C be Reached in Paris: Analyzing the CMIP6 Ensemble to Design Storylines for Adaptation," *Climate Services*, vol. 36, p. 100518, 2024.

[36] J. Bessembinder, R. Bintanja, R. van Dorland, C. Homan, B. Overbeek, F. Selten, and P. Siegmund, "KNMI'23-Klimaatscenario's voor Nederland," tech. rep., Royal Netherlands Meteorological Institute, 2023.

[37] Royal Meteorological Institute, "Verwachtingen voor 5 juli 2063," 2019.

[38] C. Bertrand, R. Ingels, and M. Journée, "Homogenization and Trends Analysis of the Belgian Historical Precipitation Time Series," *International Journal of Climatology*, vol. 41, no. 11, pp. 5277–5294, 2021.

[39] M. J. Menne, C. N. Williams Jr., and M. A. Palecki, "On the Reliability of the U.S. Surface Temperature Record," *Journal of Geophysical Research: Atmospheres*, vol. 115, 2010.

[40] C. Bertrand, V. Vrábeĺ, C. Delvaux, M. Alioscha-Perez, and H. Sahli, "BEL-HORNET: Belgian Homogenized Long-Term Reference Climate Time Series," tech. rep., Belgian Science Policy Office, 2018.

[41] C. Delvaux, R. Ingels, V. Vrábeĺ, M. Journée, and C. Bertrand, "Quality Control and Homogenization of the Belgian Historical Temperature Data," *International Journal of Climatology*, vol. 39, no. 1, pp. 157–171, 2019.

[42] J. Hansen, R. Ruedy, M. Sato, and K. Lo, "Global Surface Temperature Change," *Reviews of Geophysics*, vol. 48, no. 4, 2010.

[43] N. Lenssen, G. A. Schmidt, M. Hendrickson, P. Jacobs, M. J. Menne, and R. Ruedy, "A NASA GISTEMPv4 Observational Uncertainty Ensemble," *Journal of Geophysical Research: Atmospheres*, vol. 129, no. 17, 2024.

[44] Vlaamse Overheid, "Waterinfo," 2025.

[45] Waterinfo, "Watertemperaturen – Lillo Meetpaal." `https://www.waterinfo.vlaanderen.be/Meetreeksen`, 2022. Accessed: May 2025.

[46] R. C. Cornes, G. van der Schrier, E. J. M. van den Besselaar, and P. D. Jones, "An Ensemble Version of the E-OBS Temperature and Precipitation Data Sets," *Journal of Geophysical Research: Atmospheres*, vol. 123, no. 17, pp. 9391–9409, 2018.

[47] Copernicus Climate Change Service, Climate Data Store, "E-OBS Daily Gridded Meteorological Data for Europe From 1950 to Present Derived From In-Situ Observations," 2020.

[48] European Climate Assessment Dataset, "Daily Data," 2025.

[49] European Centre for Medium-Range Weather Forecasts (ECMWF), "ECMWF Reanalysis v5 (ERA5)," 2024.

[50] J. Muñoz Sabater, "ERA5-Land Hourly Data From 1950 to Present. Copernicus Climate Change Service (C3S) Climate Data Store (CDS)," 2019.

[51] J. Monteith and M. Unsworth, *Principles of Environmental Physics: Plants, Animals, and the Atmosphere*. Academic Press, 2013.

[52] J. Holton and G. Hakim, *An Introduction to Dynamic Meteorology*. International Geophysics, Academic Press, 2012.

[53] M. Auffhammer, S. M. Hsiang, and W. Schlenker, "Global Climate Models and Climate Data: A User Guide for Economists," 2011.

[54] R. L. Wilby, J. Troni, Y. Biot, L. Tedd, B. C. Hewitson, D. M. Smith, and R. T. Sutton, "A Review of Climate Risk Information for Adaptation and Development Planning," *International Journal of Climatology*, vol. 29, no. 9, pp. 1193–1215, 2009.

[55] P. Termonia, B. Van Schaeybroeck, L. De Cruz, R. De Troch, S. Caluwaerts, O. Giot, R. Hamdi, S. Vannitsem, F. Duchêne, P. Willems, H. Tabari, E. Van Uytven, P. Hosseinzadehtalaei, N. Van Lipzig, H. Wouters, S. Vanden Broucke, J.-P. van Ypersele, P. Marbaix, C. Villanueva-Birriel, X. Fettweis, C. Wyard, C. Scholzen, S. Doutreloup, K. De Ridder, A. Gobin, D. Lauwaet, T. Stavrakou, M. Bauwens, J.-F. Müller, P. Luyten, S. Ponsar, D. Van den Eynde, and E. Pottiaux, "The CORDEX.be Initiative as a Foundation for Climate Services in Belgium," *Climate Services*, vol. 11, pp. 49–61, 2018.

[56] L. R. Leung, *Regional Climate Models*, pp. 8902–8919. New York, NY: Springer New York, 2012.

[57] Z. Xu, Y. Han, and Z. Yang, "Dynamical Downscaling of Regional Climate: A Review of Methods and Limitations," *Science China Earth Sciences*, vol. 62, pp. 365–375, Feb 2019.

[58] W. C. R. P. (WCRP), "Coordinated Regional Climate Downscaling Experiment - European Domain (EURO-CORDEX)," 2024.

[59] E. Katragkou, S. P. Sobolowski, C. Teichmann, F. Solmon, V. Pavlidis, D. Rechid, P. Hoffmann, J. Fernandez, G. Nikulin, and D. Jacob, "Delivering an Improved Framework for the New Generation of CMIP6-Driven EURO-CORDEX Regional Climate Simulations," *Bulletin of the American Meteorological Society*, vol. 105, no. 6, 2024.

[60] D. Jacob, C. Teichmann, S. Sobolowski, E. Katragkou, I. Anders, M. Belda, R. Benestad, F. Boberg, E. Buonomo, R. M. Cardoso, A. Casanueva, O. B. Christensen, J. H. Christensen, E. Coppola, L. De Cruz, E. L. Davin, A. Dobler, M. Domínguez, R. Fealy, J. Fernandez, M. A. Gaertner, M. García-Díez, F. Giorgi, A. Gobiet, K. Goergen, J. J. Gómez-Navarro, J. J. G. Alemán, C. Gutiérrez, J. M. Gutiérrez, I. Güttler, A. Haensler, T. Halenka, S. Jerez, P. Jiménez-Guerrero, R. G. Jones, K. Keuler, E. Kjellström, S. Knist, S. Kotlarski, D. Maraun, E. van Meijgaard, P. Mercogliano, J. P. Montávez, A. Navarra, G. Nikulin, N. de Noblet-Ducoudré, H.-J. Panitz, S. Pfeifer, M. Piazza, E. Pichelli, J.-P. Pietikäinen, A. F. Prein, S. Preuschmann, D. Rechid, B. Rockel, R. Romera, E. Sánchez, K. Sieck, P. M. M. Soares, S. Somot, L. Srnec, S. L. Sørland, P. Termonia, H. Truhetz, R. Vautard, K. Warrach-Sagi, and V. Wulfmeyer, "Regional Climate Downscaling Over Europe: Perspectives From the EURO-CORDEX Community," *Regional Environmental Change*, vol. 20, p. 51, Apr 2020.

[61] R. Moss, M. Babiker, S. Brinkman, E. Calvo, T. Carter, J. Edmonds, I. Elgizouli, S. Emori, E. Lin, K. Hibbard, R. Jones, M. Kainuma, J. Kelleher, J.-F. Lamarque, M. Manning, B. Matthews, J. Meehl, L. Meyer, J. Mitchell, and M. Zurek, "Towards New Scenarios for Analysis of Emissions, Climate Change, Impacts, and Response Strategies. Technical Summary," 2008.

[62] C. Schwingshackl, A. S. Daloz, C. Iles, K. Aunan, and J. Sillmann, "High-Resolution Projections of Ambient Heat for Major European Cities Using Different Heat Metrics," *Natural Hazards and Earth System Sciences*, vol. 24, no. 1, pp. 331–354, 2024.

[63] E. Coppola, R. Nogherotto, J. M. Ciarlo', F. Giorgi, E. van Meijgaard, N. Kadygrov, C. Iles, L. Corre, M. Sandstad, S. Somot, P. Nabat, R. Vautard, G. Levavasseur, C. Schwingshackl, J. Sillmann, E. Kjellström, G. Nikulin, E. Aalbers, G. Lenderink, O. B. Christensen, F. Boberg, S. L. Sørland, M.-E. Demory, K. Bülow, C. Teichmann, K. Warrach-Sagi, and V. Wulfmeyer, "Assessment of the European Climate Projections as Simulated by the Large EURO-CORDEX Regional and Global Climate Model Ensemble," *Journal of Geophysical Research: Atmospheres*, vol. 126, no. 4, 2021.

[64] V. Eyring, S. Bony, G. A. Meehl, C. A. Senior, B. Stevens, R. J. Stouffer, and K. E. Taylor, "Overview of the Coupled Model Intercomparison Project Phase 6 (CMIP6) Experimental Design and Organization," *Geoscientific Model Development*, vol. 9, no. 5, pp. 1937–1958, 2016.

[65] "The CMIP6 landscape," *Nature Climate Change*, vol. 9, pp. 727–727, Oct 2019.

[66] F. Duchêne, R. Hamdi, B. Van Schaeybroeck, S. Caluwaerts, R. De Troch, L. de Cruz, and P. Termonia, "Downscaling Ensemble Climate Projections to Urban Scale: Brussels's Future Climate at 1.5 °C, 2 °C, and 3 °C Global Warming," *Urban Climate*, vol. 46, p. 101319, 2022.

[67] V. Masson, P. Le Moigne, E. Martin, S. Faroux, A. Alias, R. Alkama, S. Belamari, A. Barbu, A. Boone, F. Bouyssel, P. Brousseau, E. Brun, J.-C. Calvet, D. Carrer, B. Decharme, C. Delire, S. Donier, K. Essaouini, A.-L. Gibelin, H. Giordani, F. Habets, M. Jidane, G. Kerdraon, E. Kourzeneva, M. Lafaysse, S. Lafont, C. Lebeaupin Brossier, A. Lemonsu, J.-F. Mahfouf, P. Marguinaud, M. Mokhtari, S. Morin, G. Pigeon, R. Salgado, Y. Seity, F. Taillefer, G. Tanguy, P. Tulet, B. Vincendon, V. Vionnet, and A. Voldoire, "The SURFEXv7.2 Land and Ocean Surface Platform for Coupled or Offline Simulation of Earth Surface Variables and Fluxes," *Geoscientific Model Development*, vol. 6, no. 4, pp. 929–960, 2013.

[68] Ghent University, "The Vlinder Project," 2018.

[69] J. Finkel and P. A. O'Gorman, "Bringing Statistics to Storylines: Rare Event Sampling for Sudden, Transient Extreme Events," *Journal of Advances in Modeling Earth Systems*, vol. 16, no. 6, 2024.

[70] P. Yiou, C. Cadiou, D. Faranda, A. Jézéquel, N. Malhomme, G. Miloshevich, R. Noyelle, F. Pons, Y. Robin, and M. Vrac, "Ensembles of Climate Simulations to Anticipate Worst Case Heatwaves During the Paris 2024 Olympics," *npj Climate and Atmospheric Science*, vol. 6, p. 188, Nov 2023.

[71] S. Coles, *An Introduction to Statistical Modeling of Extreme Values*. Springer Series in Statistics, Springer London, 2013.

[72] C. Navarro-Racines, J. Tarapues, P. Thornton, A. Jarvis, and J. Ramirez-Villegas, "High-Resolution and Bias-Corrected CMIP5 Projections for Climate Change Impact Assessments," *Scientific Data*, vol. 7, Jan 2020.

[73] D. Maraun, "Bias Correcting Climate Change Simulations - a Critical Review," *Current Climate Change Reports*, vol. 2, pp. 211–220, Dec 2016.

[74] R. Vautard, P. Yiou, Y. Robin, N. de Noblet, F. d'Andrea, and L. Abbadie, "Simulations de Scénarios 'Paris 50°C'," tech. rep., GREC francilien, June 2023.

[75] C. H. Simpson, O. Brousse, and C. Heaviside, "Estimated Mortality Attributable to the Urban Heat Island During the Record-Breaking 2022 Heatwave in London," *Environmental Research Letters*, vol. 19, aug 2024.

[76] E. Hawkins, D. Frame, L. Harrington, M. Joshi, A. King, M. Rojas, and R. Sutton, "Observed Emergence of the Climate Change Signal: From the Familiar to the Unknown," *Geophysical Research Letters*, vol. 47, no. 6, 2020.

[77] Z. Zhong, B. He, H. W. Chen, D. Chen, T. Zhou, W. Dong, C. Xiao, S.-p. Xie, X. Song, L. Guo, R. Ding, L. Zhang, L. Huang, W. Yuan, X. Hao, D. Ji, and X. Zhao, "Reversed Asymmetric Warming of Sub-Diurnal Temperature Over Land During Recent Decades, journal=Nature Communications," vol. 14, p. 7189, Nov 2023.

[78] T. R. Karl, P. D. Jones, R. W. Knight, G. Kukla, N. Plummer, V. Razuvayev, K. P. Gallo, J. Lindseay, R. J. Charlson, and T. C. Peterson, "A New Perspective on Recent Global Warming: Asymmetric Trends of Daily Maximum and Minimum Temperature," *Bulletin of the American Meteorological Society*, vol. 74, no. 6, pp. 1007 – 1024, 1993.

[79] Q.-V. Doan, F. Chen, Y. Asano, Y. Gu, A. Nishi, H. Kusaka, and D. Niyogi, "Causes for Asymmetric Warming of Sub-Diurnal Temperature Responding to Global Warming," *Geophysical Research Letters*, vol. 49, no. 20, 2022.

[80] Y. Dodge, *The Concise Encyclopedia of Statistics*. Springer New York, 2008.

[81] H. B. Mann and D. R. Whitney, "On a Test of Whether one of Two Random Variables is Stochastically Larger Than the Other," *The Annals of Mathematical Statistics*, vol. 18, no. 1, pp. 50 – 60, 1947.

[82] M. DeGroot and M. Schervish, *Probability and Statistics*. Addison-Wesley, 2012.

[83] N. Smirnov, "Table for Estimating the Goodness of Fit of Empirical Distributions," *The Annals of Mathematical Statistics*, vol. 19, no. 2, pp. 279 – 281, 1948.

[84] D. Knuth, *The Art of Computer Programming: Seminumerical Algorithms, Volume 2*. Pearson Education, 2014.

[85] R. S. Kovats and S. Hajat, "Heat Stress and Public Health: a Critical Review," *Annual Review of Public Health*, vol. 29, no. Volume 29, 2008, pp. 41–55, 2008.

[86] K. Parsons, *Human Thermal Environments: the Effects of Hot, Moderate, and Cold Environments on Human Health, Comfort and Performance*. CRC press, 2007.

[87] T. Kjellstrom, "Climate Change, Direct Heat Exposure, Health and Well-Being in Low and Middle-Income Countries," *Global Health Action*, vol. 2, no. 1, p. 1958, 2009.

[88] J. C. Liljegren, R. A. Carhart, P. Lawday, S. Tschopp, and R. Sharp, "Modeling the Wet Bulb Globe Temperature Using Standard Meteorological Measurements," *Journal of Occupational and Environmental Hygiene*, vol. 5, no. 10, pp. 645–655, 2008.

[89] B. Lemke and T. Kjellstrom, "Calculating Workplace WBGT From Meteorological Data: A Tool for Climate Change Assessment," *Industrial Health*, vol. 50, no. 4, pp. 267–278, 2012.

[90] Q. Kong and M. Huber, "Explicit Calculations of Wet-Bulb Globe Temperature Compared With Approximations and Why It Matters for Labor Productivity," *Earth's Future*, vol. 10, no. 3, 2022.

[91] T. Kjellstrom, I. Holmer, and B. Lemke, "Workplace Heat Stress, Health and Productivity – an Increasing Challenge for Low and Middle-Income Countries During Climate Change," *Global Health Action*, vol. 2, no. 1, p. 2047, 2009.

[92] A. Casanueva, S. Kotlarski, A. M. Fischer, A. D. Flouris, T. Kjellstrom, B. Lemke, L. Nybo, C. Schwierz, and M. A. Liniger, "Escalating Environmental Summer Heat Exposure - a Future Threat for the European Workforce," *Regional Environmental Change*, vol. 20, p. 40, Mar 2020.

[93] "ISO 7243: Ergonomics of the Thermal Environment—Assessment of Heat Stress Using the WBGT (Wet Bulb Globe Temperature) Index," tech. rep., International Organization for Standardization, 2017.

[94] P. Bröde, D. Fiala, B. Lemke, and T. Kjellstrom, "Estimated Work Ability in Warm Outdoor Environments Depends on the Chosen Heat Stress Assessment Metric," *International Journal of Biometeorology*, vol. 62, pp. 331–345, Mar 2018.

[95] M. C. Almeida and P. S. Coelho, "Modeling River Water Temperature With Limiting Forcing Data: Air2stream v1.0.0, Machine Learning and Multiple Regression," *Geoscientific Model Development*, vol. 16, no. 14, pp. 4083–4112, 2023.

[96] F. Petrakopoulou, A. Robinson, and M. Olmeda-Delgado, "Impact of Climate Change on Fossil Fuel Power-Plant Efficiency and Water Use," *Journal of Cleaner Production*, vol. 273, p. 122816, 2020.

[97] F. Petrakopoulou, "Defining the Cost of Water Impact for Thermoelectric Power Generation," *Energy Reports*, vol. 7, pp. 2101–2112, 2021.

[98] H. Koch and S. Vögele, "Dynamic Modelling of Water Demand, Water Availability and Adaptation Strategies for Power Plants to Global Change," *Ecological Economics*, vol. 68, no. 7, pp. 2031–2039, 2009.

[99] A. Rabi, M. Hadzima-Nyarko, and M. Šperac, "Modelling River Temperature From Air Temperature: Case of the River Drava (Croatia)," *Hydrological Sciences Journal*, vol. 60, no. 9, pp. 1490–1507, 2015.

[100] R. Kruk, J. Van Geertsom, A. Royen, and N. Bourland, "Is Belgium Ready for More Frequent and Intense Wildfires? Analysis of the Belgian State of Play and Insights From the International Context," tech. rep., Climate Risk Assessment Center and National Geographic Institute, 2025.

[101] B. Lawson and O. Armitage, "Weather Guide for the Canadian Forest Fire Danger Rating System," *Natural Resources Canada*, 2008.

[102] M. Kogan and R. Prokopy, "Chapter 3 - Agricultural Entomology," in *Encyclopedia of Insects* (V. H. Resh and R. T. Cardé, eds.), San Diego: Academic Press, second edition ed., 2009.

[103] P. C. Tobin, S. Nagarkatti, G. Loeb, and M. C. Saunders, "Historical and Projected Interactions Between Climate Change and Insect Voltinism in a Multivoltine Species," *Global Change Biology*, vol. 14, no. 5, pp. 951–957, 2008.

[104] O. H. Berteloot, A. Kuhn, G. Peusens, T. Beliën, L. Hautier, T. V. Leeuwen, and P. D. Clercq, "Distribution and Genetic Diversity of the Invasive Pest Halyomorpha halys (Hemiptera, Pentatomidae) in Belgium," *NeoBiota*, vol. 90, pp. 123–138, 2024.

[105] EPPO Global Database, "First Report of Popillia japonica in Switzerland," 2017.

[106] European Parliament, "Discovery of Pest 'False Codling Moth' on Fruit From Morocco," 2023.

[107] European Commission, "Commission Delegated Regulation (EU) 2019/1702 of 1 August 2019 Supplementing Regulation (EU) 2016/2031 of the European Parliament and of the Council by Establishing the List of Priority Pests," 2019.

[108] D. Kriticos, G. Maywald, T. Yonow, E. Zurcher, N. Herrmann, and B. Sutherst, "CLIMEX Version 4: Exploring the Effects of Climate on Plants, Animals and Diseases," 2016.

[109] D. J. Kriticos, J. M. Kean, C. B. Phillips, S. D. Senay, H. Acosta, and T. Haye, "The Potential Global Distribution of the Brown Marmorated Stink Bug, Halyomorpha halys, a Critical Threat to Plant Biosecurity," *Journal of Pest Science*, vol. 90, pp. 1033–1043, Sep 2017.

[110] E. J. Kistner-Thomas, "The Potential Global Distribution and Voltinism of the Japanese Beetle (Coleoptera: Scarabaeidae) Under Current and Future Climates," *Journal of Insect Science*, vol. 19, no. 2, p. 16, 2019.

[111] B. Barker and L. Coop, "False Codling Moth (Thaumatotibia leucotreta) (Lepidoptera: Tortricidae): Phenology/Degree-Day and Climate Suitability Model Analysis for USPEST.ORG," 2019. Prepared for USDA APHIS PPQ.

[112] J. Van Nieuwenhuyse, B. Van Schaeybroeck, S. Caluwaerts, J. De Deyn, A. Delcloo, R. De Troch, R. Hamdi, and P. Termonia, "Air-Stagnation Episodes Based on Regional Climate Models Part I: Evaluation Over Europe," *Climate Dynamics*, vol. 61, pp. 2121–2138, Sep 2023.

[113] J. O. Anderson, J. G. Thundiyil, and A. Stolbach, "Clearing the Air: A Review of the Effects of Particulate Matter Air Pollution on Human Health," *Journal of Medical Toxicology*, vol. 8, pp. 166–175, Jun 2012.

[114] World Health Organization, "Review of Evidence on Health Aspects of Air Pollution – REVIHAAP Project: Technical Report," tech. rep., World Health Organization Regional Office for Europe, 2013.

[115] A. P. K. Tai, M. V. Martin, and C. L. Heald, "Threat to Future Global Food Security From Climate Change and Ozone Air Pollution," *Nature Climate Change*, vol. 4, pp. 817–821, Sep 2014.

[116] D. E. Horton, Harshvardhan, and N. S. Diffenbaugh, "Response of Air Stagnation Frequency to Anthropogenically Enhanced Radiative Forcing," *Environmental Research Letters*, vol. 7, nov 2012.

[117] E. Elnagar, S. Gendebien, E. Georges, U. Berardi, S. Doutreloup, and V. Lemort, "Framework to Assess Climate Change Impact on Heating and Cooling Energy Demands in Building Stock: A Case Study of Belgium in 2050 and 2100," *Energy and Buildings*, vol. 298, p. 113547, 2023.

[118] D. Crawley, "EnergyPlus: A New-Generation Building Energy Simulation Program," 1999.

[119] R. Guglielmetti, D. Macumber, and N. Long, "OpenStudio: An Open Source Integrated Analysis Platform; Preprint," National Renewable Energy Lab. (NREL), 2011.

[120] P. K. Dunn, "Bootstrap Confidence Intervals for Predicted Rainfall Quantiles," *International Journal of Climatology*, vol. 21, no. 1, pp. 89–94, 2001.

[121] J. L. Horowitz, "Bootstrap Methods in Econometrics," *Annual Review of Economics*, vol. 11, pp. 193–224, 2019.

[122] Royal Netherlands Meteorological Institute, "Nederland Warmt Ruim 2 Keer zo Snel op als de Wereldgemiddelde Temperatuur," 2021.

[123] Royal Meteorological Institute, "Juli 2019: Absolute Warmterecord Gebroken," 2019.

[124] FOD Volksgezondheid, Veiligheid van de Voedselketen en Leefmilieu, "Ozon- en Hitteplan," 2019.

[125] Royal Meteorological Institute, "Legend Heat," 2025.

[126] Royal Meteorological Institute, "Klimaatnormalen te Ukkel," 2025.

[127] Royal Meteorological Institute, "Klimatologische Overzichten van 2024," 2024.

[128] L. Schepers, B. Haest, S. Veraverbeke, T. Spanhove, J. Vanden Borre, and R. Goossens, "Burned Area Detection and Burn Severity Assessment of a Heathland Fire in Belgium Using Airborne Imaging Spectroscopy (APEX)," *Remote Sensing*, vol. 6, no. 3, pp. 1803–1826, 2014.

[129] A. Depicker, B. De Baets, and J. M. Baetens, "Wildfire Ignition Probability in Belgium," *Natural Hazards and Earth System Sciences*, vol. 20, no. 2, pp. 363–376, 2020.

[130] Copernicus Emergency Management Service, *The European Forest Fire Information System: User Guide to EFFIS Applications*, May 2018. Version 2.3.3.

[131] A. Mastai, "Storylines of Future Climate Extremes in Switzerland," April 2022.

[132] P. Yiou, D. Faranda, S. Thao, and M. Vrac, "Projected Changes in the Atmospheric Dynamics of Climate Extremes in France," *Atmosphere*, vol. 12, no. 11, 2021.

[133] C. C. Ibebuchi and I.-O. Abu, "Characterization of Temperature Regimes in Western Europe, as Regards the Summer 2022 Western European Heat Wave," *Climate Dynamics*, vol. 61, pp. 3707–3720, Oct 2023.

[134] S. Y. Philip, S. F. Kew, G. J. van Oldenborgh, F. S. Anslow, S. I. Seneviratne, R. Vautard, D. Coumou, K. L. Ebi, J. Arrighi, R. Singh, M. van Aalst, C. Pereira Marghidan, M. Wehner, W. Yang, S. Li, D. L. Schumacher, M. Hauser, R. Bonnet, L. N. Luu, F. Lehner, N. Gillett, J. S. Tradowsky, G. A. Vecchi, C. Rodell, R. B. Stull, R. Howard, and F. E. L. Otto, "Rapid Attribution Analysis of the Extraordinary Heat Wave on the Pacific Coast of the US and Canada in June 2021," *Earth System Dynamics*, vol. 13, no. 4, pp. 1689–1713, 2022.

[135] L. Bloin-Wibe, R. Noyelle, V. Humphrey, U. Beyerle, R. Knutti, and E. Fischer, "Estimating Return Periods for Extreme Events in Climate Models Through Ensemble Boosting," *EGUsphere*, vol. 2025, pp. 1–40, 2025.

[136] L. Corre, A. Ribes, S. Bernus, A. Drouin, S. Morin, and J.-M. Soubeyroux, "Using Regional Warming Levels to Describe Future Climate Change for Services and Adaptation: Application to the French Reference Trajectory for Adaptation," *Climate Services*, vol. 38, p. 100553, 2025.

[137] D. L. Schumacher, J. Singh, M. Hauser, E. M. Fischer, M. Wild, and S. I. Seneviratne, "Exacerbated Summer European Warming not Captured by Climate Models Neglecting Long-Term Aerosol Changes," *Communications Earth & Environment*, vol. 5, p. 182, Apr 2024.

[138] C. Simolo and S. Corti, "Enhanced Risk of Hot Extremes Revealed by Observation-Constrained Model Projections," *Communications Earth & Environment*, vol. 6, p. 165, Feb 2025.

[139] H. Tabari, S. M. Paz, D. Buekenhout, and P. Willems, "Comparison of Statistical Downscaling Methods for Climate Change Impact Analysis on Precipitation-Driven Drought," *Hydrology and Earth System Sciences*, vol. 25, no. 6, pp. 3493–3517, 2021.

[140] M. R. Leadbetter, "Extremes and Local Dependence in Stationary Sequences," *Zeitschrift für Wahrscheinlichkeitstheorie und Verwandte Gebiete*, vol. 65, pp. 291–306, Dec 1983.

[141] A. Dierickx, "Precipitation Extremes in Regional and Convection-Permitting Climate Models: Validation and Future Projections," June 2024.

[142] J. Hosking and J. Wallis, "Parameter and Quantile Estimation for the Generalized Pareto Distribution," *Technometrics*, vol. 29, no. 3, pp. 339–349, 1987.

[143] A. L. Buck, "New Equations for Computing Vapor Pressure and Enhancement Factor," *Journal of Applied Meteorology and Climatology*, vol. 20, no. 12, pp. 1527 – 1532, 1981.

[144] C. H. Bedingfield and T. B. Drew, "Analogy Between Heat Transfer and Mass Transfer," *Industrial & Engineering Chemistry*, vol. 42, pp. 1164–1173, Jun 1950.

[145] C. van Wagner and T. Pickett, "Equations and FORTRAN Program for the Canadian Forest Fire Weather Index System," tech. rep., 1985.

[146] C. van Wagner, "Development and Structure of the Canadian Forest Fire Weather Index System," tech. rep., 1987.